

Development of an on-line aqueous particle sensor to study the performance of inclusions in a 12 tonne, delta shaped full scale water model tundish.

by

Abhishek Chakraborty

Department of Mining and Material Engineering
McGill University, Montreal
May 2010

A thesis submitted to McGill University in partial fulfillment of the requirements of the degree of M.Eng.

© Abhishek Chakraborty, 2010

Abstract

Detection of particulate matter thinly dispersed in a fluid medium with the aid of the difference in electrical conductivity between the pure fluid and the particles has been practiced at least since the last 50 to 60 years. The first such instruments were employed to measure cell counts in samples of biological fluid. Following a detailed study of the physics and principles operating within the device, called the **Electric Sensing Zone (ESZ)** principle, a new device called the **Liquid Metal Cleanliness Analyzer (LiMCA)** was invented which could measure and count particles of inclusions in molten metal. It provided a fast and fairly accurate tool to make online measurement of the quality of steel during refining and casting operations. On similar lines of development as the LiMCA, a water analogue of the device called, the **Aqueous Particle Sensor (APS)** was developed for physical modeling experiments of metal refining operations involving water models. The APS can detect and measure simulated particles of inclusions added to the working fluid (water). The present study involves the designing, building and final application of a new and improved APS in water modeling experiments to study inclusion behavior in a tundish operation. The custom built instrument shows superior performance and applicability in experiments involving physical modeling of metal refining operations, compared to its commercial counterparts. In addition to higher accuracy and range of operating parameters, its capability to take real-time experimental data for extended periods of time helps to reduce the total number of experiments required to reach a result, and makes it suitable for analyzing temporal changes occurring in unsteady systems. With the modern impetus on the quality of the final product of metallurgical operations, the new APS can prove to be an indispensable research tool to study and put forward innovative design and parametric changes in industrially practised metallurgical operations.

Résumé

La détection de particules finement dispersées dans un fluide à l'aide de la différence de conductivité entre le liquide pur et les particules est pratiquée depuis environ 50 à 60 ans. Le premier instrument utilisant cette technique fut employé pour mesurer le nombre de cellules dans des échantillons de fluide biologique. Suivant une étude détaillée de la physique et du principe d'opération de l'appareil appelé zone de détection électrique (Electric Sensing Zone -- ESZ), un nouvel appareil, baptisé analyseur liquide de propreté en métal (Liquid Metal Cleanliness Analyzer -- LiMCA), pouvant mesurer le nombre de particules d'inclusion dans les métaux en fusion fut inventé. Cet instrument constituait un outil rapide et précis pour faire des mesures en ligne de la qualité de l'acier au cours du raffinage et de l'opération de coulée. Dans la même lignée de développement que le LiMCA, un outil analogue, spécifique à l'eau, appelé senseur de particules aqueuses (Aqueous Particle Sensor -- APS) fut développé pour la modélisation physique des expériences reliées aux opérations de raffinages des métaux impliquant des modèles aqueux. L'APS peut détecter et mesurer les particules d'inclusions simulées ajoutées au fluide (l'eau). Cette recherche comprend la conception, la réalisation ainsi que l'application finale d'un APS (dans l'eau) nouveau et amélioré appliqué aux expériences de modélisation afin d'étudier le comportement de l'inclusion dans une opération de répartiteur. L'instrument bâti sur mesure démontre une performance supérieure, comparé à ses équivalents commerciaux, applicable dans des expérimentations comprenant de la modélisation physique des opérations de raffinage de métaux. En plus d'une précision accrue et d'un plus grand éventail de paramètres d'opérations, sa capacité de traiter des données expérimentales en temps réel pour de longues périodes rend l'outil en question plus appropriée pour l'analyse temporelle des changements occurrent dans des systèmes instables. En concordance avec l'impératif moderne concernant la qualité du produit final des produits de la métallurgie, ce nouvel APS peut s'avérer être un outil de recherche indispensable pour étudier et mettre de l'avant la conception innovatrice ainsi que les changements paramétriques des opérations métallurgiques pratiquées en industrie.

Acknowledgements

It is with a great sense of gratitude that I express my appreciation to Prof. R.I.L. Guthrie for his consistent and enlightening guidance and assistance during my time as a master's student at McGill University. I would also like to extend my regards to Dr. Mihaiela Isac for her constant endeavor in making our research activities at the McGill Metals Processing Centre and McGill University a memorable experience. Their help, in the planning and carrying out of these research activities over the past year, has been invaluable.

As an international student studying in a foreign country, I am especially thankful to MMPC, Quebec Iron and Titanium and Heraeus Electro-Nite for extending me financial assistance during my stay in Montreal. No less a contribution to the present study was that of C. Szalasci, as it was his craftsmanship which produced the several prototypes and experimental setups that were used in the course of laboratory experimentations.

A number of colleagues and friends, including K. Chattopadhyay, K. Morales and Jaspreet Gill, and other members of the McGill community rendered invaluable assistance in carrying out experimental studies in the laboratory. I would also like to thank L. Calzado for his assistance in carrying out the numerous experiments done as a part of the present scientific study. Fellow MMPC members Patrick Lemieux and Dong Hui Li were especially helpful and supportive since my induction into the research group.

Finally, my last words of gratitude goes to my family in India, my parents and my sister, without whose continuing support and affection, I would never have been able to complete this thesis.

Nomenclature of Variables

ΔV	: change in voltage when the particle passes through the orifice	Volts
ρ_e	: the electrical resistivity of the working fluid	$\Omega\text{-m}$
I	: constant current flowing through the orifice	A
d	: diameter / radius of the particle	m
D	: diameter of the orifice	m
ρ_{eff}	: effective electrical resistivity within the orifice	$\Omega\text{-m}$
$A(x)$: cross sectional area of the orifice as a function of distance along the axis	m^2
ρ_s	: electrical resistivity of the particle	$\Omega\text{-m}$
f	: volume fraction of the particle in the orifice	
L	: geometric length of the orifice	m
R	: resistance across the orifice when there are no particles in it	Ω
ΔR	: change in effective resistance across the orifice due to the passage of a particle	Ω
I_1	: current through the orifice when there are no particles	A
I_2	: current through the orifice when a particle of inclusion passes through it	A
V_0	: potential difference across the cell used to excite the APS detector	Volts
V_1	: potential difference across the orifice when there are no particles in it	Volts
V_2	: potential difference across the orifice with a particle of inclusion in it	Volts
R_B	: value of the ballast resistance in the excitation circuit for the Detector	Ω

k	: constant / constant of proportionality	
α	: (linear) gain of the amplifier	
V_{in}	: signal voltage at the input side of logarithmic amplifier	Volts
V_{out}	: signal voltage of the amplified signal from the logarithmic Amplifier	Volts
V_{ref}	: reference voltage of the logarithmic amplifier	Volts
α_2	: amplification factor for the logarithmic amplifier	
p	: pressure	Pa
ν_f / ν	: kinematic viscosity of a fluid	m^2/s
ρ_f	: density of the fluid	kg/m^3
F_e	: Lorentz force acting on the particle	N
$\mathbf{J}(J_x, J_y)$: electric current density	A/m^2
\mathbf{B}	: self induced magnetic field	Wb/m^2
σ_e	: electrical conductivity	mho/m
ϕ	: electric potential	Volts
μ_0	: magnetic permeability of free space	H/m
μ_f	: dynamic viscosity of the liquid	$Kg/m-s$
$u_p(t)$: instantaneous particle velocity	m/s
d/dt	: represents a time derivative following a moving particle	
D/Dt	: time derivative following a moving element.	
m_f	: fluid mass displaced by the particle	Kg

$\mathbf{u}_p(u_p, v_p)$ and $\mathbf{u}(u, v)$

	: represent the respective instantaneous velocity of the particle and the undisturbed fluid velocity at the centre of the particle that would apply in the absence of the particle	m/s
σ_{ep}	: electrical conductivity of the particle	mho/m
Re_p	: particle Reynolds number	
C_D	: drag coefficient on the particle	
$C_{D\infty}$: drag coefficient on the particle at infinite distance from the wall	
λ	: geometric scale factor	
L_p	: linear dimension in the prototype	
L_m	: linear dimension in the model	
U	: characteristic velocity	m/s
L	: characteristic length	m
g	: acceleration due to gravity	m/s ²
Re	: Reynolds number	
Fr	: Froude number	
$f(s)$: particle size fraction as a function of 's'	
s	: particle size range	μm
x	: concentration of particles in solution	g/ml
y	: aspiration rate through the APS	ml/min
N	: number of particles detected by a probe per min at steady state	min ⁻¹

List of Figures

Chapter 1

Figure 1.1 – Electric sensing zone principle

Figure 1.2 – Electric circuit for excitation current

Figure 1.3 – Sequence of signals generated in the LiMCA apparatus

Figure 1.4 – Resolution limit of linear amplifiers

Figure 1.5 – Signal sequence generated using a logarithmic amplifier

Figure 1.6 - Pulse height analyzer

Figure 1.7 – Other peak parameters studied by the DSP

Figure 1.8 – Distortion of an electric field due to the presence of a nonconducting particle

Figure 1.9 – Computational domain used by Mei Li for mathematical modeling

Figure 1.10 – a) Self induced magnetic field distribution B within the ESZ for a DC current of 15A and orifice diameter of 500μ . b) Flow fields generated within the ESZ under identical conditions c) Color contours showing electric fields distribution. d) Electric field distribution with a current of $30\mu A$ and orifice diameter of 270μ .

Figure 1.11 – Schematic of the “smart probe” designed by Mei Li and R.I.L. Guthrie

Figure 1.12 – Apparatus described by Coulter in the original patent filed in 1953

Figure 1.13 – Coulter’s improved design showing syringe and weight arrangement to ensure constant aspiration rate through the orifice

Figure 1.14 – Schematic showing the 1973 design of Coulter’s bottom aspirated detection tube

Figure 1.15 – a) Schematic cross section of the orifice used by Doutre. b) Experimental setup used by Doutre for LiMCA in aluminum

Figure 1.16 – LiMCA for Aluminum, design patented by Doutre and Guthrie in 1986

Figure 1.17 – Experimental water model setup, used by Tanaka

Figure 1.18 – a) Final appearance of the detector tube developed. b) Schematic of its construction

Figure 1.19 – Single use disposable inclusion detector patented in 1993

Figure 1.20 – Schematic cross section of the orifice used in LiMCA for steel

Figure 1.21 – Representative micrographs of PodFA samples

Figure 1.22 – Performance characteristics of LiMCA apparatus developed to date

Figure 1.23 – Schematic of an ultrasonic inclusion detector

Figure 1.24 – Time line showing important milestones in LiMCA development

Figure 1.25 - a) LiMCA CM made by ABB for molten aluminum, b) Commercial LiMCA in steel by Heraeus Electro-Nite

Chapter 2

Figure 2.1 – Electric sensing zone principle operating in the detector tube

Figure 2.2 – Image of the detector probe designed by Heraeus Electro-Nite

Figure 2.3 – Schematic diagram of the detector probe from APS III shown in Figure 2.1

Figure 2.4 – Raw signals showing worsening signal quality with extended usage of the original Heraeus Electro-Nite APS detector probe

Figure 2.5 – CAD model of the final APS III sensor developed, b) Working prototype of the APS III sensor

Figure 2.6 – Microscopic view of the APS III amplifier

Figure 2.7 – Circuit diagram of the APS III amplifier

Figure 2.8 – Oscilloscope trace showing performance characteristics of the APS amplifier

Figure 2.9 – View of the fully assembled APS amplifier

Figure 2.10 - a) Unfiltered raw signal from amplifier. (b) Signal obtained after high and low frequency noise filtering. (c) Signal obtained after application of threshold noise removal.

Figure 2.11 – Pulse height analyzer

Figure 2.12 – Algorithm used in APS III

Figure 2.13 – Screenshot of the user input interface for APS III

Figure 2.14 – Gaussian distribution peaks obtained with standard particle sizes

Figure 2.15 – Final calibration curve for APS III

Figure 3.1 – A water model of a full scale, 12 tonne, delta shaped, tundish located at the McGill Metals Processing Centre.

Chapter 3

Figure 3.2 – The past, present and the future of casting processes

Figure 3.3 – Schematic of the slab casting process

Figure 3.4 – The shape of the four strand delta-shaped continuous casting tundish

Figure 3.5 – a) An APS sensor attached to a strand, b) Highlighted area showing APS aspiration tube

Figure 3.6– Conductivity, temperature and pressure sensor installed below the ladle to record the physical characteristics of the water

Figure 3.7 –Schematic diagram of the experimental setup

Figure 3.8 – Microscopic view of the hollow glass microspheres used to simulate inclusions

Figure 3.9 – Total particle count at the exit strands with a bare tundish

Figure 3.10 – Image showing the flow modifiers tested. a) Standard QIT impact pad b) angled dam, c) slotted dam, d) holed dam

Figure 3.11 – Comparison of flow modifier performance using Steady State Inclusion Entrainment Rate.

Figure 3.12 – Comparison of RRI values at differing size ranges between bare tundish and standard impact pad.

List of Tables

Table 2.1 – Size ranges in microns into which particles were classified

Table of Contents

<i>Introduction</i>	1
<i>Chapter 1</i>	
1.1.0 Introduction	3
1.2.0 Importance of the study of inclusions	4
1.3.0 Working principle	6
1.3.1 The LiMCA equation adopted	7
1.3.2 The electronic circuit and excitation technique	9
1.3.3 LiMCA amplifiers	12
1.3.4 The signal processing technique and data acquisition	17
1.4.0 Mathematical modeling of the Electric Sensing Zone	19
1.4.1 Flow field in the orifice	20
1.4.2 Equation of motion of inclusions	25
1.5.0 Development of Counter Counters 1953-1986 (patent review)	28
1.5.1 Improvement in inclusion design	30
1.5.2 Signal processing and algorithm development	33
1.6.0 Development of Liquid Metal Cleanliness Analyzers	
(LiMCA) 1979-2010	35
1.6.1 LiMCA in molten aluminum	36
1.6.1.1 Development of LiMCA electrodes	36
1.6.1.2 Development of LiMCA detector tubes	37
1.6.2 Aqueous Particle Sensor (APS)	38
1.6.3 LiMCA in steel (ESZpas)	40
1.6.3.1 Electrode design for steel LiMCA	43
1.6.3.2 Development of detector tubes	43
1.7.0 Performance comparison of LiMCA	44
1.7.1 Porous Disk Filtration Apparatus (PodFA)	45
1.7.2 Metallurgical and microscopic analysis	46
1.7.3 Ultrasonic techniques	47
1.6.0 Conclusions	48

<i>Chapter 2</i>	
2.1.0 Introduction	51
2.2.0 Aqueous particle detection system	51
2.3.0 Working design	52
2.3.1 The APS equation adopted	53
2.4.0 Design of new APS sensor probe	55
2.4.1 Size and shape of orifice	59
2.5.0 Amplifier used	60
2.6.0 Adopted noise reduction/signal conditioning techniques	64
2.7.0 Algorithm used for the study of particle size	67
2.8.0 Calibration for APS III	71
2.8.1 Coincidence limit of APS III	74
2.9.0 Conclusions	74
<i>Chapter 3</i>	
3.1.0 Introduction	76
3.1.1 Continuous casting process	77
3.1.2 Behavior of inclusions	80
3.1.3 Physical modeling of tundish operations	80
3.2.0 Details of physical model used	82
3.3.0 Experimental procedures	84
3.4.0 Experimental results	88
3.4.1 Experiment with different flow modifiers (Rio Tinto QIT, Fer. et Titan. 4 strand delta shaped tundish)	90
3.4.2 Calculation of RRI for standard impact pad	91
<i>Conclusions</i>	93
<i>Future work</i>	94

Introduction

Modern fast paced research activities in liquid metal refining and casting operations area are a testament to the ever more stringent quality requirements for final metal castings. As more and more manufacturing units are switching to continuous casting routes, it is need-less to mention that extensive research is expected in the field of continuous casting techniques. Perhaps the single most important subsystem of the con-cast unit is the tundish. The tundish not only acts as an intermediate buffer, but also acts as an important reactor for carrying out further refining operations for the liquid metal. Since large tundishes can have residence times in excess of half an hour, it is an excellent location to carry out inclusion separation. Most inclusion particles occurring in molten steel are of an oxide nature with a significantly lower density as compared to the molten metal. This, plus the relatively low levels of bath agitation generally found within the tundish, facilitates their floating to the surface and being absorbed in the upper slag layer.

Special flow modifiers are often retrofitted within the tundish, to further dissipate the fluid velocities within the path by isolating the falling jet of molten steel as it is emptied from the ladle into the tundish. While proper design and use of these flow modifiers is essential, the high cost of setting up pilot plants and the dangers involved in doing research on a fluid like molten steel, inhibit research activities there. Such studies are therefore carried out in safer alternative systems, namely water models. The liquid steel is replaced by water, and non-dimensional numbers like Reynolds and Froude numbers are chosen to ensure exact similarity exists between the prototype and its model.

Study of inclusion behavior in tundish systems are done in water models by adding simulated particles of inclusions within the water and tracking their movements using specialized equipment, commonly referred to as Aqueous Particle Sensors. One such commercial maker of this kind of instrument for steel is Heraeus Electro-Nite, whose modified device was being used at the McGill Metals Processing Centre to carry out inclusion behavior studies in water models.

However, the design and mode of operation of the commercial APS severely limited its versatility. Researchers had limited options and variables to change within the device for its application to differing experimental setups. The current study consists of two essential parts. Firstly, a new and improved APS needed to be developed with more versatility, accuracy and reliability than its commercially available counterpart, Secondly, the new instrument was put to use as a research tool for carrying out physical modeling experiments. The device was first put to use to carryout performance tests on some industrially used flow modifiers, for a set of routine experiments requisitioned by Rio Tinto, Quebec Iron and Titanium. The new APS was easy to operate and user friendly to researchers and provided valuable insight into the differing performances of a tundish operating under different configurations.

Literature Review

1.1.0 Introduction

Liquid Metal Cleanliness Analyzers, or LiMCA, for short, is a class of inclusion detectors for liquid metals, comprising an Electric Sensing Zone (ESZ), a data acquisition setup, and associated signal processing techniques. It has the potential of providing an instantaneous quantitative measure of the amount of larger non metallic, inclusions in molten metals. Therein lies the sheer importance of the device in modern metallurgical industries involved in the refining and casting of liquid metals. With the modern fast paced development in materials engineering, there are ever more stringent restrictions on the quality and cleanliness of metals being produced. Modern research projects aimed at producing ultra clean steel is a testament to the requirement for an efficient and reliable metal cleanliness analyzer. LiMCA basically works on the Electric Sensing Zone (ESZ) principle first considered by J.C. Maxwell and first exploited by Wallace Coulter back in 1953, for aqueous systems. Its direct extension to the metallurgical industry was first proposed and exploited by Guthrie and Doure in late 1979 with the first working instrument designed to detect inclusions in liquid aluminum processing operations. In further research activities at McGill University it was extended to the detection of inclusions in steel and copper, and also resourced into a research tool for water modeling experiments, to monitor continuously, inclusions in water models of metallurgical processing operations. For these, the off-line Coulter Counters used in the medical industries were not suited.

Prior to 1980, the scientific development of Coulter Counters was carried out by a large number of independent researchers and different companies, working on various aspects of the aqueous device, such as probe design, signal processing and data acquisition, amongst others. The published literature of the time are thus scattered and disjointed, and a review of just the published scientific work of the time would be inadequate to portray the development of the LiMCA equipment. However, since its initial principles were mostly developed by contemporary

inventors trying to market and sell their apparatus, a fairly consistent trend in the development of the LiMCA technique can be obtained from the various patents filed since 1983, when the first patent was issued in the United States. 1980 to 2000 saw a remarkable development of LiMCA as several variants of it were designed for a variety of metal systems such as aluminum, magnesium, copper, iron and steel, etc. As a result, commercial production models are now being marketed by ABB and Alcan (LiMCA CM ® for Aluminum) and Heraeus Electro-Nite (ESZpas for steel). Recent activities in its continuing development at McGill University are aimed at improving LiMCA equipment as an aqueous analogue for physical modeling experiments, and to solve and eliminate some problems associated with using water as the working fluid.

1.2.0 Importance of the study of inclusions

Non-metallic second phase particles which may be present in molten metal prior to casting have a profound influence on the final properties of the material. These include UTS, elongation, anisotropy, fatigue life, hydrogen cracking susceptibility and surface streaks for lithographic plate materials, amongst many others. Non-metallic inclusions include oxides, silicates, sulfides, nitrides, carbides, and their compounds or composites. Under normal conditions sulfides, carbides, and nitrides precipitate during cooling of molten steel below the solidus temperature. Small particles of particular oxide inclusions, sulfides, carbides, and nitrides, have been utilized to control microstructure for improving final metal properties, especially in steel and aluminum alloys. However, much larger sized inclusions can be formed, such as agglomerates, or through steel re-oxidation or through slag entrainment while the metal is in liquid state. If they are not removed from the melt before solidification, these large inclusions can cause defects in the cast products, which in turn give rise to processing difficulties and failures, decreased productivity, degraded product properties, and reduce premium yield.

(ref 1)

The exact size, shape, morphology and density of inclusions in the final cast product is thus of the utmost importance. It is widely used and accepted that the presence of well dispersed inclusions of average size generally less than 30μ provide good work hardenability to the metal. These small inclusions prevent movement of dislocations within the bulk of the metal and lead to rapid increases in the ultimate tensile strengths in the material. (ref 2) Many grades of steel such as high speed steels, rely on small particles of Tungsten Carbide and/or Vanadium Carbide for their increased strength. This technique of increasing the strength in metals is also practiced in many copper, titanium and aluminum alloys, where small second phase intermetallic compounds are deliberately precipitated within the bulk of the casting. Relatively larger inclusions, on the other hand, severely compromise the strength of the final product. The fact that these inclusions largely exhibit extremely poor mechanical properties and are mostly incoherent with the metal matrix, severely weakens the final structure. (ref 3,4,5) The best example of this would be the high manganese free machining steels. It is perhaps amongst a very few examples where the deleterious effect of large Manganese Sulfide inclusions is put to advantage, where the reduced local strength of steel, is helpful for easy machining (scarfing is improved). Apart from the size of the particles, their shape is also an important determining parameter. This aspect is apparent in the marked difference in properties between a Gray Cast Iron and a Ductile Cast Iron. (ref 6) The transformation in the shape of the graphite particles from flaky to nodular gives greatly improved fracture resistance and formability.

The inclusions that are generally encountered in molten metals can be generally listed into two broad categories.

- *Indigenous inclusions* The best examples of inclusions of this type would be small particles (generally $<30\mu$) of metallic oxides such as Al_2O_3 or $FeO.SiO_2$, found in Aluminum Killed (A.K.) or Silicon Killed (SiK) Steels. Oxygen has a finite solubility in molten steel (2300 ppm at $1600^{\circ}C$), and the deoxidizer reacts with it to form small oxide particles. As such they are formed as a result of metal processing operations. In a very

similar way, we can have indigenous inclusions of silicates, sulfides and carbides.

- *Exogenous inclusions* These inclusions are generally in a size range in excess of 40 μ m, and are formed as a result of the molten steel in contact with a number of external sources, including particles of refractory from erosion, and small droplets of emulsified ladle or tundish slag and oxidation products formed by the liquid steel reacting with air.

The exact type, nature, and composition of inclusions that are encountered in several metal systems is huge in number, and would warrant a voluminous review in its own right. However, in the light of the current study, with due emphasis on LiMCA, a technology useful to measure and characterize these inclusions, this section merely aims to emphasize the importance of the study of inclusions in predicting final metal properties. (ref 7,8)

1.3.0 Working principle

The Electric Sensing Zone principle that is at the heart of this liquid metal device, works on the fact that there is a difference in electrical conductivity of the particle (non-metallic inclusion) and the working fluid (molten metal). Thus, the detector itself is a way to measure resistances of the fluid medium. Similarly, Coulter Counters are designed for biological use and the fluid medium is water. In this section therefore the medium will be just addressed as the “Working Fluid”.

Figure 1.1 shows the working principle of the device. The fluid containing a suspension of the inclusion particles is allowed to pass through a narrow orifice. Two electrodes are used so as to apply a constant electrical current supply (I) through the orifice. When the orifice contains no particles, the resistance (R) across the electrodes is due only to the conductive fluid. This produces a potential difference $V=(IR)$ across the electrodes, which is recorded as the base-line output for no particles present. Now consider a single particle which enters the orifice, or electric sensing zone, thereby displacing its own volume of fluid. Since the

conductive fluid in the orifice is now replaced by an insulating particle, the resistance across the orifice changes to $(R+\Delta R)$ and the potential difference across the electrodes jumps to $I(R+\Delta R)$. This jump in voltage as the particle passes through the orifice is recorded and its magnitude is an indication as to the size of particle. (ref 9,10,11)

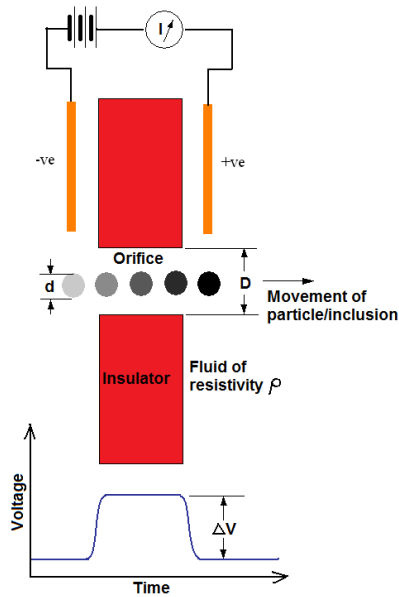


Figure 1.1 - Electric sensing zone principle

1.3.1 The LiMCA equation adopted

Obviously during actual measurements for discrete particles within an Electric Sensing Zone (ESZ), the number of peaks detected is equal to the number of particles sampled, and the height of the peaks is related to the particle sizes by equation 1.1 (ref 12)

$$\Delta V = \frac{4\rho_e I d^3}{\pi D^4} \quad [1.1]$$

Where ΔV is the change in voltage when the particle passes through the orifice

ρ_e is the electrical resistivity of the working fluid

I is the constant current flowing through the orifice

d is the diameter of the particle

D is the diameter of the orifice

The above equation was derived from Maxwell's approximations, that the particles are so dispersed in the medium that they do not in any way alter the electric field within the orifice, except at positions near the particle surface. Also equation 1.1 has been derived by assuming that the particles are perfect insulators. Here we will attempt to make a more general equation for the relation between voltage difference and the size of the particle.

Now

$$R+\Delta R=\rho_{eff} \int \frac{dx}{A(x)} \quad [1.2]$$

Where ρ_{eff} is the effective electrical resistivity within the orifice

A(x) is the cross sectional area of the orifice

Let ρ_s be the electrical resistivity of the particle

f be the volume fraction of the particle in the orifice

L is the geometric length of the orifice

$$\text{So (ref 9) } \rho_{eff} = \left[\frac{2\rho_s + \rho_e + f(\rho_s + \rho_e)}{2\rho_s + \rho_e - f(\rho_s + \rho_e)} \right] \rho_e \quad [1.3]$$

$$\text{And } f = \frac{\text{volume of particle}}{\text{volume of sensing zone}}$$

$$= \frac{\pi/6 d^3}{\pi/4 D^2 L}$$

$$= \frac{2d^3}{3D^2 L} \quad [1.4]$$

So with this information we can measure the change in resistance when the particle passes through the orifice

$$\Delta R = \frac{4\rho_{eff}L}{\pi D^2} - \frac{4\rho_e L}{\pi D^2} = \frac{4L}{\pi D^2} (\rho_{eff} - \rho_e) \quad [1.5]$$

Now with this set of general equations we will to derive the original Maxwell's equation [1.1] for perfectly insulating particles. Thus from equation [1.3] we get

$$\begin{aligned} \rho_{eff} &= \lim_{\rho_s \rightarrow \infty} \left[\frac{2\rho_s + \rho_e + f(\rho_s + \rho_e)}{2\rho_s + \rho_e - f(\rho_s + \rho_e)} \right] \rho_e \\ &= \frac{1}{2} \left(\frac{2+f}{1-f} \right) \rho_e \end{aligned} \quad [1.6]$$

Expanding the above equation using the power series, we get;

$$\rho_{eff} = \rho_e \left(1 + \frac{3}{2}f + \frac{3}{2}f^2 + \dots \right) \quad [1.7]$$

It is to be noted that the term $3/2f$ in equation 1.7 arises as a result of distortion of the electrical field around the sphere. Since $f \ll 1$, we can retain the first two terms and ignore the higher terms. Thus we get the change in resistance for a conducting particle passing through the orifice.

$$\Delta R = \frac{4\rho_e d^3}{\pi D^4} \quad [1.8]$$

1.3.2 The Electronic circuit and excitation technique

As explained in the preceding sections, a technique has to be devised to properly excite the detector tube. The ideal solution would be to apply a constant current power source across the electrodes. This would make sure that the potential difference across the electrodes would be directly proportional to the resistance across the probe, and independent of the circuit characteristics of the device. However, the use of constant current power supplies is not recommended in LiMCA type applications for the following reasons:

- Generally, constant current power supplies run on high internal resistance and open circuit potential differences. In practice, it is extremely difficult to produce a stable, noise free, source as required in this case. Furthermore, a high internal resistance in series across the electrodes would produce a constant current but of a very small magnitude. Since the voltage peak is proportional to the current flowing through them (equation 3.1) the detector tube would be very insensitive.
- For LiMCA in molten metal applications, a normal 12 volt battery with a substantial internal resistance often approximates a constant current source, as the resistance across the ESZ orifice is very small compared to the resistance of the circuit. This makes a separate constant current power source un-necessary.

Figure 1.2 depicts the simplest of all arrangements for providing excitation to the ESZ detector tubes. It uses a normal battery connected across a ballast resistance and the detector probe in series. (ref 13,14)

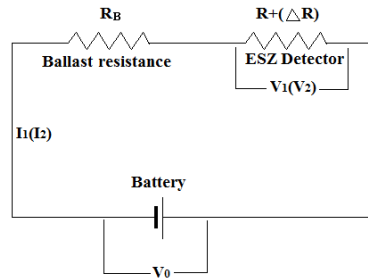


Figure 1.2 - Electric circuit for excitation current

Now from the arrangement shown in Figure 1.2, when only the liquid without any particle passes through the liquid, the voltage registered across the LiMCA probe is

$$I_1 = \frac{V_0}{R+R_B} \text{ and } V_1 = I_1 R \quad [1.9]$$

When a particle passes through the orifice, let the resistance of the probe increase by an amount ΔR . So the new current and potential difference across the electrodes become

$$V_2 = I_2(R + \Delta R) \quad \text{and} \quad I_2 = \frac{V_0}{R + \Delta R + R_B} \quad [1.10]$$

Therefore

$$\begin{aligned} \Delta V &= V_2 - V_1 \\ &= \left(\frac{R + \Delta R}{R + \Delta R + R_B} - \frac{R}{R + R_B} \right) V_0 \\ \Delta V &= \frac{\Delta R \cdot R_B}{(R + R_B)(R + \Delta R + R_B)} V_0 \quad [1.11] \end{aligned}$$

Now for most setups working in the liquid metal environment, the value of R_1 may be chosen to be substantially larger than R . This is easy as metals, being good conductors of electricity; the value of R is very small, and even with a resistance R_B of one order of magnitude higher connected in series, the value of I_1 does not decrease so much as to reduce the sensitivity of the detector.

$$\begin{aligned} \lim_{R_1 \gg R} \frac{\Delta R \cdot R_B}{(R + R_B)(R + \Delta R + R_B)} V_0 \\ \Delta V = \frac{\Delta R}{R_B} V_0 \end{aligned}$$

Now while designing the circuit, the values of R_1 and V_0 are kept constant and thus we have the working relation

$$\Delta V \propto V_0 \quad \text{or} \quad \Delta V = kV_0 \quad [1.12]$$

Thus from equation 1.12 it is apparent that the higher the voltage used for excitation, the higher would be the output signal, and hence the higher the sensitivity. However, this is not resorted to, as the higher voltage would

proportionally have to cope with the higher current demand of the circuit. Instead, an excitation voltage of around 12 volts may be used for most systems.

1.3.3 LiMCA amplifiers

Owing to the small value of ΔV obtained for the lower excitation voltage, an external amplifier arrangement is used which amplifies the entire range of ΔV from the microvolt range of signals generated by the inclusions to between 0 and 5 volts. This is ideal for most CMOS (Complementary Metal Oxide Semiconductor) based data acquisition systems.

Let α be the gain of the linear amplifier used, so from equation [1.1], the output voltage spike of the amplifier should be

$$\Delta V_{amplified} = \alpha \frac{4\rho_e I d^3}{\pi D^4} \quad [1.13]$$

At this point we will take a specific example of a detector operating under a particular set of conditions, say for example molten aluminum, so as to ascertain the order of magnitude of α . The exact value of the amplifier gain should be chosen so as to get a voltage peak of around 5 volts when the largest particle (in the range of interest) goes through the orifice. The following equation is an order of magnitude study for molten aluminum.

$$\Delta V_{amplified} \rightarrow 0 \text{ to } 5 \text{ Volts} \sim 0$$

$$I \rightarrow 50 \text{ Amps} \sim 1$$

$$\rho_e \rightarrow 2.42 \cdot 10^{-7} \text{ } \Omega\text{m} \sim -7$$

Molten aluminum has a conductivity of approximately 24.2 $\mu\Omega\text{cm}$ (ref 15)

$$d \rightarrow 0 \text{ to } 30 \text{ } \mu\text{m} \sim -5$$

$$D \rightarrow 500 \text{ } \mu\text{m} \sim -4$$

$$\pi \rightarrow 3.14 \sim 0$$

$$\langle 0|\alpha - 7 + 1 - 15 - (-16)\rangle, \text{ or } \alpha_{\text{aluminum}} \sim 5 \quad [1.14]$$

Thus it is seen that with a use of amplification in the range of around 100,000, we can achieve the desired results. It should be pointed here that the above analysis is aimed at only providing a purely theoretical value of the linear amplification factor from commonly used physical parameters used (and obtained from published literature) on LiMCA systems, the case of molten aluminum being taken as a mere example. In practice however (and especially in the case of purposely manufactured LiMCA for aluminum) amplification factors may differ.

We shall now repeat the above analysis for a similar system using water as the working fluid.

$$\rho_e \rightarrow 0.2 \cdot 10^4 \Omega \text{ m} \sim 3 \text{ (Measured value of ordinary tap water, page 72)}$$

$$I \rightarrow 1 \mu\text{A} \sim -6$$

$$\langle 0|\alpha + 3 - 6 - 15 - (-16)\rangle$$

$$\text{Or } \alpha_{\text{water}} \sim 2 \quad [1.15]$$

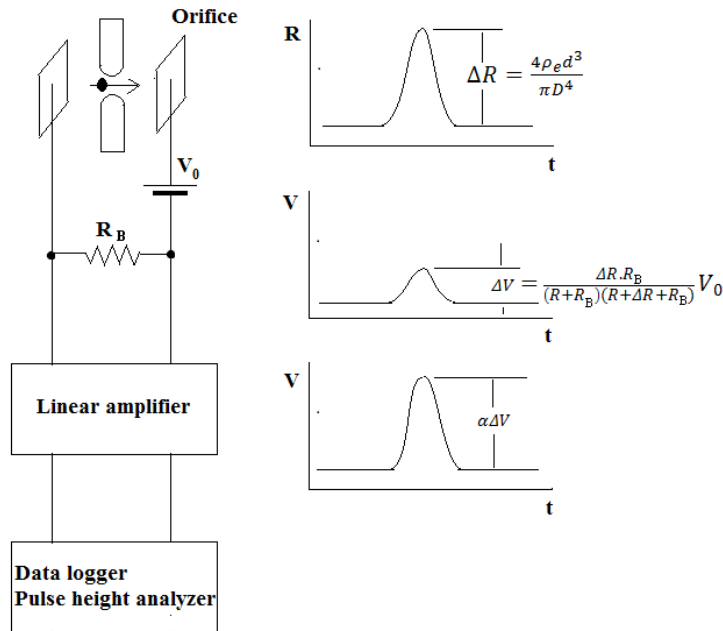


Figure 1.3 – Sequence of signals generated in the LiMCA apparatus.

In practice, amplifiers in this amplification range are very easy to construct using relatively small number of components. However the high resistance of the electric path through the water makes the signal prone to excessive noise pickup, and it is essential to implement adequate noise suppression techniques in case of Aqueous Particle Sensors.

While the signal conditioning techniques using a linear amplifier would have performed well in these devices, it was soon apparent that it was not the best solution, when it came to the task of instrument calibration. The cubic relation between the voltage peak and the particle size meant that the calibration curve would be highly non linear and the accuracy of the instrument would vary according to the size of the particle being measured. To solve this problem, a new breed of amplifier was introduced, known as a Logarithmic Amplifier. In these devices, the output voltage is α times the natural logarithm of the input voltage. The signal from the probe was pre-amplified slightly and then fed to the logarithmic amplifier, before passing to the pulse height analyzer.

Let α_1 be the gain of the pre-amplifier

α_2 be the gain of the log-amplifier

V_{ref} is the appropriately chosen normalization voltage. In practice V_{ref} is chosen equal to the base line voltage across the probe when no particle is passing.

Consider the general log amplifier equation

$$V_{out} = \alpha \ln \left(\frac{V_{in}}{V_{ref}} \right) \quad [1.16]$$

From the above equation, it is clear that when there are no particles are passing through the orifice $V_{in}=V_{ref}$ and the output of the amplifier is 0. Thus the log-amplifier has the added advantage of removing the DC component of the signal. Now in terms of digital data acquisition this has immense advantages. Firstly let's consider a CMOS based 16 bit data logger. So by theory, the instrument has a resolution of

$$5(\text{volts})/(2^{16}-1)$$

$$=5/65535 \sim 76\mu\text{V}$$

While we are doing our LiMCA measurements, we have two components, a DC component arising out of the base-line voltage across the probe, and a transient peak as the particle passes through. A linear amplifier which we used before would amplify both components. Since the maximum height of the peaks is fixed at 5 volts, we cannot utilize the full scale of resolution of the data logger. Resolution is lost in the DC part of the signal as shown in Figure 1.4.

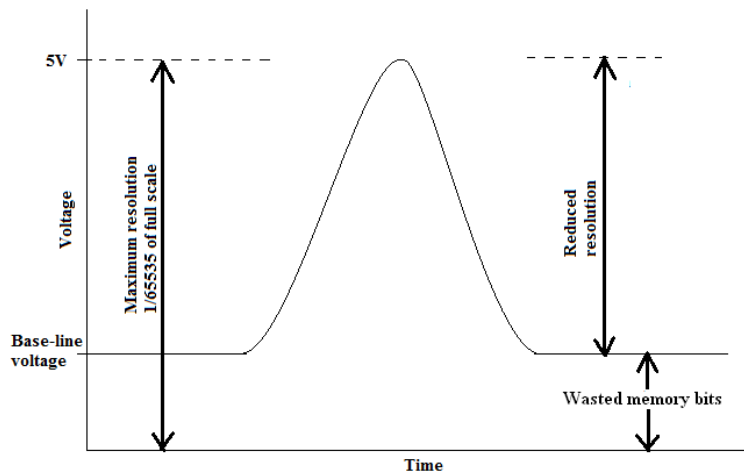


Figure 1.4 - Resolution limit of linear amplifiers

The digital data logger works by classifying the entire voltage range from 0 to 5 volts into 65535 divisions, and for our measurements, we are only interested in the ΔV values. Now since when using linear amplifiers, we cannot make the voltage peak span the entire measurable range, some of the 65535 divisions are wasted in the DC component of the signal, thereby reducing the particle size resolvability. The log-amplifier solves this problem by normalizing its output to 0 volts when no particle is passing through it.

From equations 1.1 and 1.16

$$V_{out} = \alpha_2 \ln \left(\frac{V_{in}}{V_{ref}} \right)$$

$$\text{And } V_{in} = \alpha_1 \frac{4\rho_e I d^3}{\pi D^4}$$

$$\text{Or, } V_{out} = \alpha_2 \ln V_{in} - \alpha_2 \ln V_{ref}$$

$$\text{Or, } V_{out} = \alpha_2 \ln \left(\alpha_1 \frac{4\rho_e I d^3}{\pi D^4} \right) - \alpha_2 \ln V_{in}$$

$$\text{Or, } V_{out} = \alpha_2 \ln \left(\alpha_1 \frac{4\rho_e I}{\pi D^4} \right) + \alpha_2 \ln (d^3) - \alpha_2 \ln V_{in}$$

$$\text{Or, } V_{out} = \alpha_2 \ln \left(\alpha_1 \frac{4\rho_e I}{\pi D^4} \right) + 3\alpha_2 \ln (d) - \alpha_2 \ln V_{in}$$

$$\text{Let, } A = \alpha_2 \ln \left(\alpha_1 \frac{4\rho_e I}{\pi D^4} \right) - \alpha_2 \ln V_{in}, \quad \text{and } B = 3\alpha_2$$

$$\text{Therefore, } V_{out} = A + B \ln (d) \quad [1.17]$$

Thus a semi-log plot of V_{out} and $\ln(d)$ would have a linear relation which is excellent for graphical interpolation to obtain a calibration curve. Figure 1.5 shows the modified signal sequence using a logarithmic amplifier.

Two other characteristics the LiMCA amplifier must possess are, a good noise reduction capability, and an excellent high frequency response. This is essential as the peaks in the signal are random transient phenomena lasting mostly less than a millisecond, so that the high frequency characteristic of the amplifier becomes even more essential. Further improvement in signal to noise ratios was achieved by implementation of appropriately chosen filters. Two specific type of filters were used

- A band-stop filter- Most equipment running off the mains power line adds a 50 Hz noise to the final signal, commonly referred to as the

“mains hum”. A band stop filter is designed to block out a very narrow frequency range near 50 Hz, from the LiMCA signal.

- A low pass filter- All exposed wiring are bound to pick up high frequency noises produced by external sources, like electrical equipment, radios etc. Though some of these noises peaks lie well within the frequency range of the LiMCA peak, the very high frequency noises can be blocked out without appreciably distorting the original LiMCA signal.

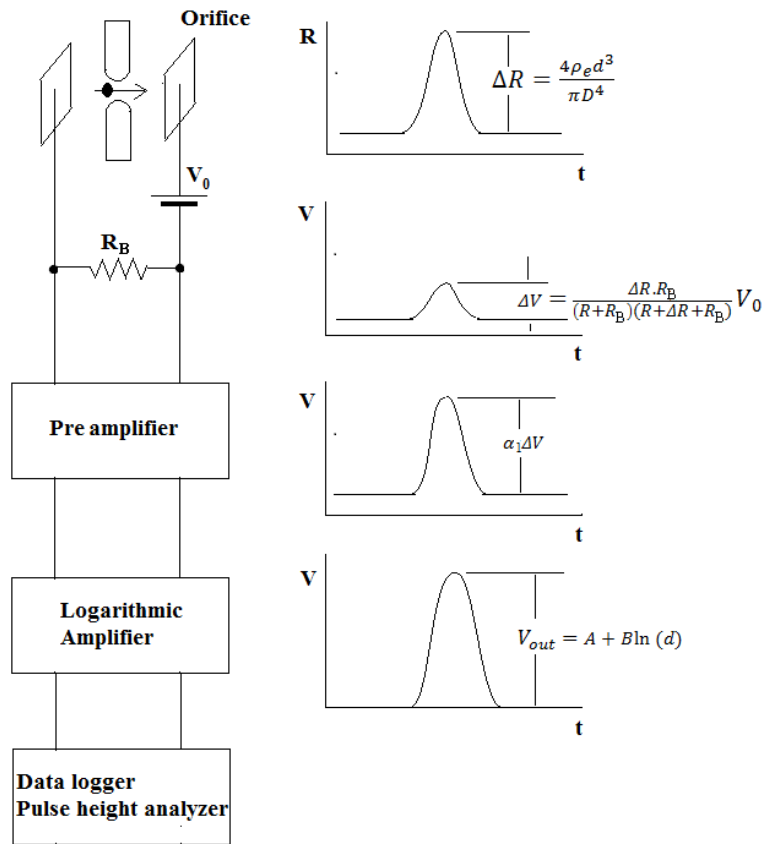


Figure 1.5 - Signal sequence generated using a logarithmic amplifier

1.3.4 The Signal processing techniques and data acquisition

Raw data obtained as the output signal from the LiMCA probe, and following successive amplification, would merely consist of a number of transient voltage pulses corresponding to each particle being counted. Since the particle generally takes less than a milli-second to pass through the orifice, these voltage pulses are

very narrow, and proper signal acquisition and analysis were a problem with the earliest Coulter Counters, as high performance solid state electronics were not available at the time. Prior to 1970, most Coulter instruments relied on feeding the signal to an oscilloscope, and photographing the oscilloscope trace. A manual measurement of the peak heights was done from measurements with an appropriate scale. Vacuum tubes and valves were utilized to automate the data analysis, but were never commercially exploited as they would generally have poor resolution and performance.

With the advent of single substrate chips, after the 1980s, this technology was eventually applied to LiMCA data acquisition and processing. During 1994, Tudor Draganovici, (ref 16) and Xiaodong Shi, (ref 17) made significant advancements to the instrument by incorporating a Digital Signal Processor, and programming a user-friendly computer application which allowed a user untrained in LiMCA to be able to quickly operate the device.

While the LiMCA signal gives us information about each particle, and in theory a data analyzer can be made that lists the size of each particle being detected, it would lead to a huge amount of information, which may not be very convenient for industrial or research purposes. So the signal processing algorithms developed, classified all the particles that were detected into a number of appropriately chosen bins (ref 18). Counters were used to store the number of particles falling into each size range or bin, and the resulting values of each counter were displayed as a histogram. This sort of data was much more convenient for analysis by the user. Figure 1.6 shows the process more clearly.

Though the above discussion gives a rather cursory glance of the pulse height analysis technique and the digital signal processors, detailed study of the exact electronics and the raw codes are outside the scope of the current review.

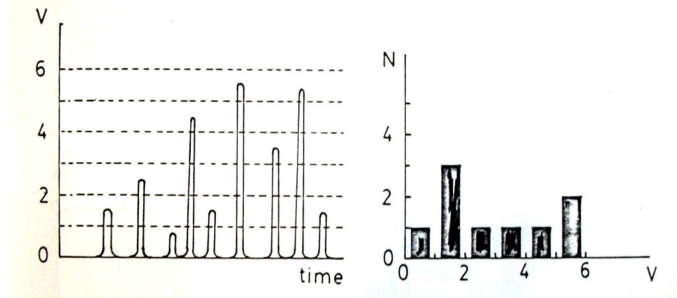


Figure 1.6 - Pulse height analyzer

Francois Dallaire and Chris Carroza's work in the late nineties (ref 19) proposed that while the pulse height was an indicator of the size of the particle being detected, more information of the exact nature of the particle, like its shape, aspect ratio, etc. could be obtained by accurately studying the exact shape of the peaks and not merely their heights. Figure 1.7 shows the other peak parameters which were studied.

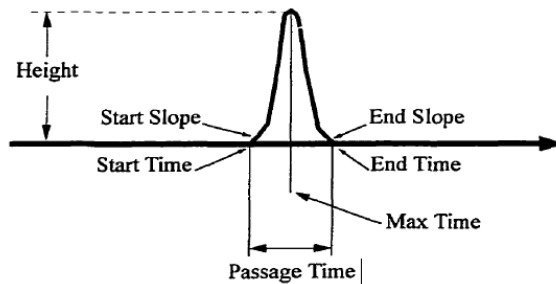


Figure 1.7 - Other peak parameters studied by the DSP

Among the motivations for their study was the prospect of being able to use the LiMCA setup to differentiate between a micro-bubble of air and a solid particle. Experiments were done with an aqueous LiMCA using a number of second phase particles such as, silica, latex and micro-bubbles of air. Experimental studies showed that indeed there were marked differences in transit times and entry slopes of the pulses according to particle density. Carroza also made a Fourier spectrum analysis of the signals. While his dissertation clearly showed the applicability of LiMCA in classifying not only the size but also the nature of the particle, he proposed no principles or algorithm by which this could be achieved.

A decade later, Xiadong Wang et al (ref 20), with the aid of mathematical modeling, would show exactly what governs the shape of the LiMCA pulses. This was especially true for the air bubbles, as they tended to deform as they passed through the orifice. The micro-bubbles would become elongated and have a larger residence time in the electric sensing zone than would an undeformable solid particle of the same volume, thereby making the peak broader and lower.

1.4.0 Mathematical modeling of the Electric Sensing Zone

Intensive mathematical modeling studies have also been conducted to uncover the exact physics associated with the motion of particles across the ESZ zone. Second phase particles flowing through the orifice would be affected not only by the fluid flow field within the orifice, but also by the electric fields passing through it, resulting in a Lorentz force which would tend to push the particles towards the side walls. While the analytical equation derived by Maxwell gave a basic correlation between particle diameter and amplitude of the voltage pulse, experimental results showed slight deviations from the ideal behavior. This could be attributed to our earlier simplifying assumption that the particle size is so small that it does not in any way alter the electric field within the orifice. However, as shown by the mathematical modeling results of Xiaodong et al, (ref 20) even a single particle will have the effect of appreciably distorting the electric field, as shown in Figure 1.8. The distorted electric field was compensated for by adding a correction factor of the form $f(d/D)$ (ref 21)

$$\Delta V = \frac{4\rho_e l d^3}{\pi D^4} f\left(\frac{d}{D}\right) \quad [1.18]$$

The correction function was obtained by Smythe (ref 22) by analyzing ideal flow of a fluid past a sphere (of diameter d) within a circular tube (of diameter D), and can be expressed as

$$f\left(\frac{d}{D}\right) = [1 - 0.8\left(\frac{d}{D}\right)^3]^{-1}$$

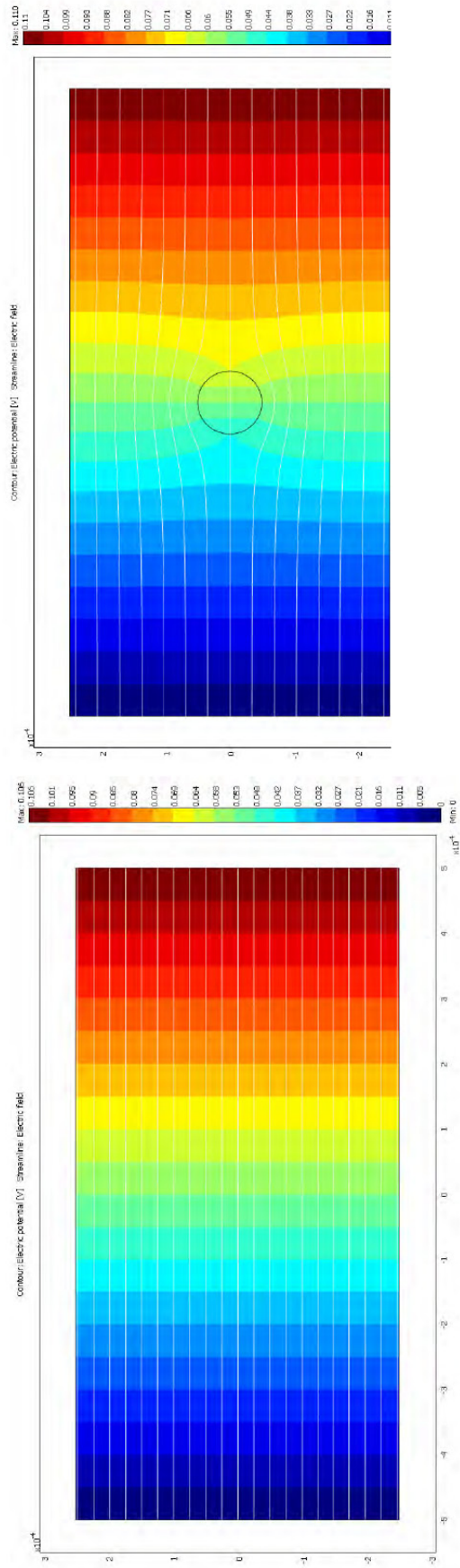


Figure 1.8 - Distortion of an electric field by the presence of a nonconducting particle

Advanced numerical simulations were carried out by Mei Li, (ref 10-12) and Xiadong Wang (ref 20) on the exact motion of particles through the current carrying orifice. Below are the basic concepts and equations used in the simulations.

1.4.1 Flow field in the orifice

Considering the general operating conditions under which the detector tubes are operated, the Reynolds number comes in around 1700 based on the orifice diameter. Several simplifying assumptions were considered

- The flow through the orifice is laminar and steady
- The fluid is incompressible
- The fluid has constant properties.

Considering the above conditions, the flow field can be modeled using the continuity equation and the Navier-Stokes equation. Since the current density within the orifice is high, Lorentz forces cannot be neglected and must be added in the Navier-Stokes Equation.

$$\nabla \cdot \mathbf{u} = 0$$

$$\mathbf{u} \cdot \nabla \mathbf{u} = -\frac{\nabla p}{\rho_f} + \nu_f \nabla^2 \mathbf{u} + \left(\frac{1}{\rho_f}\right) \mathbf{F}_e \quad [1.19]$$

Where $\mathbf{u}(u,v)$ is the fluid velocity vector

p is the pressure

ν_f and ρ_f are the density and kinematic viscosity of the fluid

\mathbf{F}_e is the Lorentz force acting on the liquid metal flow field and is defined as

$$\mathbf{F}_e = \mathbf{J} \times \mathbf{B}$$

Where $\mathbf{J}(J_x, J_y)$ is the electric current density in A/m^2

\mathbf{B} is the self induced magnetic field in Wb/m^2

Though the logical way to get values of \mathbf{J} and \mathbf{B} would be to solve the Maxwell's equations for magnetism, both Mei Li and Xiaodong Wang obtained \mathbf{J} by solving the Laplace equation, to deduce the induced magnetic field, \mathbf{B} .

$$\frac{\delta^2 \varphi}{\delta x^2} = \frac{1}{y} \frac{\delta}{\delta y} \left(y \frac{\delta \varphi}{\delta y} \right) = 0$$

where φ is the electric potential. The values of \mathbf{J} were obtained by using Ohm's law

$$J_x = -\sigma_e \frac{\delta \varphi}{\delta x}$$

$$J_y = -\sigma_e \frac{\delta \varphi}{\delta y}$$

Where σ_e is the electrical conductivity. The self induced magnetic field in terms of the azimuthal coordinate system can be obtained by using Amperes law, with μ_0 ($=4\pi \cdot 10^{-7} \text{ H}\cdot\text{m}^{-1}$) set as the magnetic permeability of free space.

$$B_\theta = \frac{\mu_0}{y} \int_0^y j_x \xi d\xi \quad [1.20]$$

Figure 1.9 (ref 11) shows the computational domain used by Mei Li for her numerical simulations, using her self-developed codes.

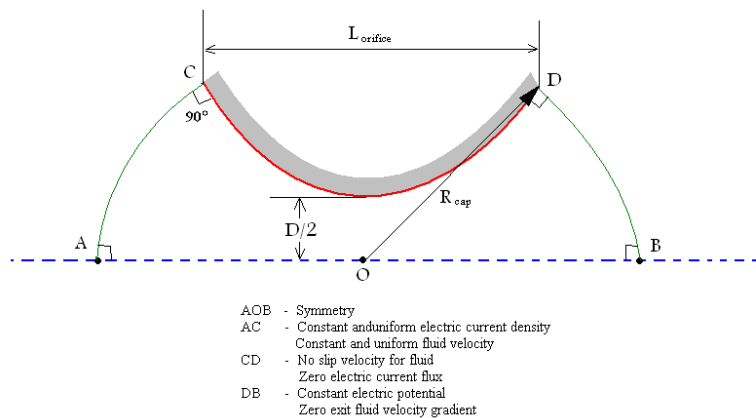


Figure 1.9 - Computational domain used by Mei Li for mathematical simulations

A parabolic contoured orifice was used for the simulations. The exit and inlet boundaries were defined by spherical caps centered at point O which is the centroid of the orifice. Xiadong et al using a new commercial simulation software Comsol Multiphysics 3.4, made similar numerical simulations, as shown in figure 1.10 (ref 22). It is to be pointed out that the results of both researchers were in close agreement when we compare the shape of the contours of the electric field.

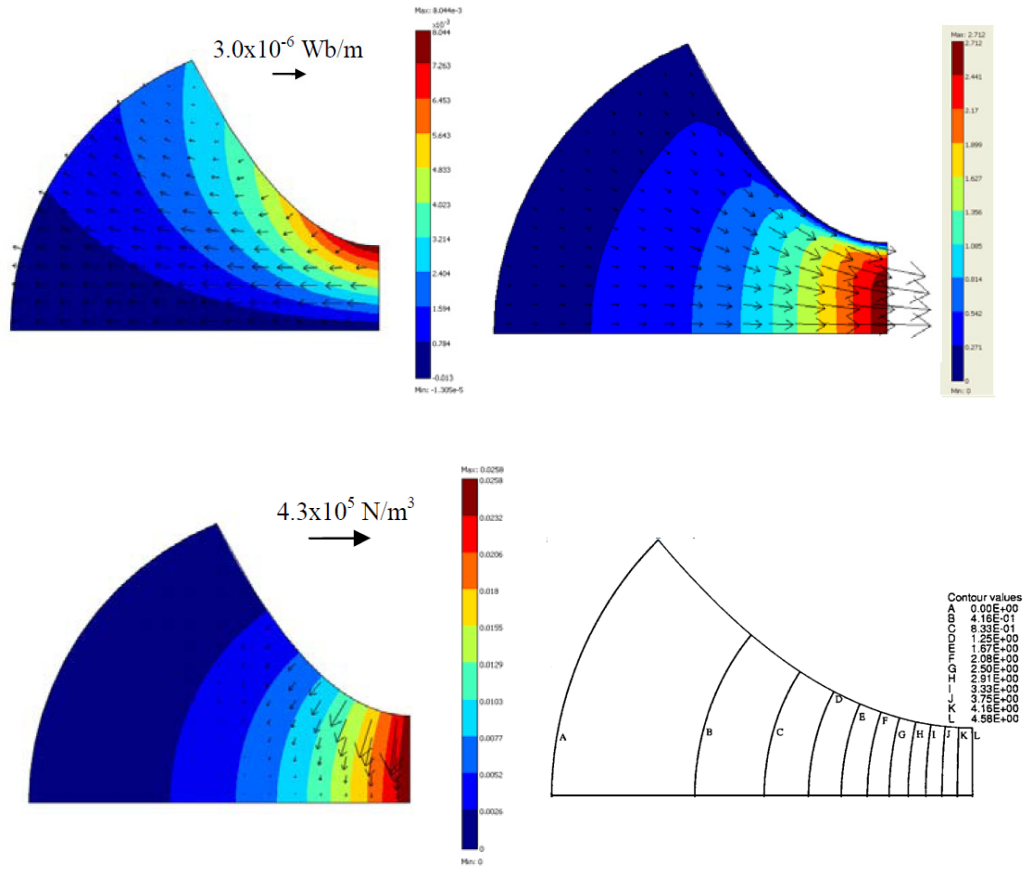


Figure 1.10 – a) Self induced magnetic field distribution B within the ESZ for a DC current of 15A and orifice diameter of 500 μ m. b) Flow fields generated within the ESZ under identical conditions c) Color contours showing electric fields distribution. d) Electric field distribution with a current of 30 μ A and orifice diameter of 270 μ m.

While in metal, the high current magnitudes necessitates consideration of magnetic forces for mathematical analysis, the magnetic effect can be safely neglected in aqueous ESZ as the current flowing through the aqueous media would be very small indeed. Figure 1.10 b) & 1.10 c) are more interesting because Xiadong (ref 23) and Mei Li (ref 11) obtained remarkably similar results using

two separate orifice dimensions and working fluids. Xiadong's model used an orifice diameter of 500 microns using liquid aluminum, while Mei Li considered a 270 micron orifice operating in water. Likewise the current flowing through the Aluminum was 15 Amps, while it was just 30 μA in case of water. The fact that the isopotential lines are almost straight and parallel to one another means that the original Ohmic model proposed during the derivation of equation 1.3 is still valid.

1.4.2 Equation of motion for inclusions

The finite extent of the fluid medium and the high velocities at which the particle would traverse the length of the orifice means that the equation would be a combination of the Stokesian drag by the undisturbed ambient flow but also the disturbance that the particle creates within the fluid. Had the fluid flow within the orifice been slow enough to approximate a creeping flow, the drag force could have been represented simply as

$$6\pi\mu_f d u_p(t)$$

Where μ_f is the dynamic viscosity of the liquid

$u_p(t)$ is the instantaneous particle velocity

d is the radius of the particle

However it was understood that two extra terms needed to be considered for the relatively high Reynolds number flows encountered within the orifice, one is the added mass term and the other is a Basset history force term generated by the transient formation of momentum boundary layers on the surface of the particle. Though quite a few expressions for the added mass term have been proposed over time, Mei Li used one put forward by Auton (ref 24), which can be expressed as

$$\left(\frac{1}{2}\right) m_f \left(\frac{D\mathbf{u}}{Dt} - \frac{d\mathbf{u}_p}{dt} \right)$$

Where m_f is the fluid mass displaced by the particle

d/dt represents a time derivative following a moving particle and D/Dt is a time derivative following a moving element.

$\mathbf{u}_p(u_p, v_p)$ and $\mathbf{u}(u, v)$ represent the respective instantaneous velocity of the particle and the undisturbed fluid velocity at the centre of the particle that would apply in the absence of the particle.

Since the electromagnetic force on the particle must be included for LiMCA systems, predictions on the trajectories of a spherical rigid, particle of arbitrary conductivity is made, by defining a dependence term of the electromagnetic force on the particle and fluid conductivity, this term would later appear in the final equation of motion.

$$\chi = \frac{3\sigma_{ep}}{3\sigma_e + 3\sigma_{ep}}$$

Where σ_{ep} and σ_e are the conductivity of the particle and fluid respectively

The drag coefficient for the particle C_D was given by the steady standard drag curve by Clift et al, based on the particle Reynolds number

$$Re_p = \frac{\rho_f |\bar{u} - \bar{u}_p|}{\mu_f} \quad [1.21]$$

However, the presence of the orifice walls in close proximity to the moving particle will alter the drag force. Fayon and Happel (ref 25) approximated a modified drag coefficient when the fluid is not of infinite extent.

$$C_D = C_{D\infty} + \left(\frac{24}{Re_p}\right)(W - 1) \quad [1.22]$$

Where $C_{D\infty}$ is the drag coefficient in absence of the wall and the value of W is given by

Haberman and Sayre (ref 26) as

$$W = \frac{1 - 0.75857k^5}{1 - 2.1050k + 2.0865k^3 - 1.7068k^5 + 0.72603k^6} \quad [1.23]$$

$$k=f/D$$

So the final equation for the motion of the particle through the LiMCA ESZ becomes (ref 10-12,23,27)

$$\begin{aligned} \rho_p V_p \frac{d\mathbf{u}_p}{dt} = & \frac{1}{2} C_{Dstd} \pi a^2 \rho_f |\mathbf{u} - \mathbf{u}_p| (\mathbf{u} - \mathbf{u}_p) + \frac{1}{2} \rho_f V_p \left(\frac{D\mathbf{u}}{Dt} - \frac{d\mathbf{u}_p}{dt} \right) + \rho_f V_p \frac{D\mathbf{u}}{Dt} \\ & + 6a^2 (\pi \mu_f \rho_f)^{1/2} \int_0^t \frac{d(\mathbf{u} - \mathbf{u}_p)/d\tau}{(t - \tau)^{1/2}} d\tau + V_p (\rho_p - \rho_f) \mathbf{g} - \frac{3(1 - \lambda)}{4} V_p \mathbf{F}_e \end{aligned}$$

[1.24]

As a result of these numerical simulations, a number of interesting aspects of the particle's motion were observed which have not yet been detected in physical experiments. The strong Lorentz force developed in a circular cylinder was used (ref 23) to propose a modified detector tube ineptly termed the “smart probe”. As orifice clogging by larger particles or gas bubbles was always a problem after a de-gassing unit in aluminum processing, the proposal was to add a long collar type extension in front of the orifice. Larger, low density particles (or bubbles) approaching the orifice would experience a large body force that would drive them to the walls of the collar away from the orifice, while the smaller solid particles would be free to pass through the orifice. Figure 1.11 shows a schematic of a “Smarter Probe” (ref 28).

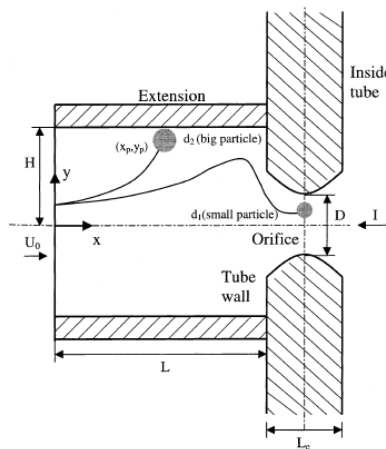


Figure 1.11 – Schematic of the “Smart Probe” designed by Mei Li and R.I.L. Guthrie.

1.5.0 Development of Coulter Counters 1953-1986 (patent review)

The chronological development of the LiMCA technique can best be depicted by a thorough study of the numerous patents that were filed over the years. From 1953 to the present year, well over 50 individual patents have been filed, but in spite of recent improvements from use of better designed sensors, to solid state electronics for improved signal processing, the basic principle and apparatus for the device has changed little.

The first claims of developing a particle counter can be traced to an inventor W.H. Coulter (ref 29) in the fall of 1953. His invention in his own words provided a “Means for counting particles suspended in a fluid”. In the patent, Coulter describes the first designs of an apparatus that can detect particles using the Electric Sensing Zone principle; his simplest arrangement consisted of two glass vessels interconnected by a tube of narrow bore. Though he mentions no working relation between the signal height and size of the particle, correct physical principles are emphasized as to how the difference between the conductivity of the fluid and the particle gives rise to the peaks. It must be emphasized here that all available literature on Coulter Counters were mostly aimed at biological use like counting blood cells, or bacteria, in water.

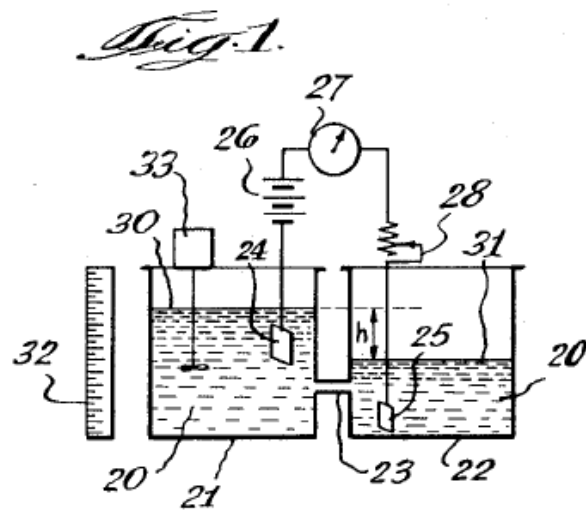


Figure 1.12- Apparatus described by Coulter in the original patent filed in 1953

But the most important contribution of the 1953 patent, was the design of a more robust sensor, where the fluid was not separated in two separate vessels, but between the interior and outside of a test-tube, with a small hole at the tube wall acting as the current path through the fluid. This simple but robust arrangement was used and refined in several future works, and is the most common form of the Coulter Counter till date. In 1964, Coulter (ref 30) and his co-workers designed a more scientifically accurate counting element, in his continuing work on his particle analyzer. The flow of a particle through the orifice being driven by a pressure difference in the fluid on either side of the hole, the rate of aspiration becomes an important parameter to consider during the use of Coulter Counters. Earlier setups relied on differences in liquid heights as the driving force for fluid movement, but as the flow progressed, the fluid levels changed, and so did the flow rate through the orifice. Coulter corrected the problem, by adding a syringe type arrangement, where the piston was pulled out at a constant speed by a weight, thereby ensuring constant flow through a sapphire orifice. Improvement was also made on the orifice by using a small and thin glass disk, with an accurately drilled hole, fused on the side-walls of the tube. All this was aimed towards more accurately being able to count the concentration of particles in the said suspension.

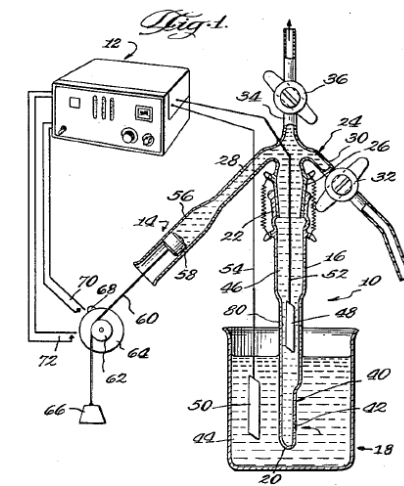


Figure 1.13 – Coulter’s improved design showing syringe and weight arrangement to ensure constant aspiration rate through the orifice.

Accuracy of the measurement technique was improved by Coulter and Henderson (ref 31), as they devised a method which directly measured the volume of the fluid passing through the orifice that does not rely on indirect techniques using known flow rates. This was achieved by using improvised mercury contact switches, the flowing fluid displaced an equal volume of mercury into a tube, where the moving column of mercury made contact with pins placed along the tube. The signals produced when the mercury flowed through the tube, were an indication of the volume of fluid aspirated through the orifice. Until the 1960s, all uses of Coulter counters were restricted to its use in off-line measurements, where constant volumes of solutions were tested for their particle concentration.

In the year 1967, Coulter (ref 32) himself made the first attempt to develop an online variant of his counter which he called “Flow through sample apparatus for use with electrical particle study device”. The disclosed design was complex, and there is little evidence that the apparatus he described was ever put to general use, but Coulter and his co-workers correctly laid emphasis on two important aspects necessary for development of an online variant of the device. Firstly, to maintain, a constant flow rate through the orifice at all times, and to remove fluid from the vessel, as flow is continued non-stop. Coulter solved the problem by using a reliable source of vacuum, and to collect the fluid in a run-off reservoir. In our current project, the development of an on-line particle detection system was also hindered by these two factors, which were first solved four decades ago.

Development of Coulter Counters between 1968 and 1986, can be categorized into the following

- Improvement of the detector element
- Signal processing and algorithm development

1.5.1 Improvement in detector design

As mentioned, the use of the Coulter Counter was limited to biological applications, and consequently, all development was channeled towards this usage. Since the current article is more concerned with its use in metallurgical

applications, a rather brief discussion follows about the several types of detector units that were designed mainly for use with biological specimens.

Between 1968 and 1973 (ref 33-37), Coulter and Hogg, patented a number of different designs for the original counter. Underlying their new designs was the claim that we have better signal strength and lower noise levels, if the electrodes be brought very close to the orifice, as far as practicable, without actually blocking the orifice. This led to the idea of placing silver electrodes flush against the sides of the test tube. Coulter proposed using rings and thimbles which fit snugly against the walls of the tube, as electrodes, while Hogg used silvering techniques to deposit a thin layer of silver on the tube walls, to act as electrodes. Hogg (ref 33) in 1972 made an important modification to the normal test tube and differential pressure design of the Coulter Counter, to use it for online measurements of solutions flowing through a pipe. Differential pressure across the orifice was created by fitting a modified Venturi tube across the flowing liquid. Many modern instruments for analyzing solid suspensions use very similar arrangements with little or no modification.

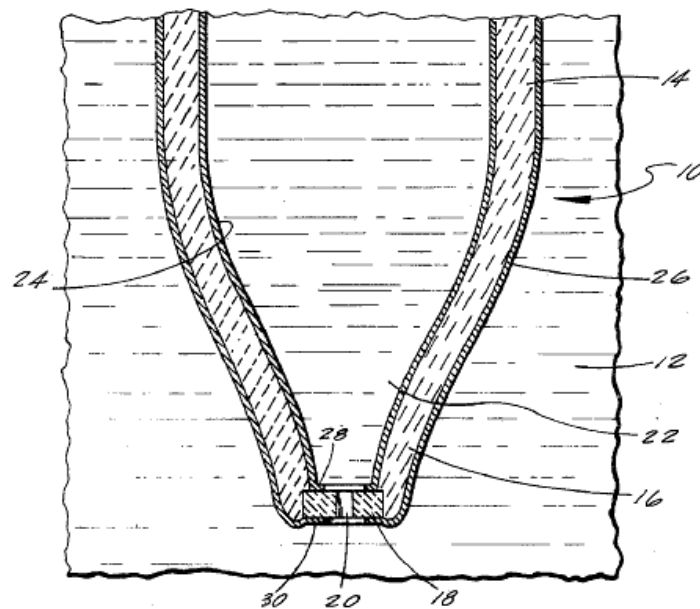


Figure 1.14 – Schematic showing the 1973 design of Coulter's bottom aspirated detector tube

Coulter's further contributions includes the designs of the first bottom aspirated detector tubes (ref 34). Though later research would show that bottom and side aspirated detector tubes have different behaviors, Coulter however gives little, if any, justification of why he considered the bottom aspirated tube as an improvement over the earlier designs. The 1973 patent also mentions the use of alternating high frequency currents, instead of DC voltages, to minimize the effects of polarization in the circuit. But no previous literature published by Coulter depicts any necessary circuitry, which could have used alternating voltages across the tube. In the same year an isolated patent was filed by Jacques A Pontigny (ref 38) which claimed higher accuracy of the Coulter Counter by employing what he described as "an isolated manometer". The principle of operation was identical to that invented by Coulter in the 1950s utilizing a volume measuring setup; making the test liquid displace a volume of mercury along a glass tube lined with electrical contacts. When the mercury flowed past them, they produced signals which were an indication of the volume of fluid tested. Pontigny simply replaced the mercury with a conductive electrolyte, and used an inelastic and impermeable membrane to isolate the electrolyte and the test liquid. However exactly what provided the impetus for this development was never mentioned clearly in the patent, neither are the advantages over the earlier mercury based counters mentioned

A constant problem which always plagued the Coulter Counters was clogging of the microscopic pore, or ESZ, which is essential for the ESZ principle. Archives do show that some patents of less significance were assigned to Coulter Electronics Inc. (ref 39-41) utilizing meshes and screens in front of the pores to decrease the chances of potentially large particles compared to the pore, from clogging the same. However, the most ingenious plan was developed by Coulter (ref 42) himself in the summer of 1976; he used a direct current, high voltage discharge across the electrodes of his counter. The high current pulse flowed through the small pore in the counter generating high amounts of joule heating. This sudden build up of heat would instantly vaporize the liquid inside the ESZ resulting in a small explosion, powerful enough to dislodge any clogged

up particle. Coulter claimed that this microburst did not damage the orifice in any way and can be used as effective means of freeing up clogged up counters.

As mentioned before, Coulter Counters in the 70s were primarily being used in biological applications, and making offline particle counts in fluids like blood, milk etc. The volume of the fluids being tested were essentially very small, and considering the intricacies inherent to the sensor hardware, it was extremely laborious to clean the last traces of the previous fluid before a new sample could be tested. Thomas J Goudin (ref 43) in 1976 solved this issue with an elaborate and complicated apparatus which maintained a constant flow rate of a clean electrolyte through the orifice. When samples were to be tested, extremely small volumes of the fluid were added upstream to the orifice, which would mix with the flowing electrolyte and pass through. The working principle was same, but it had two important advantages; first since there was a constant flow of clean fluid through the apparatus, it was self cleaning, and second very small volumes of fluids could be tested in rapid succession. Many modern commercial hospital equipments are based on a similar apparatus. Between 1977 and '85, Hogg, Simpson and Groves (ref 42-46) made several improvements to the Counter design, incorporating an optical arrangement to correlate the data by a visual particle count, using diffracted light from the particles using a microscope (ref 44). Hogg's proposal consisted to attaching 4 separate counters in tandem, or series (ref 45). The idea was that it would eliminate false peaks. If the peak was due to a particle, then it would show up in all the four signals. In 1983, we have the first patent application showing the use of ESZ counters in molten metals, and this aspect is something that is still being researched to date, and has been dealt with more detail in later sections.

1.5.2 Signal processing and algorithm development

Right from the very first claims by Coulter, a substantial part of the development of the device was channeled towards developing the electronic counters that would convert the raw signals from the counting device to legible data. The first attempts were made by Coulter in 1966 (ref 49,50). Employing

several amplifiers, and threshold noise filters, a better signal to noise ratio was obtained. This improved signal was then fed to commercially available counters at the time, either mechanical or those operating on principles similar to the decautron type Geiger counters. Since transistors and solid state electronics were not popular at the time, bulky vacuum tubes made up the detector circuits. Though the basic block diagram of the detector still consists of an amplifier, a noise filter and a counter, the advent of modern data acquisition systems, and single substrate amplifiers, have greatly improved their performance.

Fairly sophisticated signal processing was integrated into the Coulter Counters by William Claps (ref 51) in 1973, utilizing a discrimination algorithm that could separate a signal peak from a noise peak. The algorithm relied on the differing rise times between the signal pulse and a noise pulse. Though this method of noise removal had been prevalent in years previous to 1973, this is the first instance of solid state signal processing equipment being used in conjunction with the Coulter counter. With the advent of the digital age and computers being more available to the public, Klein (ref 52), in 1974, first patented a system which relied on a code based algorithm to classify each peak as it passes through the system. He also utilized the all important analogue to digital converter, to interface the analogue signal from the sensor to the digital input format for the computer.

With more control and flexibility of the signal processing equipment, Coulter wasted no time in coming up with another great contribution to his invention. All previous patents filed prior to June 1975 (ref 53-59) used the pulse heights as the sole measurement parameter from the signal. Coulter argued that the pulse height alone gives a fair idea about the particle size only if they are roughly spherical. He correctly laid emphasis on the fact that the width of the pulse height was also a key parameter which depends on the particle length, or more precisely the transit time of the particle in the orifice (ref 60). The fact that the exact pulse shape is a function of not only the particle diameter but also its

aspect ratio was correctly predicted by Coulter, which was only later confirmed by mathematical analysis.

1.6.0 Development of Liquid Metal Cleanliness Analyzers (LiMCA) 1979-2010

The research work began in 1979 with an initial proof of concept test in molten gallium, to see the applicability of the ESZ principle to liquid metals. For particles, silica flour was taken in suspension. The metal to be used had to be a liquid close to room temperatures, while at the same time wet the silica tube. This ruled out the use of Mercury, and the metal of choice was gallium. Oscilloscope traces confirmed that particles of silica were being detected, and the effort was on to develop a working detector suitable for molten aluminum.

By 1983, Prof. R.I.L Guthrie and Don A Dautre (ref 61) had succeeded in adopting the ESZ principle to analyzing non-metallic inclusions in liquid metals and had developed the sensing equipment needed. The name Liquid Metal Cleanliness Analyzer (LiMCA) was coined to differentiate it from Coulter Counters. Surprisingly, the setups devised almost two decades back designed for aqueous media also worked well for the first molten metals studied: zinc, gallium, and aluminum (ref 62). Tubes of borosilicate and later by alumino-silicate, were dipped into a liquid metal bath of molten aluminum, to withdraw a sample, to exhaust it out and to re-fill in a semi-continuous manner during an “aluminum drop”, lasting one to two hours (ref 63). Though there is no reference about the exact quality or noise to signal ratio of the original coulter, theory suggests that it would be far better in molten metal, as the conductive liquid would form an isolating Faraday Cage around the sensor element, thereby greatly decreasing the noise levels in the signals. While there was adequate shielding within the detector tube, once the lead wires emerged out of the sensor, it picked up extraneous noises, and this was particularly troublesome as the height of peaks in the LiMCA signal were very small, in the order of micro-volts. The problem was addressed by attaching the amplifier as close to the detector as practicable to increase the signal

strength such that noise pulses would be much lower in magnitude than the signal peaks.

1.6.1 LiMCA in molten aluminum

The first equipment was tested and used in aluminum, and by 1995, LiMCA II equipment was sold commercially by Bomem Inc for ALCAN to the aluminum industry. Detecting non-metallic inclusions in aluminum had been a concern in the aluminum industry, particularly those devoted to the canning industry which represented 30% of the production of Aluminum. As such the absence of a rapid quality assessment tool for counting inclusions led to ALCAN's active support in the development of LiMCA, "A Rapid Method of Evaluating Molten Metal Cleanliness", as claimed by Doutre himself. (ref 64,65)

In his Doctoral dissertation, Doutre compared and reported on the inaccuracies and time consuming nature of the then prevalent metal cleanliness analysis techniques, such as PoDFA, microscopic examination, and ultrasonics, amongst others. The LiMCA technique, boasted a technology which had both the potential to be more accurate, as well as to be an online monitoring system. The majority of the research was dedicated to the aluminum industry, ending in successful plant trials. Though the process would work smoothly for steel as well, there were technological limitations of developing a suitable detector which can stand the 1600 °C or so temperatures reached in the steel making vessels. With aluminum however, the lower temperatures meant that a detector tube manufactured of alumino-silicate glass would easily withstand the temperature, and a successful online detection system using the LiMCA principle was developed and a working prototype was operating in Jouquiere's Smelter by 1991.

1.6.1.1 Development of LiMCA electrodes

The successful operation of the detector unit would be severely hampered by poor contact between the electrodes and the molten metals. Two criteria were essential for a good electrode material, firstly it should have low solubility in the liquid aluminum, and secondly there should not be any oxide layer on it that

prevents proper wetting of the surface by molten aluminum. Copper and stainless steel were thus ruled out and the best results were obtained using simple steel electrodes. Though the steel eventually dissolved completely in the aluminum, they had a service life of around 10 hours before they needed to be replaced. Later developments lead to the commercial sensors` use of tungsten-tipped electrodes which have a far longer service life in the liquid aluminum.

1.6.1.2 Development of the LiMCA detector tubes

The first detector tubes were constructed with borosilicate glass which could stand up to the corrosive action of the molten aluminum. Doutre devised an ingenious method to manufacture the dimensionally accurate orifice on the tube walls. An initial larger hole was made with a micro drill, and then a microflame torch was used to heat shrink the orifice to its correct size. He produced an orifice of constant dimensions, parabolic geometry and smooth walls.

Follow-up tests were conducted by Doutre also in other metal systems including lead and zinc, where it also performed exactly such as in Gallium or Aluminum. As a result of this preliminary

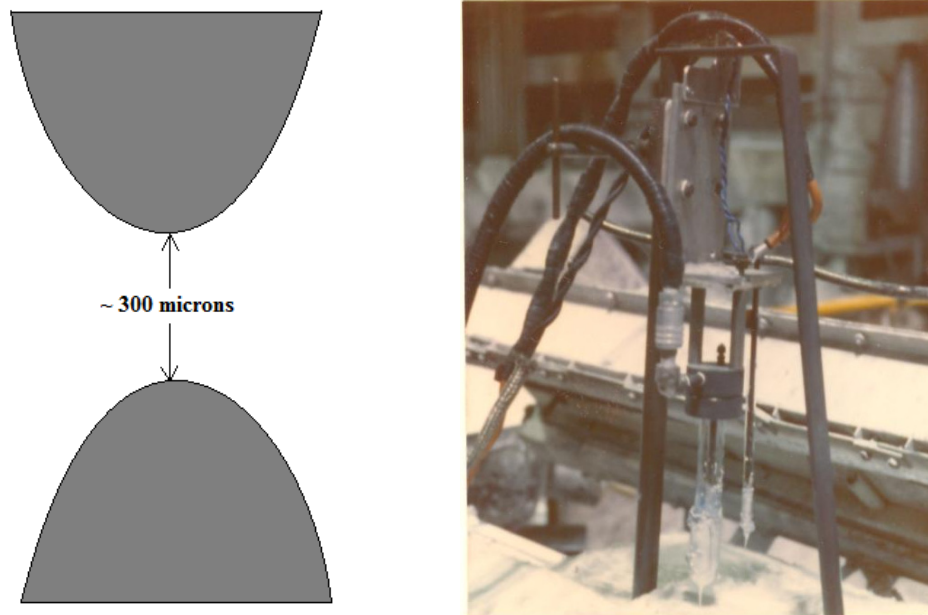


Figure 1.15 – a) Schematic cross section of the orifice used by Doutre

b) Experimental setup used by Doutre for LiMCA in aluminum

investigation, a working LiMCA was developed which counted particles in the size range of 20 to around 200 microns; Figure 1.15 b) shows the image of the experimental setup used by Doutré. In a 1986 patent, Doutré and Guthrie divulged a more detailed design of the setup. A system of pressurized argon and a source of vacuum would be used to draw in samples of molten aluminum within the tube for analysis and then the tube emptied by the pressurized argon gas. Figure 1.16 shows the schematic of the setup designed by Doutré and Guthrie.

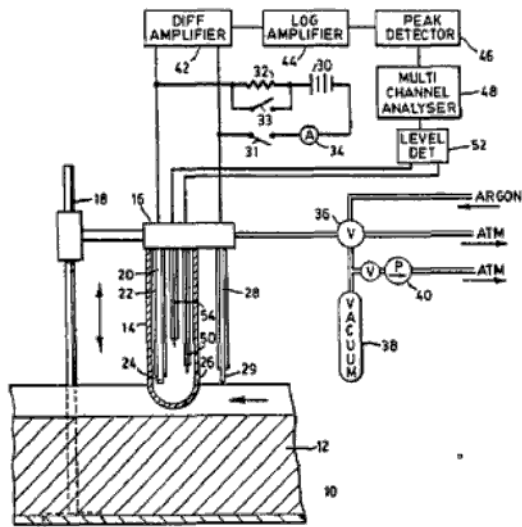


Figure 1.16 - LiMCA for aluminum, design patented by Doutré and Guthrie in 1986

1.6.2 Aqueous Particle Sensor (APS)

While Doutré's contribution towards the LiMCA was aimed at the aluminum industry, S. Tanaka helped by Frank Sebo, MMPC technician, in a 1986 PhD (ref 14) thesis reported on an analogous ESZ system for water models used to investigate of inclusion behavior in water models. The 1986 (ref 61) research thesis divulges greater details about the principles and parameters at work behind the ESZ technique for water. The fact that it worked with a less corrosive environment than molten steel, namely water, a greater understanding was obtained about the importance of amplifier performance, noise removal, and a proper data acquisition algorithm.

The way data was analyzed by the APS (Aqueous Particle Detector) and the Aluminum LiMCA was very similar, involving appropriately chosen bin rules. The various sizes falling within the measurement range of the device were categorized into a convenient number of classes, and the number of particles falling under each class was counted. A pulse height analyzed would determine the height of each peak and use a predetermined relation to convert the voltage readings to particle sizes. This particular mode of approach for the LiMCA data analysis has remained unchanged since then, but how, and the exact algorithm being used to achieve this, has been continuously improved.

At this point, it should be made clear that since in water there is no added difficulty of operating in the high temperatures of molten aluminum, there are other difficulties associated with water arising out of its poor electrical conductivity. The problem was successfully addressed by using appropriate shielding techniques. Coaxial cables were used and the detector tube itself was totally covered with a braided stainless steel braid, with only the orifice region remaining uncovered. One important accidental discovery that came out of these experiments was the beneficial effect of grounding the tundish in helping to drastically reduce the noise level in the signal.

Apart from developing an appropriate particle detector and counter, Tanaka also developed a tundish arrangement, whereby the performance of inclusions could be accurately monitored continuously. He attached two APS probes to a scaled down water model tundish, one at the inlet shroud and the other at one of the submerged entry nozzles. This arrangement was successfully used to obtain tundish performance parameters such as residual ratios of inclusions, performance of flow modifiers, and so on. Figure 1.17 shows the schematic of the arrangement used as shown in the 1986 thesis.

While hot molten aluminum inherently contained non-metallic insulating inclusions, there was a problem with water as it contains no simulator for

inclusions. This problem was addressed with addition of lighter than water, hollow silica bubbles of size range 0 to 200 microns (ref 14). The silica would wet water while at the same time the fact that their effective density was less than that of water means they would tend to float, thereby approximately modeling the behavior of the inclusions in steel. The schematic shows an agitator arrangement in the reservoir containing the particle slurry to maintain a mostly homogenous mixture to be added to the shroud. The effective measurement range for the device used by Tanaka was about 20 to 300 microns. The detector tubes themselves were made of borosilicate test tubes with orifices drilled at the side using a diamond tipped micro drill.

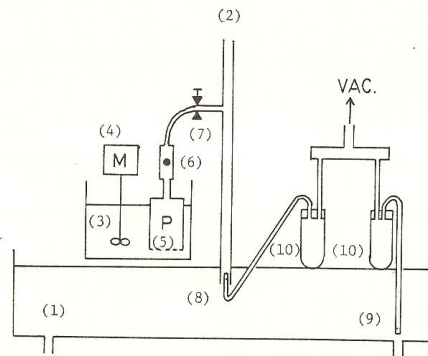


Figure 2.26 Measurement system of residual ratio of particles.

1. tundish
2. inlet nozzle
3. 8 litre vessel
4. stirrer
5. pump
6. flow meter
7. flow control bulb
8. probe 1
9. probe 2
10. water collector

Figure 1.17 - Experimental water model setup used by Tanaka

1.6.3 LiMCA in steel (ESZpas)

Attempts to employ the ESZ principle to develop an online inclusion sensor for molten steel were first attempted by Nakajima at McGill University in the year 1982. (ref 13) The phenomenally high temperatures encountered in steel

making, around 1600 °C, required a completely revised materials and operational approach. While the data-acquisition electronics and data-analysis techniques remained very similar to those of previous setups, considerable advances were made with the probe design. The alumino-silicate tubes had to be replaced by fused quartz (silica) tubes. While materials like boron nitride were available having higher refractoriness as compared to silica, the latter was preferred as molten steel wets silica and produced a better signal as the steel flowed through the orifice. The high temperature had the undesirable effect of softening the silica tube however. This became

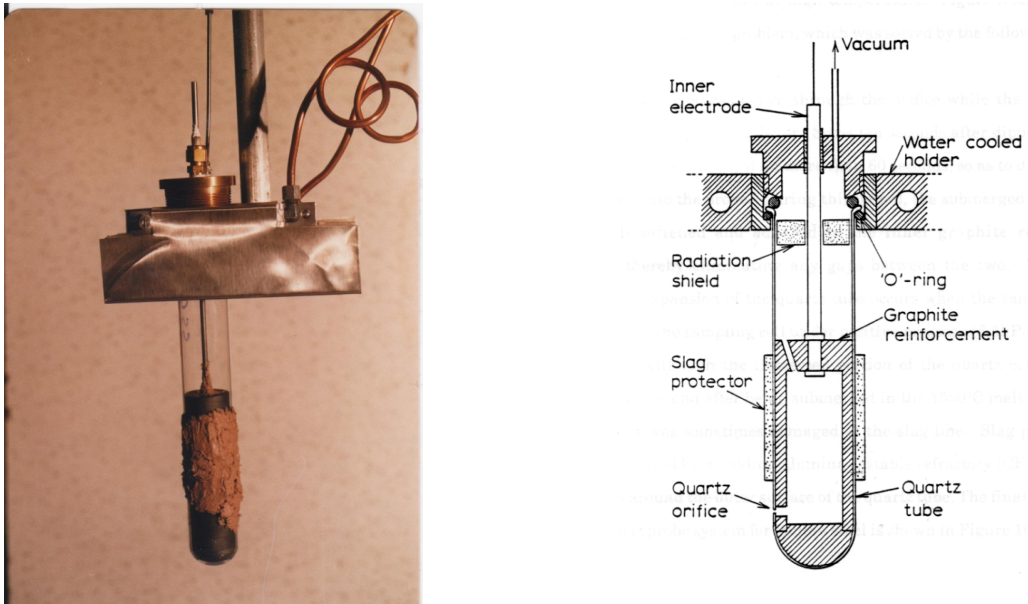


Figure 1.18 – a) Final appearance of the detector tube developed, b) schematic of the construction apparent when a positive or negative pressure was applied to the tube, either to start sampling (negative pressure to draw in the metal) or during probe positioning (positive pressure to stop the orifice from clogging), where the probe either tended to collapse or to enlarge. The problem was solved by reinforcing the sides of the tube with graphite cylinders. The lining graphite cylinders also doubled as the electrodes. Similar to the setup patented by Dautre and Guthrie for aluminum, the steel variant also relied on the alternate application of vacuum and high pressure argon gas to repeatedly draw in the molten metal and then empty the tube. The developed probe generally had a service life of about 30 minutes in the

tundish. Sometimes, as the probe would penetrate the slag layer to sample the metal underneath, the quartz tube would be damaged by the slag. To counteract this problem, a moldable alumina mixture was applied on the exterior of the tube. As the tube would reach the steel, the high temperatures would have destroyed the alumina paste and it would fall off. Figure 1.18a shows the final appearance of the detector probe used by Nakajima in plant tests carried out at Dofasco in their 70 ton tundishes.

As a result of this research, in 1993 Prof. R.I.L. Guthrie (McGill University) in collaboration with H Nakajima, filed two separate patents (ref 68-69) for steel inclusion sensors, the first a continuous use variant very similar to that described by Nakajima in his PhD work, and a second more advanced variety, of a disposable nature, (single use device). The essentials of the two devices were identical. With the continuous use variety, the initial establishment cost was high as an elaborate system of vacuum and high pressure argon gas was to be made. A single use disposable detector on the other hand was cheaper to use as only a data logger and the probe was enough for the tests, and the detector probe had to survive just 1 to 2 minutes in the liquid steel

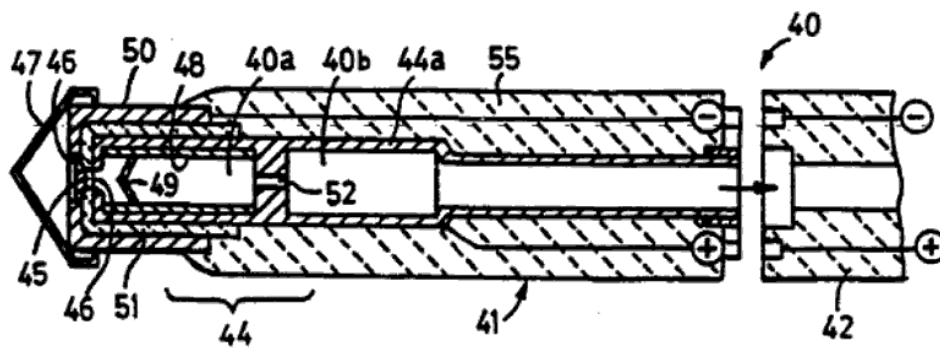


Figure 1.19 - Single use disposable inclusion detector patented in 1993

The tube was identical in construction, but the orifice was sealed by a protective seal so as to pass through the slag phase over the steel. First the tube was

evacuated and then the orifice sealed. As the probe would enter the metal, the seal would melt away, when the pre-sealed vacuum within the tube would draw the metal inside. However, to make sure that the metal does not reach the holder and destroy it, a chill block was placed at a predetermined position along the tube. A small hole would allow the vacuum to draw the metal, but once it reaches the block, it would freeze, and stop the device from drawing in more metal. This ingenious arrangement was also a way to accurately control the amount of metal being sampled in each experiment. The tube itself would be covered in a layer of easily meltable material. This layer would protect the tube as it would penetrate the slag layer, but as it reaches the metal, the high temperature would melt it away, exposing the tube and orifice to the molten metal.

1.6.3.1 Electrode design for steel LiMCA

Proper electrode design for use in steel was a challenge to start with. Graphite performed well at the high temperatures and steel did wet the graphite surface, but there was a problem with steel containing dissolved oxygen, as it tended to form carbon monoxide bubbles on the surface of the graphite. These bubbles would tend to add noise to the signal. Eventually electrodes were made with refractory metals like tungsten or molybdenum. They had a tendency to be wetted by the molten steel, and because of their finite solubility in steel, they would slowly dissolve in the steel thereby ensuring a good electrical contact between the steel and the electrode.

1.6.3.2 Development of the detector tubes

Detector tubes manufactured for steel were identical to those used by Doutre in terms of basic design but were made of silica tubes closed at one end. However a different technique was adopted to create the detector orifice than the drill and heat shrink technique used earlier. For the steel detectors developed by Heraeus Electro-Nite, a laser pulse was used to bore the orifice on the side of the

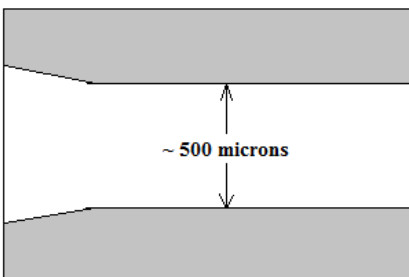


Figure 1.20 - Schematic cross section of the orifice used in LiMCA for steel

tube. The end of the orifice pointing out of the tube tends to be slightly fluted; this showed the effect of improving the noise characteristic of the signal generated by the detector. Figure 1.20 shows the schematic of the orifice used.

Apart from application of LiMCA in aluminum and steel systems, Selcuk Kuyucak (ref 70,71) studied its suitability in molten copper and magnesium. The stability of silica glass sampling tubes and the orifice was found to be good in alloys containing at least 0.02% beryllium. This was attributed to the formation of a protective oxide layer on the surface of the silica glass. The research work by Kuyucak showed that similar LiMCA equipment could be effectively used to determine final metal quality and its cleanliness in both magnesium and copper systems.

1.7.0 Performance comparison of LiMCA

With a relatively in-depth review of the development of the LiMCA technique spanning three decades, a cursory performance comparison with other commercial liquid metal quality analyzers is definitely called for. While a number of liquid metal quality sensors are available commercially which measure anything from melt temperature to dissolved hydrogen content, only a few techniques exist that give an estimate about the amount of non metallic particles in the melt. The following alternative techniques fall into this category

- Porous Disc Filtration Apparatus (PodFA)
- Microstructural/microscopic analysis
- Ultrasonic techniques

1.7.1 Porous Disk Filtration Apparatus (PodFA)

The method basically consists of filtering a sample of molten metal (primarily aluminum alloys) through a porous sintered silicon carbide filter. The non metallic inclusions are retained within the surface of the filter, and a microscopic analysis of the sample gives an indication about the inclusion content of the metal. Another similar technique is the LAIS or Liquid Aluminum Inclusion Sampler, and is used for faster measurements. The technique is very similar to the off-line PodFA, but makes the process on-line, by placing the filter at the end of a small canister which contains a sealed vacuum, as the canister is lowered into the flowing metal, the liquid aluminum flows into the vacuum, passing through the filter where the inclusions are retained in the form of a compact cake. The filter is then removed, frozen and examined for the captured inclusions. (ref 72)

While these techniques are common, they suffer a number of drawbacks,

- The process fails if there are a large number of inclusions in the metal. The inclusions retained by the filter forms a sort of porous cake on the silicon carbide surface thereby modifying the porosity and sieve size of the original filter. During the microscopic examination, it becomes possible that particles retained in the filter could be retained not by the filter itself but the porous layer of inclusions on the surface. Also alumina films forming on the disc leads to clogging and changes the filtration characteristics of the porous disk on which the technique relies.
- The process cannot give an exact indication of the size distribution and number of inclusions detected, but can give a rough estimate about the volume fraction of the inclusions in the melt.
- It is a very time consuming process requiring a lengthy process of microscopic examination (ref 73,74)
- The process is severely dependant on the visual interpretation of the cakes by individual operators and their habits and techniques.

Figure 1.21 shows representative samples showing inclusions and the 'cake' area at 200x magnification.

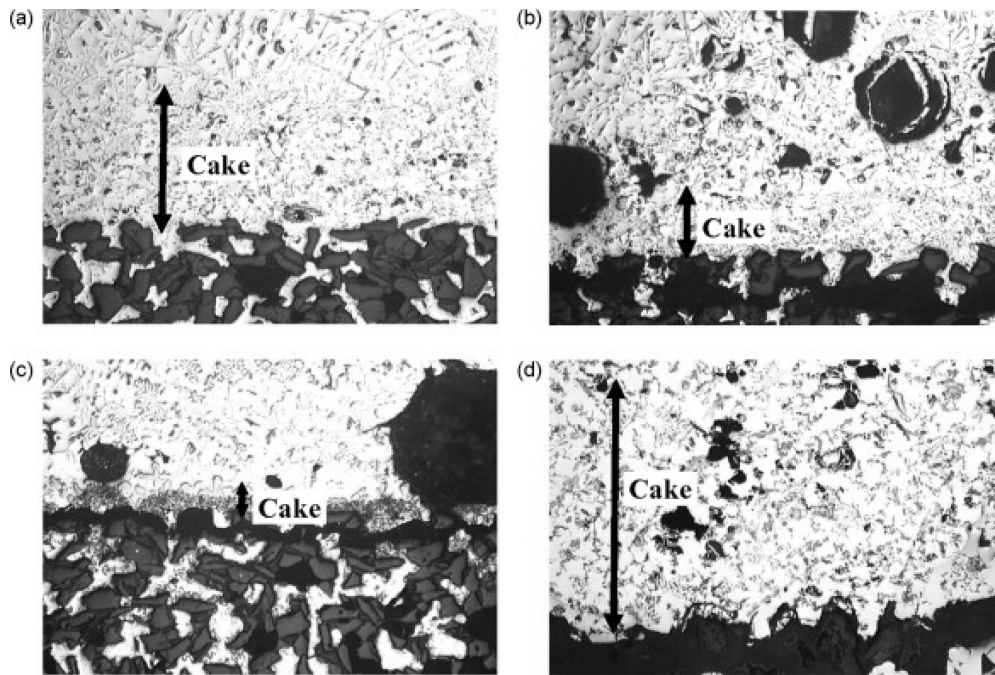


Figure 1.21 - Representative micrographs of PodFA samples

1.7.2 Metallurgical and microscopic analysis

Metallurgical analysis is the most concrete and straight-forward metal cleanliness analysis that can be used. It basically consists of microscopic analysis, either optical or electronic, of a cast and subsequently polished section of the metal. The method is relatively accurate in detecting non-metallic inclusions, of varying size ranges and morphologies. However the method is extremely time consuming and requires the knowledge of metallographic surface preparation and expensive microscopes. Another method of metallurgical analysis consists of examination of a fracture surface of the cast metal. Similar to the Charpy tests in steel, a notched bar cast with the alloy in question is fractured and the fracture surface examined with the naked eye, or a low powered (4x) microscope. By this process only the presence of Macro-inclusions can be detected but a well trained eye can make a fairly accurate, but subjective estimation of the metal cleanliness.

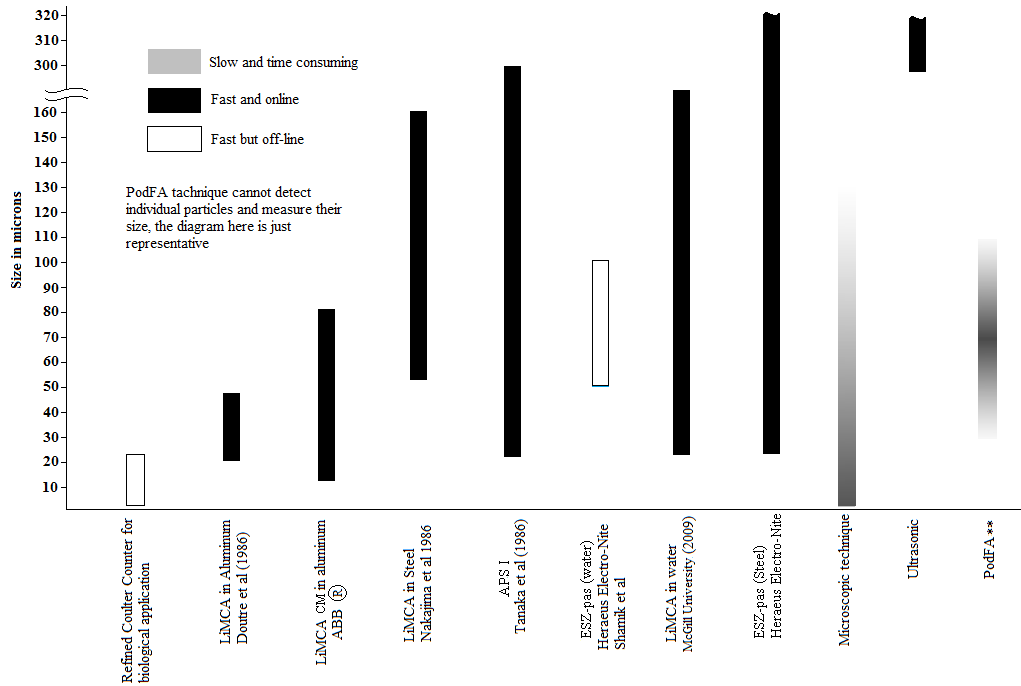


Figure 1.22 - Performance characteristics of LiMCA apparatus developed to date

1.7.3 Ultrasonic techniques

Ultrasonic cleanliness analyzers are mainly designed for liquid aluminum and steel, where non-metallic inclusions are detected with ultrasonic backscattered pulse echo signals coming from individual inclusion particles. The technique is claimed to have been developed successfully for Aluminum by the Reynold's Aluminum Company (ref 75). Attempts have been made to develop it for molten steel and iron in the University of Toronto (ref 76, 77). Its attractiveness lies in its ability to provide on-line information on the frequency of macro-inclusions in the melt. As in other instruments that depend on wavelength for detection, only the particles greater than half the signal wavelength will cause backscatter, and will be detectable by ultrasonic techniques. This method severely limits the detectable inclusion size in molten metals to 250 microns in molten aluminum for instance, with the presently attainable ultrasound frequencies of 10 MHz. (ref 78)

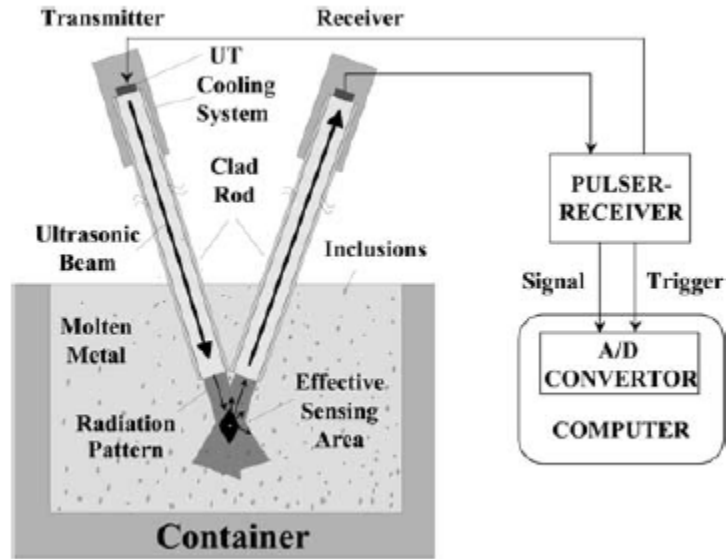


Figure 1.23 - Schematic of an Ultrasonic inclusion detector

From the above comparison it is apparent that the LiMCA technique is the ideal liquid metal cleanliness measurement device which gives the ideal compromise between speed of operation and measurement range. Figure 22 is a comparison chart showing the performance characteristics of the LiMCA devices developed to date.

1.8.0 Conclusion

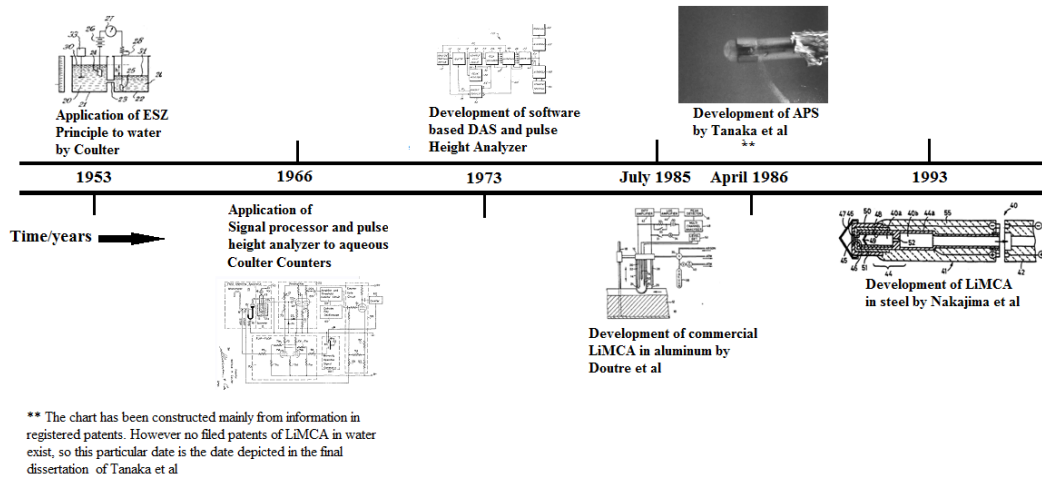


Figure 1.24 - Time line showing important milestones in LiMCA development

The review presented here aims to put into perspective, the discovery and development of Liquid Metal Cleanliness Analyzers (LiMCA) from their initial development to final application, over a period of three decades. As a system which relies on physics, metallurgy, signal processing and electronics, multi-disciplinary knowledge was always necessary to make the system work, and that is possibly why it has taken such a long span of time to reach its current state of development. Commercial variants of the original LiMCA in aluminum have been commercialized and marketed by Bomem, ABB (ref 79) and Alcan and the LiMCA research group at McGill University. Heraeus Electro-Nite markets a commercial variant of LiMCA meant for liquid steel named ESZpas, though it has less popularity in the steel industry as compared to aluminum. Though LiMCA has indeed come a long way, there remains a lot of further improvement that is called for, especially in liquid steel applications, where it needs



Figure 1.25 - a) LiMCA CM manufactured by ABB for molten aluminum,
b) Commercial ESZpas (LiMCA) for liquid steel by Heraeus Electro-Nite

to be marketed to its full potential. While previous researchers have predicted that the LIMCA principle can also be utilized to differentiate between solid inclusions, small liquid droplets and air micro-bubbles, no robust algorithm or codes have yet been definitively developed, and this is clearly one of the areas where future research activities can be channeled.

Development of Aqueous Particle Sensor III

2.1.0 Introduction

Research aimed at process engineering of steel making and/or refining operations have gained importance over the years, in an attempt to develop methods that are superior, both in terms of quality of final product as well as efficiency. However, due to the high cost of setting up pilot plants, as well as technical difficulties associated with working in the high temperature environments, researchers have long turned to physical modeling tests using water analogues. Comparison of dimensionless numbers like Reynolds number, or Froude number, ensures that the flow fields of the working fluids (ref 80) (liquid metal in the plant, and water in the physical models) are identical. Study of inclusion behavior in metal systems is also carried out in water trials by adding simulated inclusions within the liquid, such as small buyout particles (microspheres) of glass. The movement of these inclusions within the fluid is studied with appropriate particle detection devices.

2.2.0 Aqueous particle detection system

The **McGill Metals Processing Centre (MMPC)**, at McGill University, Montreal, has long conducted such water modeling tests both for novel research as well as routine testing for industrial firms, and has put to use a number of particle detection devices to study inclusion behavior in water trials. Routine testing using aqueous particle sensing devices was started with a device called APS II (ref 71, 72) which worked on analogue principles. The current such instrument being used is one manufactured by Heraeus Electro-Nite, and was an adaptation of McGill's **Aqueous Particle Sensor (APS) II** (ref 81). While MMPC has carried out experiments using the Heraeus sensor in the past ten years, it suffers from some demerit points, which are listed below.

- The size range of particles that it is capable of measuring is quite limited, namely 60 to 100 microns.

- Measurements can only be made on small samples of water collected during testing. That is to say, all measurements had to be made off-line from the actual water modeling experiments. The construction of the detector was such that it could take measurements only from samples placed in small vessels like glass beakers.
- The complexity and relatively large size of the manufactured device prevented researchers from making any operational changes or modifications to the instrument.

The computer handling the user input interface and the operational parts of the particle detector were integrated into one device, since detailed circuit diagrams were unavailable, the versatility of the instrument was severely reduced.

Efforts were thus recently channeled into developing a new APS III within the MMPC group based on the initial principles and ideas. The new instrument would not only have superior performance over the Heraeus Electro-Nite device, but would also be amenable to changes and modifications made by the researchers working with it.

2.3.0 Working design

The basic design of the detector commonly used at McGill University was the tried and tested side-aspirated borosilicate tubes. The orifice can be either drilled or laser bored into the side of a closed ended tube and a differential pressure within the tube is used to continuously draw the liquid in and force out of the orifice (Figure 2.1a). Figure 2.1 shows the working principle of the device. The fluid containing a suspension of the inclusion particles is allowed to pass through a narrow orifice. The two electrodes are used so as to apply the necessary constant electrical current supply (I) through it. As explained in previous sections, as a particle passes through the orifice, it shows up as a jump in the voltage across the electrodes (Figure 2.1d) and this is digitally recorded. Its magnitude is an indication as to the size of particle (ref 9-11). It should be noted that the transit time of the particle through the orifice is extremely small (~ 1 ms), so if the

recorded times for detection of signals is of any modest time length (20 seconds or more), then the width of the peak relative to the entire train of signal becomes extremely small, and we end up with a signal as shown in Figure 2.1b, i.e. each particle being detected shows up as a narrow transient voltage spike.

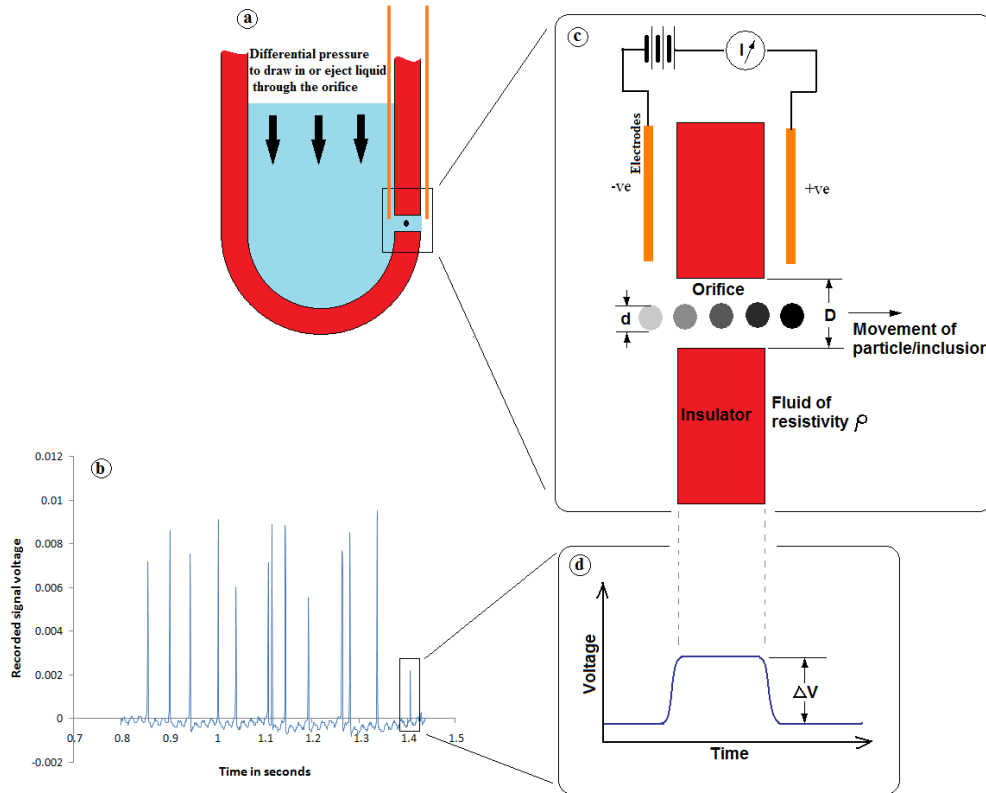


Figure 2.1 - Electric sensing zone principle operating in the detector

2.3.1 The APS equation adopted

Obviously, during actual measurements for discrete particles within an Electric Sensing Zone (ESZ), the number of peaks detected is normally equal to the number of particles sampled, and the height of the peaks is related to the particle sizes by equation 2.1 (ref 12).

$$\Delta V = \frac{4\rho_e I d^3}{\pi D^4} \quad [2.1] \quad \text{or,} \quad \Delta V = k d^3 \quad [2.2]$$

where ΔV is the change in voltage when the particle passes through the orifice

ρ_e is the electrical resistivity of the working fluid

I is the constant current flowing through the orifice

d is the diameter of the particle

D is the diameter of the orifice

$$k \text{ is a constant} = \frac{4\rho_e I}{\pi D^4}$$

The above equation was derived from Maxwell's approximations, that the particles are so dispersed in the medium that they do not in any way alter the electric field within the orifice except at positions near the particle surface. The individual voltage peaks in the signal are, however, far too small in magnitude to be accurately measured by a data acquisition system, so the raw signals from the detector must be amplified linearly by a factor α .

$$\Delta V_{\text{amplified}} = \alpha k d^3 \quad [2.3]$$

The exact value of α was chosen based on an order of magnitude analysis from equation 2.1. Considering a CMOS (Complementary Metal Oxide Semiconductor) data acquisition system being used, a total signal swing of 0 to 5 volts is considered ideal. The amplifier gain is thus chosen so as to get a voltage peak of around 5 volts when the largest particle (in the range of interest) goes through the orifice.

$$\Delta V_{\text{amplified}} \rightarrow 0 \text{ to } 5 \text{ Volts} \sim 0$$

$$d \rightarrow 40 \text{ to } 99 \text{ } \mu\text{m} \sim -5$$

$$D \rightarrow 500 \text{ } \mu\text{m} \sim -4$$

$$\pi \rightarrow 3.14 \sim 1$$

$$\rho_e \rightarrow 0.2 * 10^4 \text{ } \Omega \text{ m} \sim 3$$

$$I \rightarrow 1 \text{ } \mu\text{A} \sim -6$$

$$\langle 0|\alpha + 3 - 6 - 15 - (-16)\rangle$$

or $\alpha \sim 2$

Thus, the gain of the amplifier was chosen to be 100.

2.4.0 Design of new APS sensor probe

Prior to any design innovations, the original APS probe adoption used by Heraeus-Electro Nite was studied and some of its operational limitations analyzed. Figure 2 shows an image of that sensor. An important part of the device is the electrode assembly which applies the excitation current across the orifice, and was the first subsystem to undergo modification.



Figure 2.2 – Image of the detector probe designed by Heraeus Electro-Nite for APS II

The primary impetus for the first modification came from the fact that a new design feature for the APS III would require it to be able to operate under fully submerged conditions. While the older APS II was designed with ease of construction, the setup fails completely when submerged. It should be noted here that the ESZ technique works only when the conduction path between the two electrodes is through the small filament of electrolyte / molten metal passing through the orifice. In the original Heraeus design for liquid steel a small metallic tube acts both as the vacuum feed to draw in the liquid steel (or water), as well acting as a conductor between the inner electrode and the external lead wire. As

can be seen in the schematic in Figure 2.3, when the modified steel probe is completely immersed in water, the external surface of the vacuum lead protruding out of the tube is exposed to the electrolyte and acts as an extension of the internal electrode. This sets up conduction paths between the inner and outer electrodes externally through the fluid, and not through the orifice, thereby rendering the ESZ principle inoperable. The necessary modification for APS III involved electrically isolating the entire inner electrode lead wires and contacts with epoxy and tube insulation. Only the lower portion of the inner electrode was exposed to establish electrical contact with the fluid inside the tube. The metallic vacuum lead was also replaced by one made of insulating material.

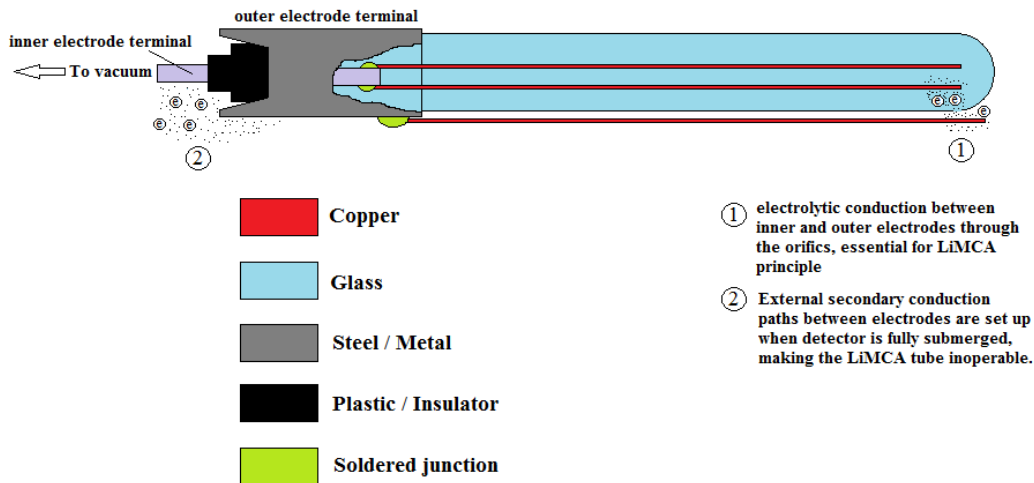


Figure 2.3 – Schematic diagram of the detector probe from APS II showed in Figure 2.1

A second problem with the previous version was discovered during a routine test lasting almost an hour. It was observed that the amount of noise within the signal increased slowly with time. Figure 2.4 shows two 1.5 second signal segments 30 minutes apart.

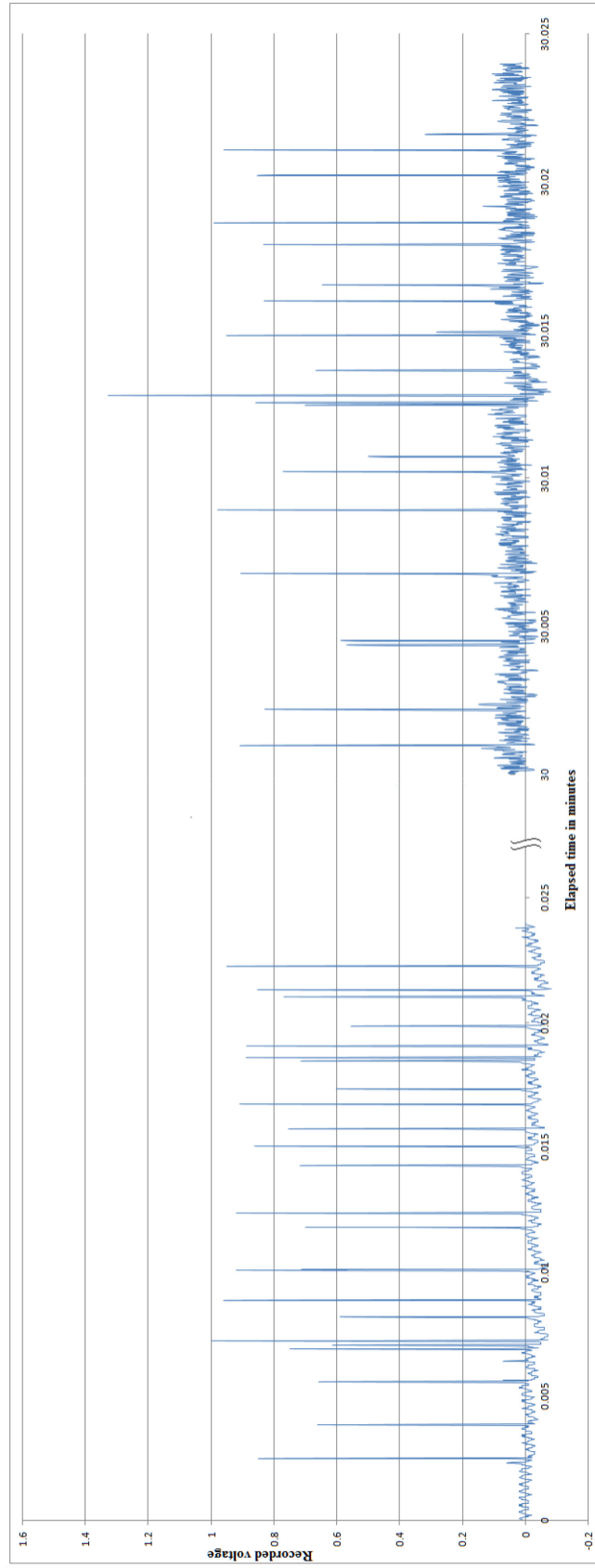


Figure 2.4 – Raw signals showing worsening signal quality with extended usage of the omodified Heraeus Electro-Nite APS detector probe.

Putting two DC excited electrodes in an aqueous environment would tend to electrolyze the water and this tends to buildup small gas bubbles on the surface of the electrodes. The buildup of these small bubbles on the electrode surface was found to be coincident with the increased noise in the electrodes. The fact that these bubbles were contributing to increased noise was also corroborated by the fact that a gentle shake to the sensor to dislodge the bubbles from the electrodes restored the original low noise signals generated at the start of the experiment. An attempt was made to reduce the amount of electrochemical reactions. Decreasing the potential difference would have stopped the electrolysis of water, but would also decrease the signal amplitude. Another way to decrease the bubble buildup was to increase the surface area of the electrodes. A larger surface area meant that even if we have bubbles covering some part of the electrode, we would still have enough part of the surface still exposed to make noise free electrical contact with the fluid. Similarly it also decreases the current density at the electrode surface, decreasing the rate of electrolysis.

The end of the inner electrode was made into a helix of 7 to 8 turns, while the outer electrode was modified into a ring surrounding the helix region of the inner electrode. The ring electrode was also made the ground and effectively doubled as a shield to keep extraneous noise pickup to a minimum. The material for the electrode was kept the same (copper). Prolonged use of a detector would tend to corrode the electrodes and this becomes apparent if it is operated in a small volume of stagnant fluid, when it takes on a faint green tinge due to dissolved copper salts. This slow corrosion of copper was actually advantageous because it always exposed a fresh metal surface to make good electrical contact with the electrolyte. The importance of this slow corrosion became apparent when a trial detector was constructed with austenitic stainless steel, and showed widely variable signal quality due to complex interactions between the applied potential and the behavior of the passive oxide films on the electrode surface. The new probe was first modeled using AutoCAD 2004. Figure 2.5a shows the rendered model and Figure 2.5b is the final prototype.

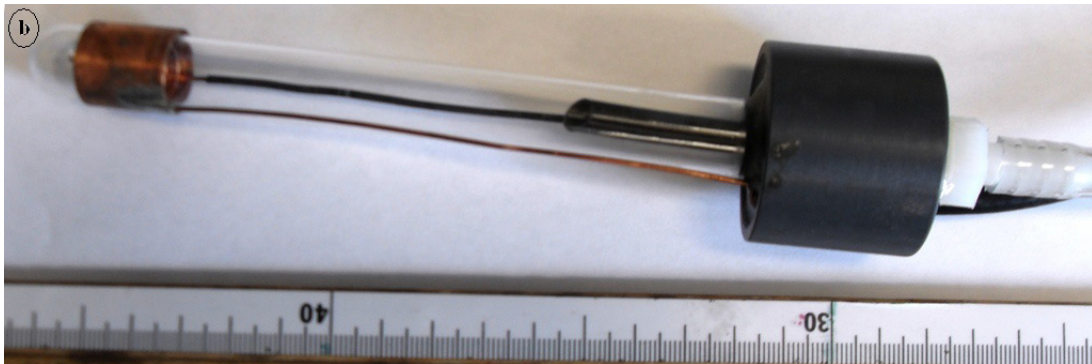
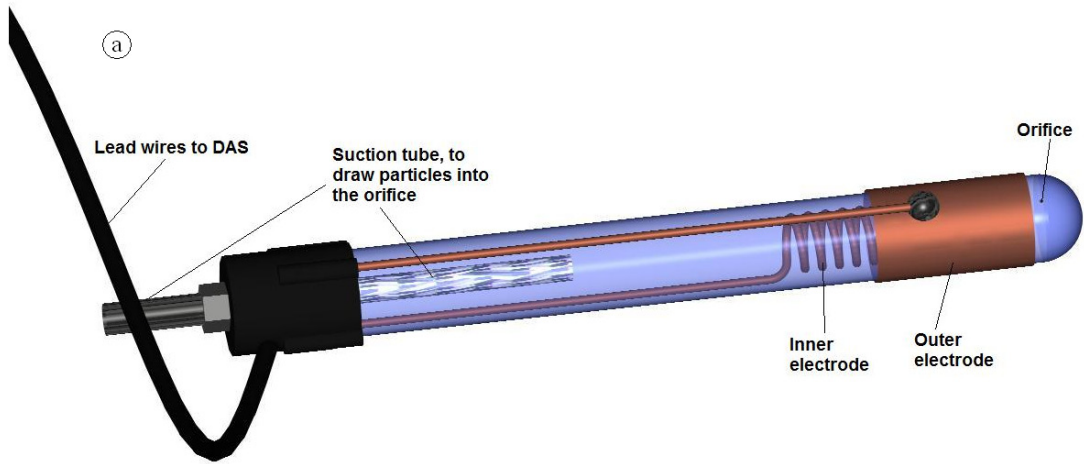


Figure 2.5 – a) CAD Model of the final APS III sensor developed. b) Working prototype for the APS III sensor

2.4.1 Size and shape of orifice

As mentioned in the introduction, the exact size and shape of the orifice is of marked importance in the final operation of the transducer. The tubes used in developing the present versions of the aqueous particle sensor were manufactured of test tube shaped borosilicate glass with the orifice drilled through the side walls close to the bottom. The tubes were manufactured

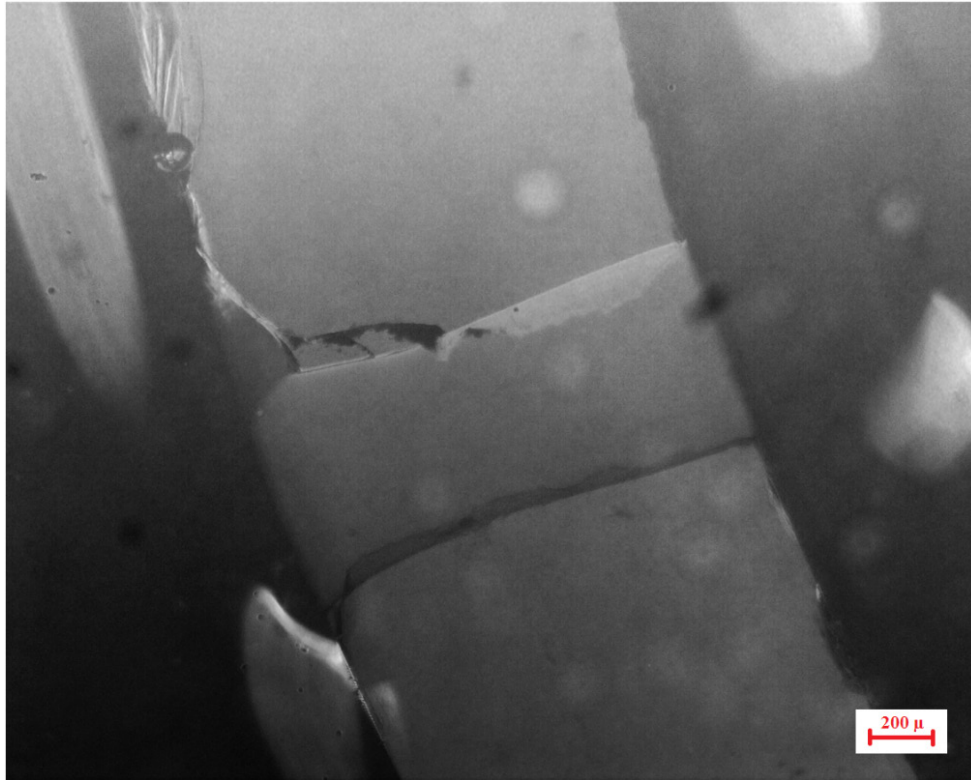


Figure 2.6 – Microscopic view of the APS orifice

by Heraeus Electro-Nite, and were same as those used by them to make the LiMCA sensor for steel. The orifice was bored with the aid of a laser pulse. This resulted in a more or less cylindrical orifice with its exterior end slightly fluted. A number of tube orifices were sectioned and examined microscopically. The average diameter of the cylindrical portion of the orifice was determined to be very close to 500 microns.

2.5.0 Amplifier used

As has been explained earlier, the absence of adequate shielding around the detector tube by the molten metal presents a unique set of challenges for the device as compared to LiMCA for metal, as far as the electronics associated with the system is concerned. Use of high quality 75 Ohm coaxial was used for all external wiring to keep extraneous noise pickup to an absolute minimum. A

fundamental flaw with the older setup was its reliance on a relatively noisy excitation voltage setup across the detector probe. Oscilloscope traces revealed that an appreciable amount of the 50 Hz main component had filtered into the excitation voltage. Though both the computers and amplifiers were housed in shielded metal boxes, the fact that these devices are meant to operate in laboratories which are inherently electrically noisy, meant it was difficult to eliminate the mains hum. However, by isolating the APS detector and associated electronics from any mains driven power supply, and employing dry cells for power, the quality of the excitation voltage was substantially improved. While the maximum amplitude generated by the probe is around 50 mV, adequate amplification ($\alpha \sim 100$) is essential to bring up the maximum amplitude to around 5 Volts before the signal can be fed into the data acquisition system. The small amplitude of the original signal, the transient nature of the peaks generated, and the high gain, places stringent performance demands on the amplifier being used.

- It should have a constant gain over the entire range through which the signal is expected to swing, essentially from zero to around 50 mV.
- High frequency response of the amplifier should be very good owing to the fact that the individual signal peaks last in the order of 1 ms.

The actual amplifier was constructed with an AD 624 single substrate operational amplifier. This particular IC was chosen for its superior performance (ref 82, 83), easy availability and requiring lesser number of supporting external components. The superiority of the device lies in the fact that appropriate feedback mechanisms and filters are integrated within the package and interconnecting appropriate external pins are adequate to set the gain of the device. Figure 2.7 shows the schematic circuit diagram of the amplifier.

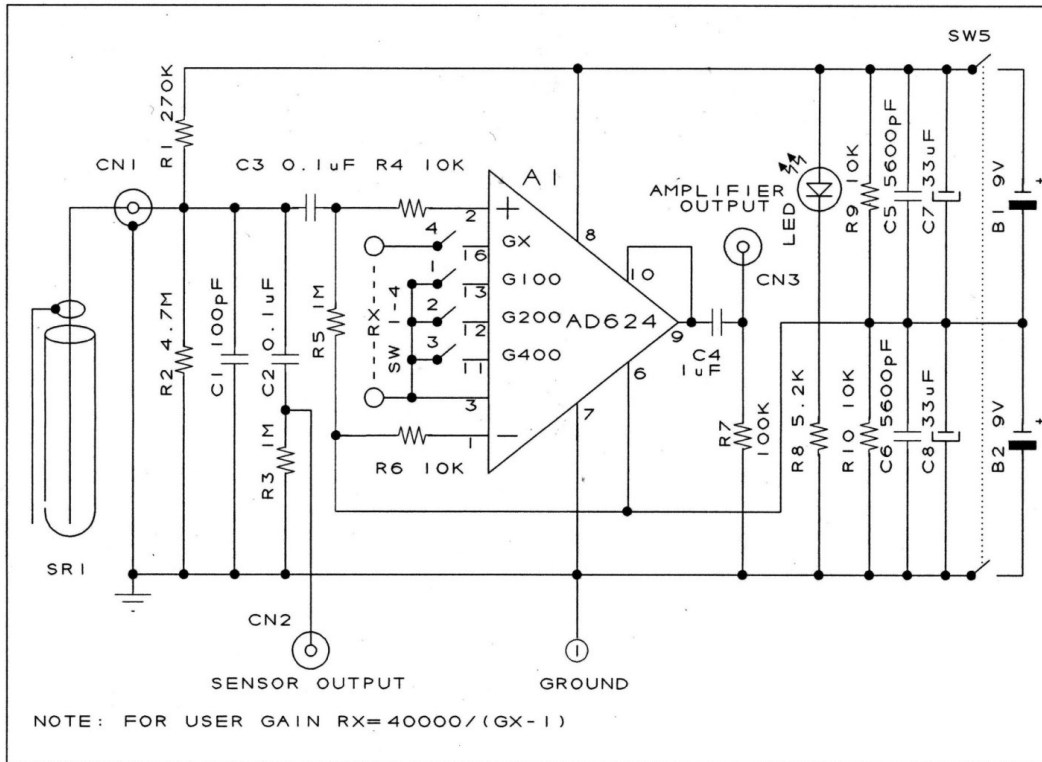


Figure 2.7 – Circuit diagram of the APS III amplifier (ref 83)

Two standard 9 volt dry cells provide both power to the operational amplifier, as well as provide excitation voltage to the transducer. While B1 and B2 provide the necessary bi-polar power supply to the chip, the negative terminal of B2 is grounded instead of its positive terminal (or the negative terminal of B1), as is done with conventional bi-polar power supplies. This was done to utilize the maximum possible potential difference (18 Volts) across the detector tube in order to generate signals with as high an amplitude as possible. Capacitors C7 to C8 and resistors R9 and R10 form part of a smoothing circuit and filter for the power supply. Switch SW 1 to SW 4 form part of the feedback mechanism which lets one select the gain of the device. For our instrument, the gain was kept constant at 100. Potential across the tube is applied via a potential divider consisting of R1 and R2, where R1 acts as the ballast resistor. The final signal from the amplifier is fed to an external CMOS based data acquisition system filtered through a 1 micro Farad capacitor C4 to remove all DC components from the signal.

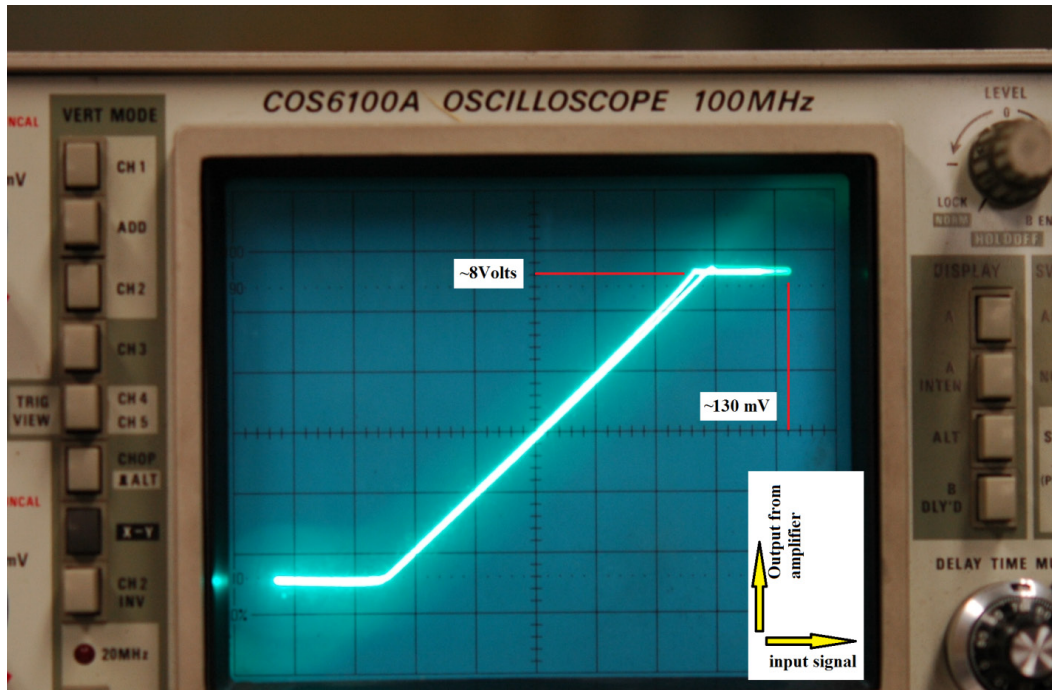


Figure 2.8 – Oscilloscope trace showing performance characteristic of the APS amplifier

The constructed circuit was made physically as small as possible to reduce chances of extraneous noise pickup, and housed in a shielded metal box which also housed the cells. Connections were made with coaxial cables using heavy gauge BNC connectors. A large number of tests were done on the circuit to judge its performance using synthetic signals from a solid state signal generator, utilizing a range of amplitudes and frequencies. Figure 2.8 shows an input V_s output oscilloscopic trace generated by the amplifier. The input signal was a sine wave with amplitude of 130 mV and a frequency of 10 Mhz. The linear nature of the trace shows the excellent frequency response and linearity of the device. The trace also shows that the amplifier reaches its saturation state, at an output of around 8 Volts. However since a CMOS data acquisition would be used, the output signal from the amplifier would not be allowed to go above 5 Volts.

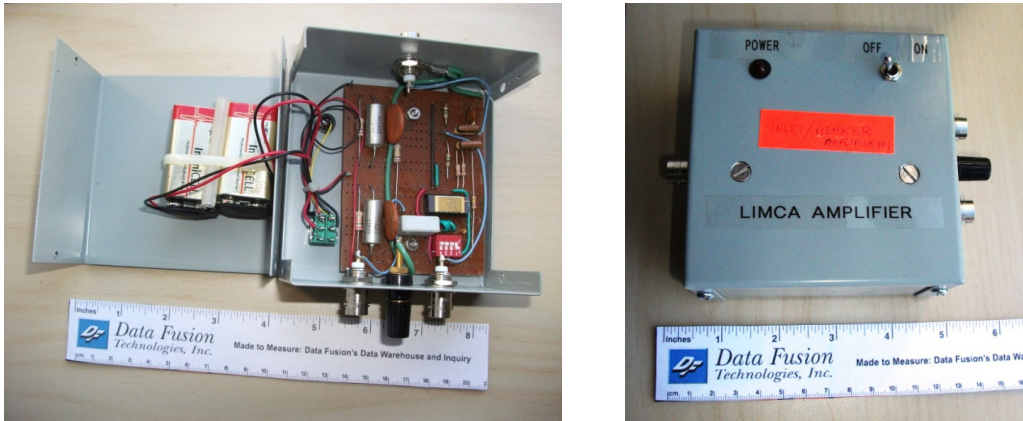


Figure 2.9 – Final assembled APS amplifier (ref 83)

The amplified signal was fed to an analogue input channel of an InstruNET i-NET100 data acquisition board and DASyLab v5.6 software. The DASyLab worksheet was configured to 2 kHz in analyzing voltage readings from the analogue input channel which was set at a sampling frequency of 20 kHz. This was kept sufficiently high, as the individual peaks comprising of the APS signal are of extremely short duration and only a high sampling rate would provide the necessary resolution to capture all the transient artifacts of the signal. Figure 2.9 shows the final, assembled APS amplifier.

2.6.0 Adopted noise reduction/signal conditioning techniques

The relatively high resistance path through the fluid filament in the probe circuit has a deleterious effect on the signal to noise ratio of the APS signal as mentioned before, and further measures were needed to reduce the amount of noise in the circuit. As mentioned, the use of high quality shielded co-axial cables were the first line of defense against the pickup of extraneous noise from the environment. However, even with adequate shielding, the final signal still contained noise components that needed to be removed. Noise picked up by the setup can be of two broad types

- *Low frequency* – These constitute low frequency components added to the final signal. The primary source for this is the 60 Hz mains component picked up by external wires, also commonly referred to as the “Mains Hum”. A narrow band stop filter across 60 Hz was incorporated to remove as much of the 60 Hz component as possible.
- *High frequency* – High frequency external noise has numerous sources, like radio signals, operating machinery, electrical sparks to name a few, but all present in the immediate environment. A low pass filter at 5 KHz was used to block the higher frequency components. The exact frequency of operation of the filter was however not calculated exactly. A spectral curve of the raw APS signal showing relatively high noise levels above 5 KHz was used as a rule of thumb to obtain the filter frequency.

Even with the above filters in place, the filtered signal still showed noise components, and a threshold noise removal scheme was applied. Lab tests were performed to ascertain the relative amplitude of the left-over noise in the signal, which showed maximum amplitude of around 0.15 volts. All perturbations within the signal less than 0.15 volts were forced to zero. The use of DASyLab showed another advantage in itself, by being able to incorporate these noise reduction techniques as software based filters thereby eliminating the need for external equipment. Figure 2.8a shows the original unfiltered raw signal obtained after amplification. Figure 10b shows the improved signal to noise ratio after the signal is filtered for both high and low frequency noise. Figure 10c shows the final signal after the threshold noise removal has been applied, and shows the final signal form before particle size measurement is carried out.

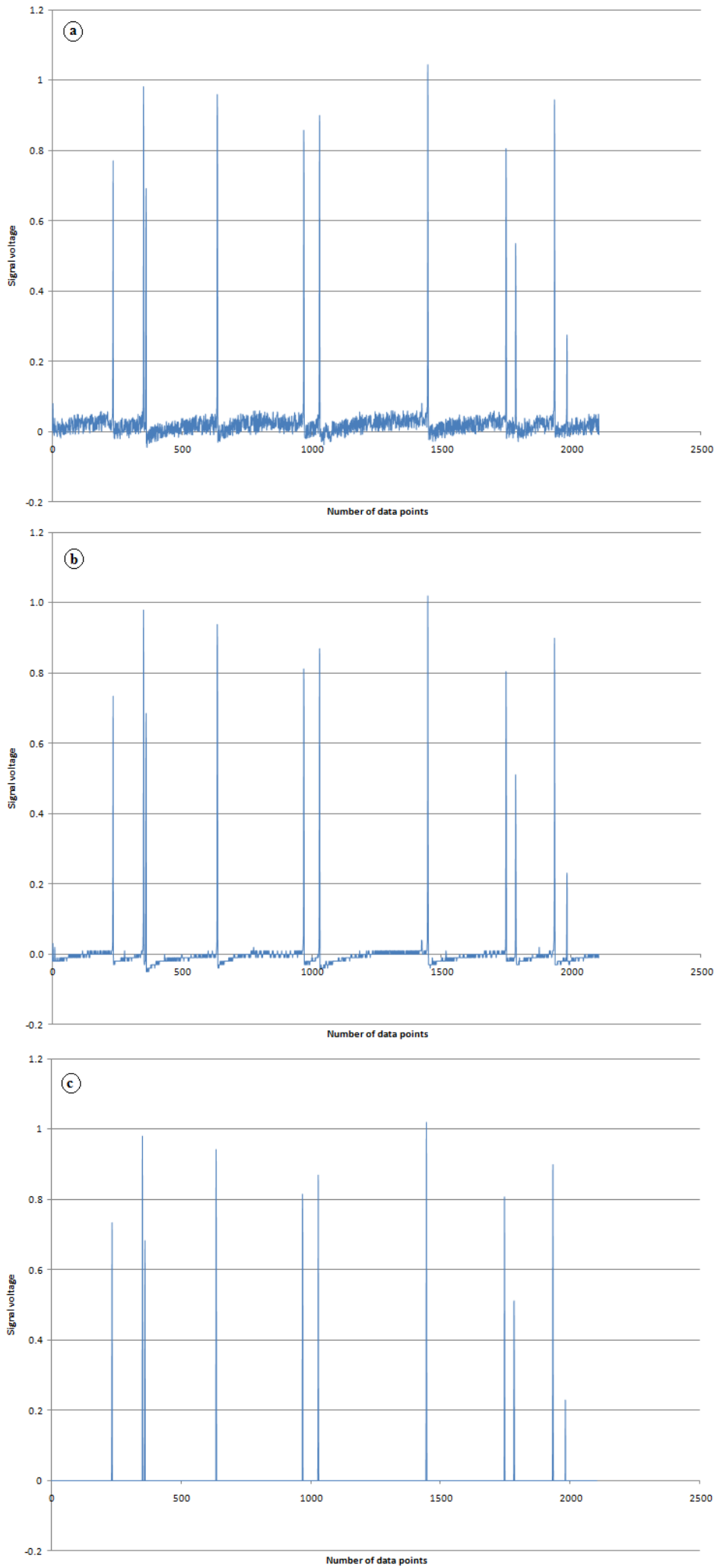
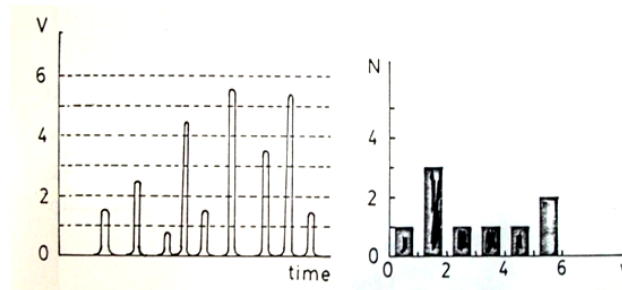


Figure 2.10 – (a) Unfiltered raw signal from amplifier. (b) Signal obtained after high and low frequency noise filtering. (c) Signal obtained after application of threshold noise removal.

2.7.0 Algorithm used for study of particle size

Raw data obtained as the output signal from the APS probe upon successive amplification would merely consist of a number of transient voltage pulses corresponding to each particle being counted. Since the particle generally takes less than a milli-second to pass through the orifice, these voltage pulses are very narrow, and proper analysis is essential to obtain useful information from the electronic signals

While the APS signal gives us information about each particle, and in theory a data analyzer can be made that lists the size of each particle being detected, it would lead to a huge amount of information, which may not be very convenient for industrial or research purposes considering the particle count can be in the tens of thousands. So the signal processing algorithms developed, classified all the particles that were detected into a number of appropriately chosen bins. Counters were used to store the number of particles falling into each size range, or bin, and the resulting values of each counter were displayed as a histogram. This sort of data was much more convenient for analysis by the user. Figure 2.11 shows the process more clearly.



Bin number	Bin Range	Number of peaks lying in that voltage range	Tally Marks
1	0 – 1 volts	1	/
2	1 – 2 volts	3	///
3	2 – 3 volts	1	/
4	3 – 4 volts	1	/
5	4 – 5 volts	1	/
6	5 – 6 volts	2	//

Figure 2.11 - Pulse height analyzer

The choice of using the DASyLab data acquisition software was an advantage in itself due to its superior user interface, and its menu driven structure. Once an algorithm was developed, it was entered into the DASyLab workplane (ref 84). Figure 2.12 shows the exact algorithm. The use of this particular software was also useful in incorporating software based filters to remove some extraneous noise from the signal, considering the fact that the device was meant to operate in electrically noisy environments. A narrow band stop filter across 60 Hz would remove any mains components, while a low pass filter was used to block any high frequency noise that may be picked up.

The total CMOS voltage range from 0 to 5 volts are divided into “n” number of Bins, and counter variables called Counter(1), Counter(2) Counter(n) are assigned to each of these bins. The size of the particle is measured by measuring the height of the peaks in the signal. Whenever the signal peak rises above the lower threshold value of a bin, its corresponding counter is incremented by 1, thereby registering a particle detected which falls in the size range of the bin. However this algorithm while being fast and simple, has a drawback as larger sized particles would pass through the lower threshold values of a number of preceding bins, and would register itself in these bins as well. For example, if a particle falls into the size range of bin number 3, it would also result in it being registered in Bin numbers 1 and 2 as its signal peak would cross the lower threshold limits of these bins as well. The solution was to cumulatively subtract each counter value from its preceding counter. The following table shows the several bins into which the particles were classified into depending on their size

25-30	30-35	35-40	40-50	50-60	60-70	70-80	80-100	100-120	120-140	>140
-------	-------	-------	-------	-------	-------	-------	--------	---------	---------	------

Table 2.1 – Size ranges in microns into which the particles were classified.

It is emphasized that, with a data sampling rate of 2kHz, the time between two successive data points is a mere 0.5 millisecond. This is also the time limit

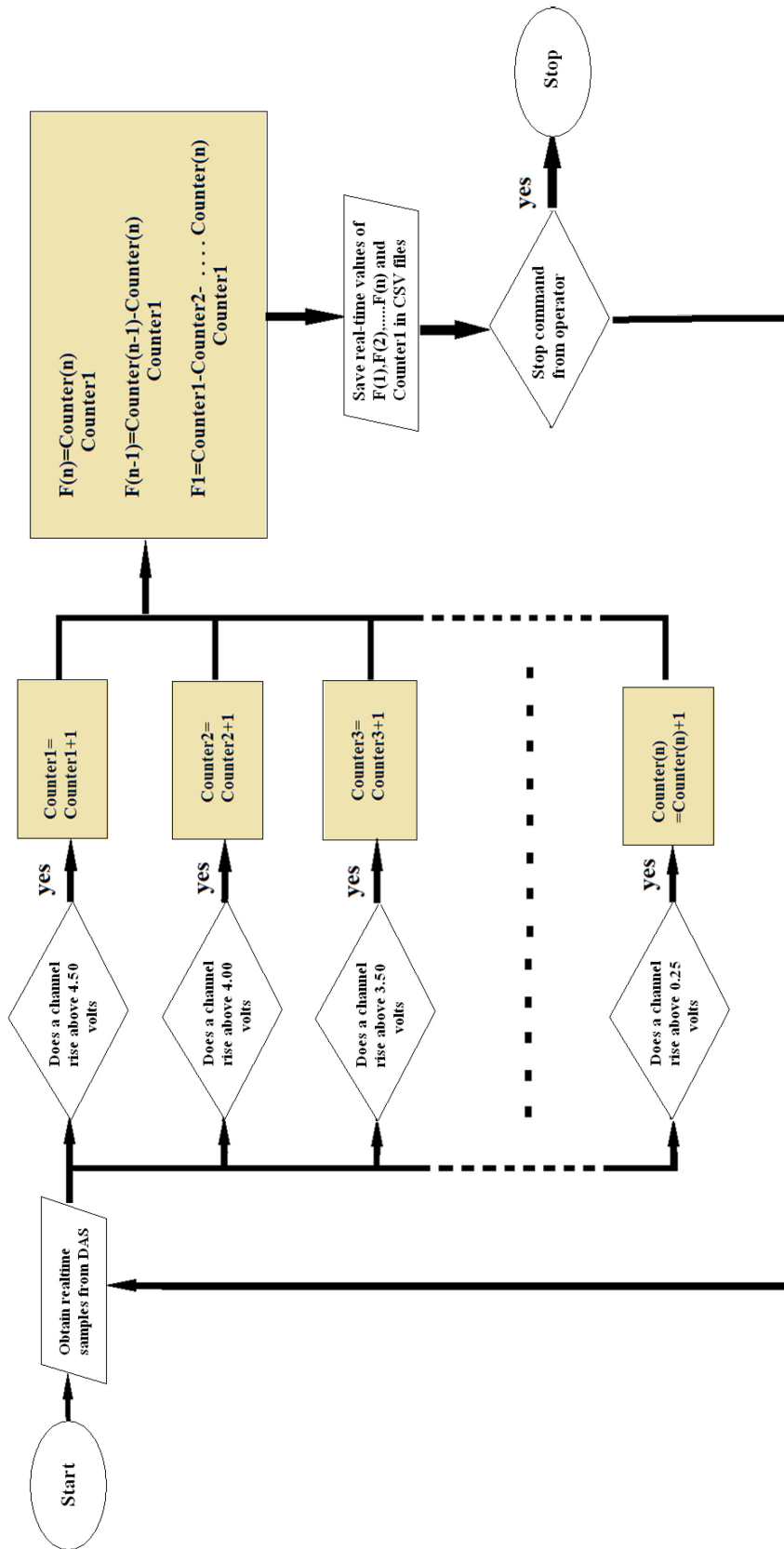


Figure 2.12 – Algorithm used in APS III

within which the computer processor must perform one instance of the algorithm. This puts a severe limitation on the choice of the algorithm used. Signal analysis of the APS would basically consist of location of maxima along the time varying signal. However tests with such an algorithm showed that even with modest computing resources, it took more than 0.5 milliseconds to perform one instance of the algorithm. Also mere identification of a maxima may not necessarily constitute detection of a particle, as local signal maxima can be produced by transient noise peaks as well. The new algorithm adopted here worked flawlessly with a 2.10 Ghz Core II Duo Intel processor running on 4 GB of RAM. The final version of the DASYLab worksheet classifies particles into 11 different size ranges or bins. Figure 2.13 shows a screenshot of the final worksheet. The size fractions of particles in each bin (obtained by dividing the value of its corresponding counter with the total particle count) are displayed as a histogram, and the total particle count is also displayed.

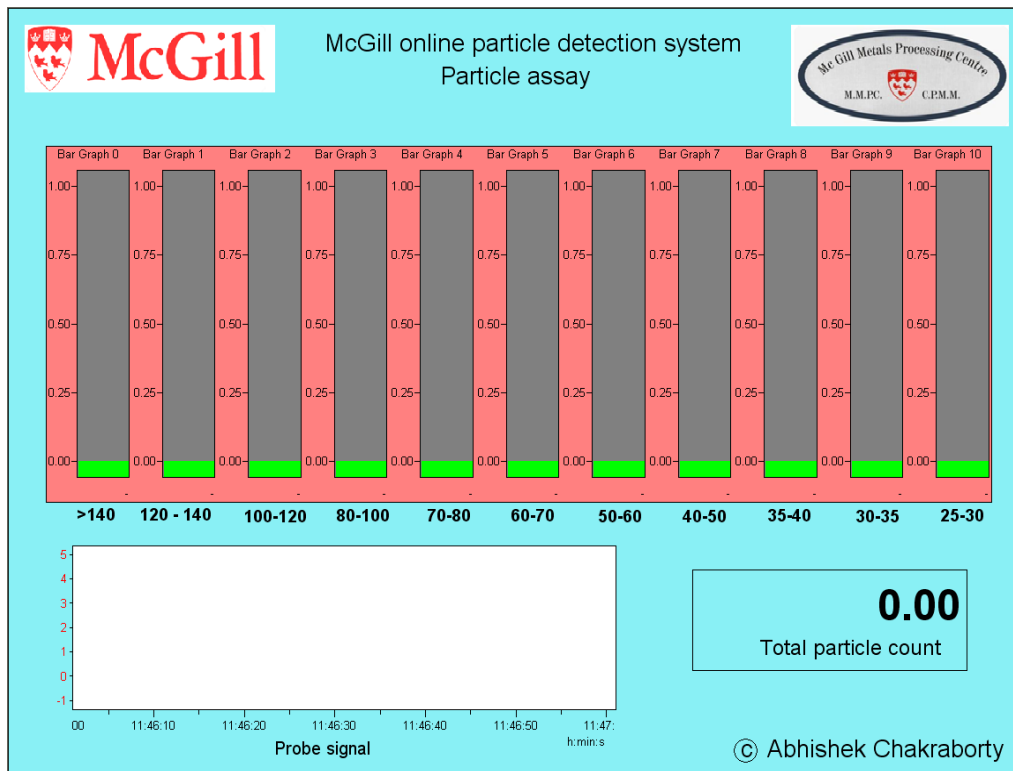


Figure 2.13 – Screenshot of the user input interface for APS III

It should be noted that while the algorithm itself should classify particles on the basis of its diameter, it's the signal voltages that it is measuring. While mathematical considerations described by equation 1 gives a relation between voltage peaks and particle size, it is worthwhile to perform an experimental calibration of the device, as well

2.8.0 Calibration of APS III

Calibration of the device was performed using 4 different particle sizes of tight size ranges or tolerances. Separate experiments were performed using suspensions of standard silica particle of sizes 20, 40, 90, 120 and 140 microns in normal tap water. Figure 2.14 shows the plots of voltage Vs number of peaks detected. Assuming a Gaussian distribution of the particle size across the reported size of the standard particles, Gaussian fits were calculated for the four experiments using the CFTOOL (ref 85) option in MATLAB. The voltage corresponding to the point of maxima on the Gaussian curves would be taken as corresponding voltages for the chosen particle sizes. The uncertainty in voltage measurement was taken as the error measured at half heights of the Gaussian curves. Figure 2.15 (see appendix 1) shows the final calibration curve obtained by plotting the 4 data points relating a particle size and its signal peak voltage.

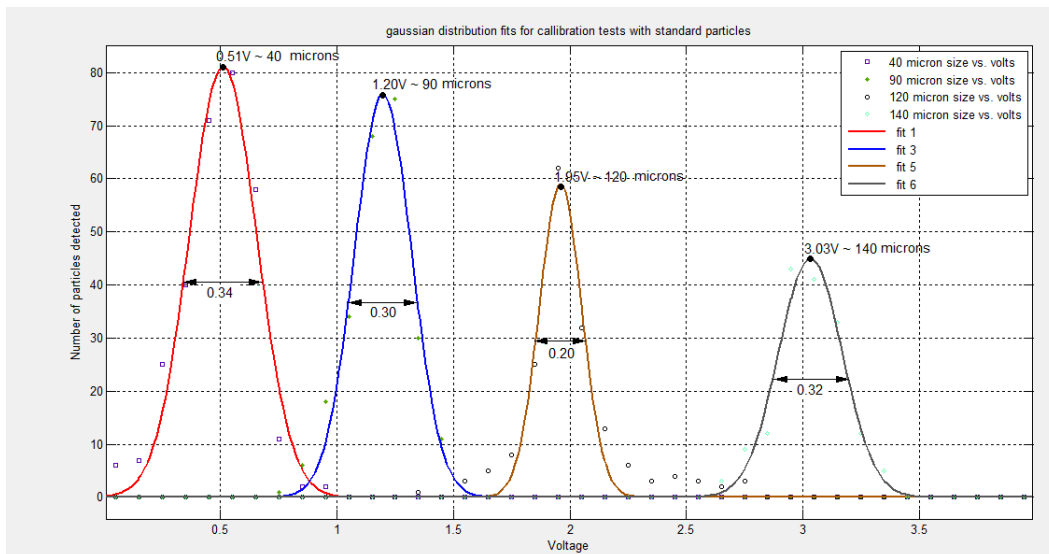


Figure 2.14 – Gaussian distribution peaks obtained with standard particle sizes

The error bars in the x axis shows the deviation in particle size as reported by the manufacturer of the standard particles. (ref 86). A similar error analysis with the 20 micron particles could not be done as the small voltage peaks produced have an error range partially coincident with the threshold noise region of 0 to 0.15 volts. However the data point generated with the 20 micron particles was used in generating the final calibration curve. Using similar curve fitting techniques, an equation of the type described in Equation 2.2 was obtained in MATLAB, which is as follows. (bold dotted line in Figure 2.15)

$$\Delta V = 1.57 * 10^{-6} d^3$$

Comparing with Equation 2.3

$$\Delta V_{amplified} = \alpha k d^3 \quad [2.3]$$

$\alpha=100$ [chosen when amplifier was designed]

$$k_{\text{experimental}}=1.57*10^{-8}$$

While the above value of k has been derived empirically from experimental data, the value of k can also be derived from Equation 2 utilizing measured physical parameters.

$$k = \frac{4\rho_e I}{\pi D^4}$$

$$\rho_e = 5\mu\text{S/cm or } 0.2*10^6 \Omega\text{cm}$$

$$I=0.3 \mu\text{A or } 0.3*10^{-6}\text{A}$$

$$D=500 \mu \text{ or } 500*10^{-4}\text{cm}$$

$$\text{Therefore, } k = \frac{4*0.3*10^{-6}*0.2*10^6}{\pi*(500*10^{-4})^4}*(10^{-4})^3$$

$$\text{Or } k_{\text{calculated}}=1.22*10^{-8}$$

Thus, it can be seen that there is a fair degree of agreement between the calculated and the experimentally obtained values of k. However, as is apparent in the figure, there is a deviation between the ideal fit and the experimentally obtained data points and hence consequently the two values of k. This can be attributed to the non-ideality of the amplifier circuit and excitation source used with the detector. While Equation 2.2 considers a constant current source, the excitation method used in this study was not. A second polynomial fit (thin solid line) of type $f(x)=ax^3+bx^2+cx+d$ shows a much better adherence to the data points. So the final corrected working equation used for APS III is defined to be

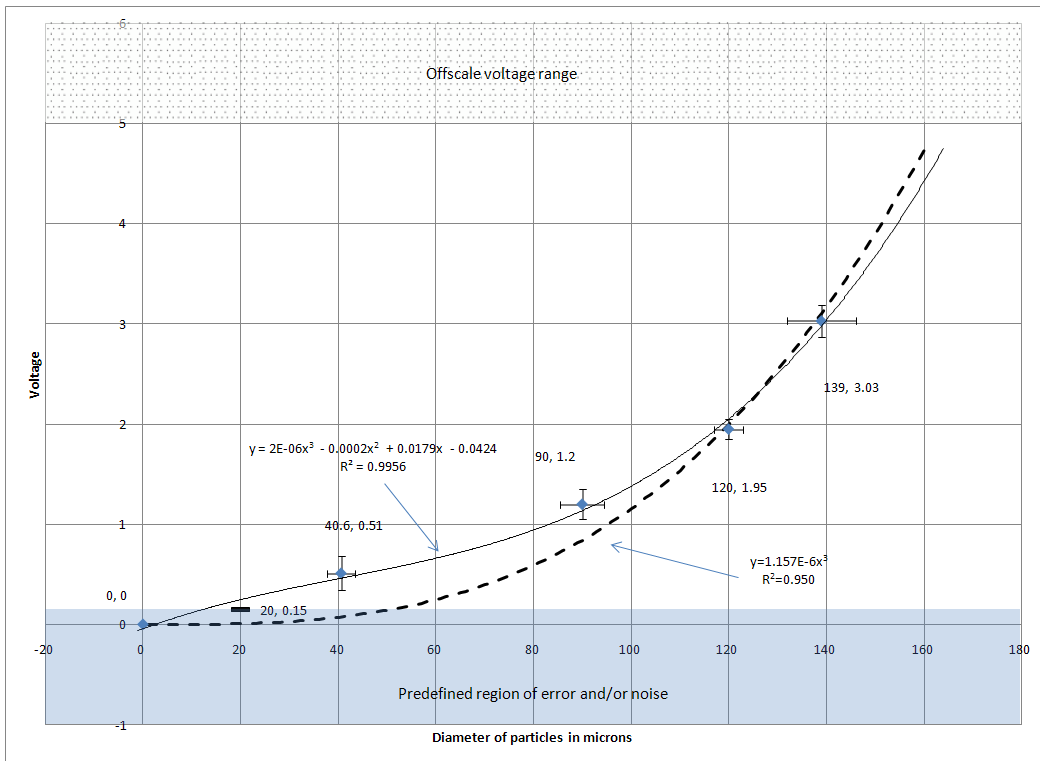


Figure 2.15 – Final calibration curve for APS III

$$\Delta V = 2 \cdot 10^{-6} d^3 - 0.0002 d^2 + 0.0179 d - 0.0424 \quad [2.4]$$

The last two terms in the above equation can be termed as correction factors arising out of non-ideality of the system. It is to be noted that the equation 2.4 was computed to also pass through the data point generated by a particle size of 20 microns, and the origin. While detailed analysis of this non-ideal behaviour was

not undertaken, the obtained calibration curve was markedly stable and easily reproducible, and propitiously fortunate for this research. The calibration curve, while not adhering to ideal equation, served its purpose of accurately predicting a particle of a given size.

Since the instrument was initially intended to operate in the water modeling facility at McGill University, the ambient noise level in the signal was measured in the environment of interest. It was observed that that maximum value of the noise peaks was around 0.15 volts, and this was defined as the lower threshold of measurable particle size, around 15-20 microns. The upper threshold of measurable size range was limited by the fact that the CMOS based data acquisition system saturates at above 5 volts, which corresponds to a particle size of 170 microns.

2.8.1 Coincidence limit of APS III

While the calibration procedure established the operating limit of the device, as a particle range of 25 to 170 microns, another limiting factor for its performance is the maximum particle density in the fluid it can measure. The electric sensing zone principle assumes that there should be single particle in the volume of the electric sensing zone at any instant of time, or else peaks generated by two particles passing through the orifice at once, would give rise to erroneous results. The upper limiting particle concentration can be obtained by assuming a uniform particle density, with one particle per volume of the orifice.

$$\text{Orifice volume} = \pi r^2 h = 3.14 * (250 * 10^{-6})^2 * 1.2 * 10^{-3} \text{ cu mt} = 2.35 * 10^{-10} \text{ cu mt.}$$

$$\text{So the limiting particle density} = (2.35 * 10^{-10})^{-1} \text{ per cu mt.} = 4.24 * 10^9$$

Considering a factor of safety of 10, the maximum useful particle density may be reported as

$4.24 * 10^8$ per cu mt or more conveniently 424 (let's say approximately 400) particles per cc.

2.9.0 Conclusions

As a result of the present study and innovation, a new and improved Aqueous Particle Detector has been developed from first principles, which has the potential to outperform its previous versions. The capability of the new device to perform online tests under totally submerged conditions makes it an invaluable research tool in carrying out inclusion behavior studies in water modeling experiments. The versatility of the device also lies in the fact that there is no need to collect samples during the actual tests, the detector probes may be placed at any convenient location within the experimental vessel, and data collected in real-time. As part of a continuing endeavor to utilize this research tool, the full scale 4 strand water model tundish at McGill Metal Processing Centre is being fitted with an even more advanced version of APS III, in order to track inclusion behavior with 5 separate detector probes placed at strategic locations within the vessel.

Use of APS III in water modeling experiments

3.1.0 Introduction

As mentioned before, the real purpose behind the development of the APS III was to use it to carry out physical modeling experiments at the McGill Metals Processing Centre. The first application of APS III was to study inclusion behavior in tundishes fitted with a variety of flow modifiers. A full scale water model of a generic 12 tonne delta shaped tundish was fitted with APS III detectors at several locations to measure the amount of inclusions per volume of water.



Figure 3.1 – A water model of a full scale 12 tonne delta shaped water model tundish at McGill Metals Processing Centre

For this it is essential to discuss some details about the tundish system itself, i.e. the use and functioning of a tundish in steel processing. A tundish is a buffer vessel set between the steelmaking ladle and the casting moulds in a continuous process. While modern plants in greater numbers are implementing continuous casting technologies, steel making remains a batch process in which, the tundish acts to distribute and maintain a uniform flow of liquid steel into the

continuous casting moulds. The residence time of the molten steel within tundishes of moderate size can be as high as 30 minutes, and this time is enough to realize a number of metallurgical functions such as homogenization of flow, and removal of some inclusions by flotation. The performance of the tundish can be judged by flow fields of the molten steel, and thus depends heavily on the size, and design of the tundish in question. Often flow modifiers are retrofitted into the tundish to provide improved performance. The purpose of the present study was to judge the performance of the tundish when fitted with several different flow modifiers.

3.1.1 Continuous casting process

While the older ingot casting process consisted of transferring the molten steel from the ladle to cast-iron moulds, in modern continuous casting techniques, the molten steel in the ladle is poured into the tundish where it continuously feeds a set of open bottom copper moulds, where it partially solidifies and leaves the mould through the bottom side. Thus, only long products of relatively simple and uniform cross-section are usually produced by continuous casting. Figure 1 provides a comparison between the conventional ingot casting process and continuous casting. Continuous casting provides a number of important advantages over the older batch process. (ref 87,88)

- The reduced number of separate operations results in increased efficiency and reduced energy consumption
- Increased casting speed (1.5-2.8 m/min)
- Improved inclusion float-out owing to the relatively high residence time and low fluid velocities within the tundish.

The earliest mention of a continuous casting process was made in the late nineteenth century by R.M. Daelen (ref 89). The process consisted of water cooled copper moulds open at both ends, and liquid steel was poured through the bottom. However there was a problem of the liquid metal sticking to the copper

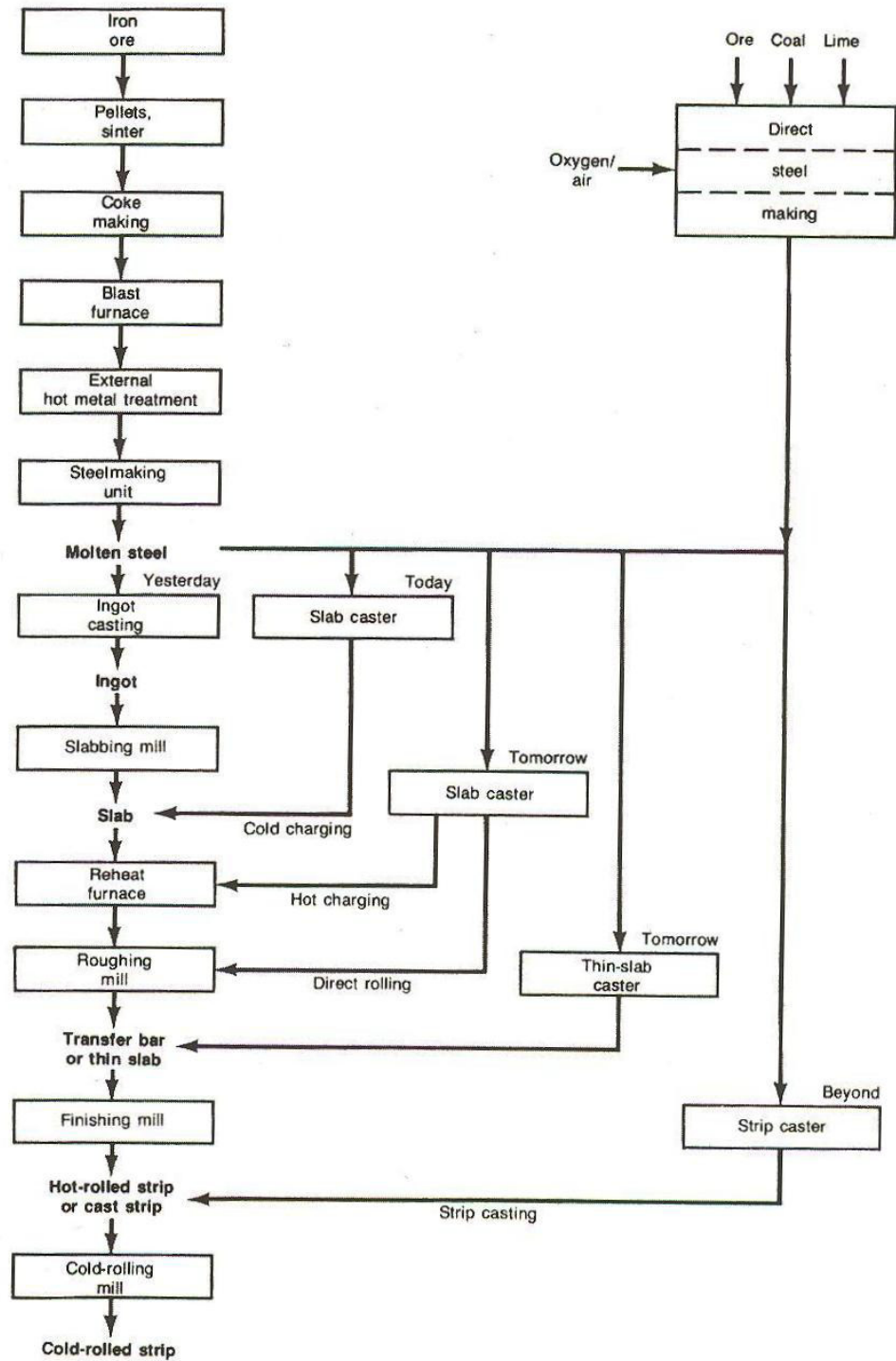


Figure 3.2 – The past, present, and the future of casting processes (ref 91)

mould. Siegfried Junghans (ref 90) developed a mould oscillation system to correct this problem. In modern casting operations, a batch type draining ladle, a constant

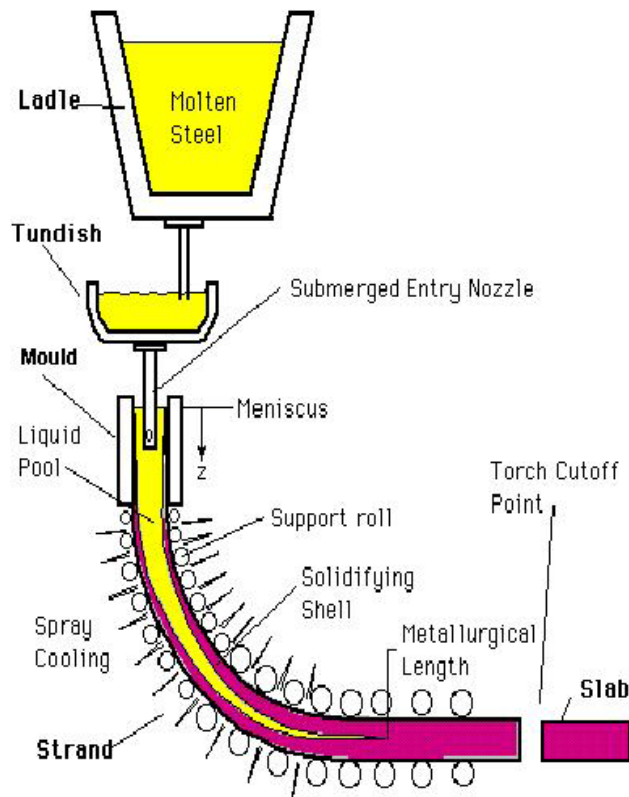


Figure 3.3 – Schematic of a continuous slab casting process (ref 92)

head draining tundish, and a mould and mould oscillator, comprise a continuous casting unit. Figure 3.2 describes a schematic of the setup.

As explained in the initial review, inclusions in the final steel product can detrimental to the final cast product. Oxidation of the molten steel in contact with air constitutes one such source. The hot liquid steel is extremely vulnerable when it is transferred from the ladle to the tundish. To prevent contact with air a ladle shroud is used to protect the metal, and this tube is enveloped with a protective envelop of argon. The surface of the steel within the tundish is also protected with a layer of slag on its surface. Steel from the tundish is poured into the moulds by submerged entry nozzles (SENS). Large tundishes can have up to 8 submerged entry nozzles depending on the number of strands being cast.

3.1.2 Behavior of inclusions

No matter how much care is taken to protect the molten metal from oxidation, the liquid metal within the tundish still contains some inclusions. Most of these inclusions are oxide particles in nature, and lighter than the molten steel. According to Stokes law, the rising velocity of a particle in a non-agitated fluid is given by

$$U_s = \frac{(\rho_{Fe} - \rho_{inclusion})gd^2}{18\mu} \quad [3.1] \quad \text{Reynolds number (Re)} < 2$$

Where μ = viscosity of steel

d = diameter of inclusion

U_s = Stokes Rising Velocity

Since the fraction of inclusions of sizes greater than 150 μm is almost negligible and the maximum particle size governed by Stokes law is $\sim 190 \mu\text{m}$ in diameter, it is reasonable to assume that inclusions in molten steel typically follow Stokes law. Thus, for an inclusion of a particular size, it takes a finite amount of time to float up to the surface and get trapped in the slag layer. If the residence time of the steel within the vessel is larger than the time taken for the inclusion to reach the surface, then we assume 'inclusion float-out'. However, this is only considering ideal plug-flow conditions. In the real system, agitation of the liquid metal can hinder or helps this float-out depending on the flow characteristics. The main source of this agitation is from the jet of liquid metal entering the bath in the tundish. Thus flow modifiers are constantly used in tundish operations to dissipate the energy of the falling jet of liquid steel entering the tundish, and curtail its detrimental stirring effects.

3.1.3 Physical modeling of tundish operations

The objective of physical modeling is to study the real system with a prototype or model, where the dangerous high temperature liquid metal is replaced with a safer liquid, namely water. The main purpose of modeling a

tundish system is to study the flow fields generated within the vessel. To obtain a reasonably realistic representation, the model and prototype must satisfy geometric as well as dynamic similarity.

To obtain geometrical similarity, corresponding linear dimensions between prototype and model must bear a constant scalar ratio. This ratio can be defined as the geometric scale factor λ .

$$\lambda = \frac{L_m}{L_p} \quad [3.2]$$

Where L_p =linear dimension in the prototype

L_m =linear dimension in the model

The dynamic similarity criteria can be derived by non-dimensionalizing the Navier-Stokes equations

$$\frac{D\vec{v}^*}{Dt^*} = -\Delta^* P^* + \frac{1}{Re} \Delta^{*2} \vec{v}^* + \frac{1}{Fr} \vec{g} \quad [3.3]$$

$$Re = \frac{LU}{\nu} \quad [3.4]$$

$$Fr = \frac{U^2}{gL} \quad [3.5]$$

Where ν =fluid kinematic viscosity

U =characteristic velocity

L =characteristic length

g =acceleration due to gravity

The Reynolds number (Re) and the Froude number (Fr) are defined as the ratio of inertial forces to viscous forces and to gravitational forces respectively. Hence, a geometrically identical prototype and its model would have similar hydrodynamic characteristics as long as the Reynolds and Froude numbers are

same. However it can be shown that a physical model can only match both criteria for dynamic similarity provided the geometric scale down factor, λ , is unity.

3.2.0 Details of physical model used

The model that was utilized for the present study was a full scale water model of a generic 12 tonne delta shaped 4 strand tundish. The inclusion float-out performance of the tundish was studied with a variety of flow modifiers, and the residual ratio of inclusions was calculated. Figure 3.4 shows how the four strand positions are numbered.

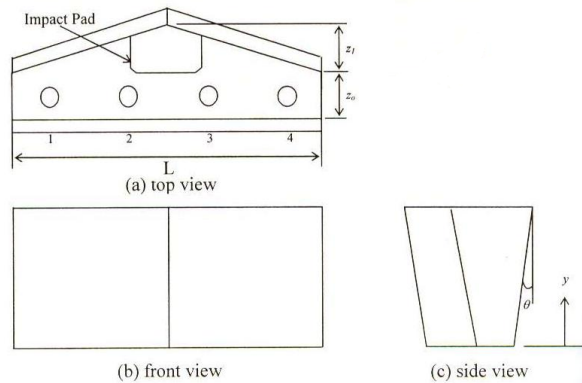


Figure 3.4 – The shape of the four strand delta-shaped continuous casting tundish

Since the tundish is bilaterally symmetrical, APS detectors were only connected to strand positions 3 and 4, assuming we would obtain a symmetrical distribution of inclusions on strands 1 and 2, as well. Figure 3.5a shows one of the strands fitted with an APS probe. As explained in previous sections, APS probes need a constant source of low pressure within the tube to aspirate the test solution through the orifice. Due to absence of a suitable vacuum line in the laboratory, an improvised siphon tube (Figure 3.5b) was connected to each aspiration tube in the detectors. Meter long rigid Plexiglas tubes were filled with water and made the descending leg of the siphon such that their lower end always remained below the water level in the tundish, so that water continuously flowed down the tube. A tap connected to the end of the siphon tube was used to adjust the aspiration rates through the detectors. A 3 m high Plexiglas rectangular tank placed above the

tundish helps to maintain a constant pressure head at the shroud. Since the original APS working equation is dependent on fluid properties such as temperature, electrical conductivity etc. of water, appropriate sensors were installed (Figure 3.6) to make sure the physical properties of the supply water was similar to those used during the calibration. The model, being full scale with respect to the prototype, matched both the Reynolds number and Froude number of the plant equipment. The shroud flow rate was kept at 170 litres per minute, and flow through each strand was 42.5 litres per minute.

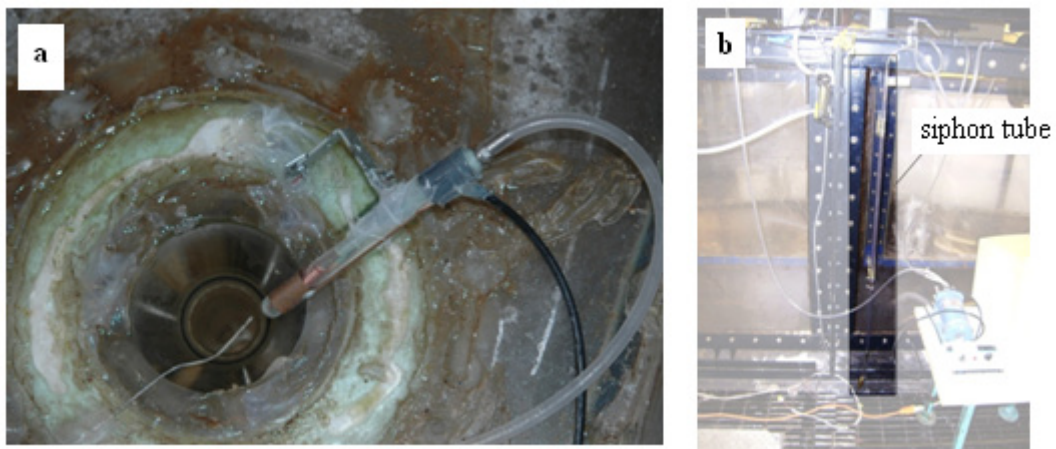


Figure 3.5 – a) an APS sensor attached to a strand b) highlighted area showing APS aspiration tube

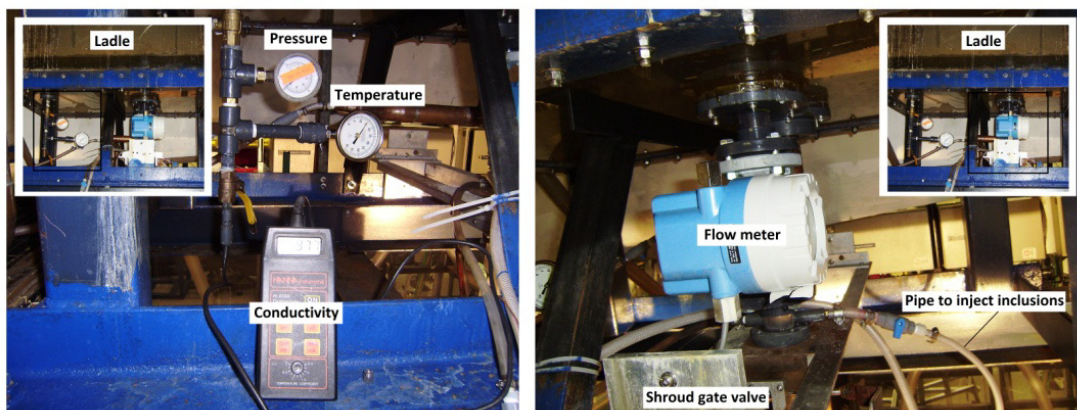


Figure 3.6 – Conductivity, temperature and pressure sensors installed below the ladle to record the physical characteristics of the water

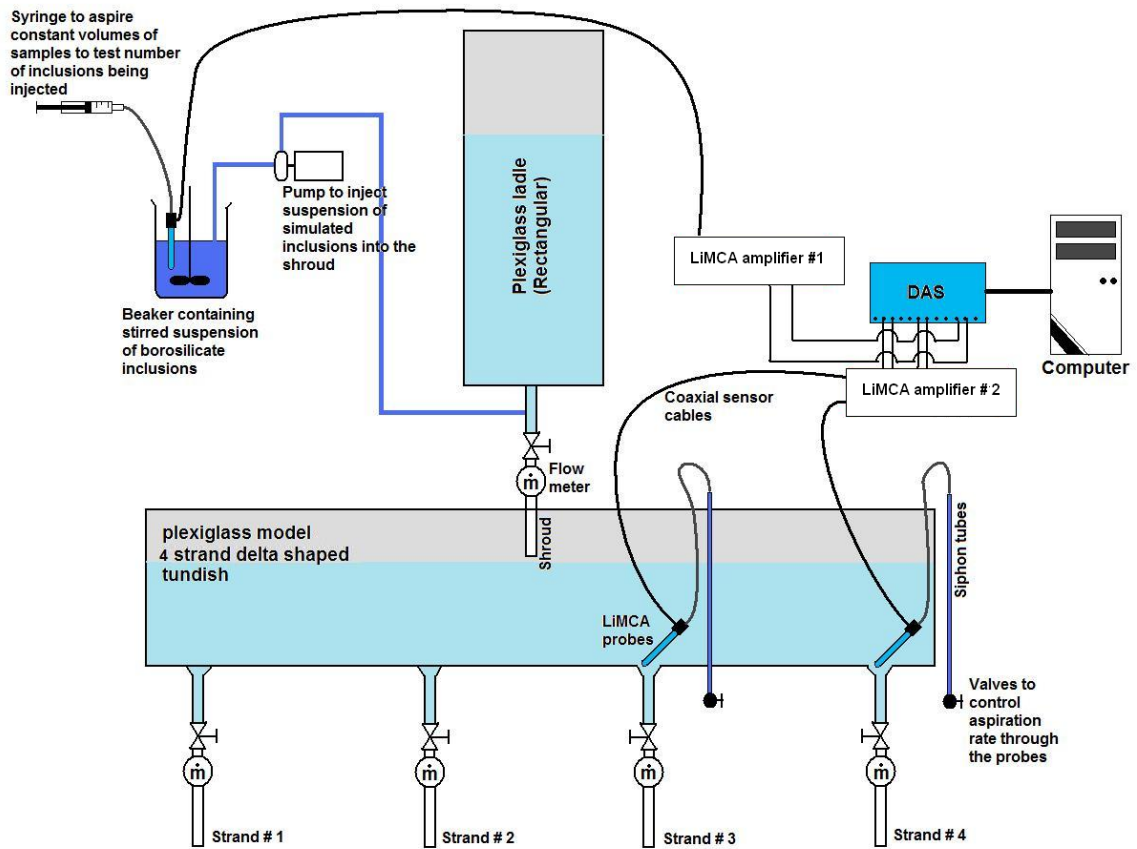


Figure 3.7 – Schematic diagram of the experimental setup

3.3.0 Experimental procedures

Due to its easy availability, tap water was used as the working fluid. Small, hollow, borosilicate glass microspheres, of a fixed size range were utilized to simulate the inclusions (refer to appendix 2 for size distribution and density). The tundish was first operated to reach steady state, where the height of liquid in the vessel remains constant. The borosilicate glass particles of known size distribution were pumped continuously into the shroud as a slurry of known concentration, at a fixed rate. At the same time, the APS probes were activated and the amount and size distribution of the inclusions reaching the inner and outer strand was measured as a function of time.



Figure 3.8 – Microscopic view of the hollow glass microspheres used to simulate inclusions

The amount of inclusion float-out was quantified with a term called **Residual Ratio of Inclusions (RRI)**. RRI in our experiments is defined for a particular strand as

$$RRI = 4 * \frac{\text{number of inclusions going out through the strand}}{\text{Total number of inclusions added through the shroud}} * 100 \quad [3.6]$$

It should be noted here that the prefactor of 4 occurs because one source of inclusions namely the shroud, leads to 4 sinks or strands. The higher the value of RRI, the less the number of inclusions removed and the worse is the performance of the tundish as an inclusion remover. Now if we consider a hypothetical case, when none of the inclusions float out, but are roughly homogenously mixed in the tundish, then theoretically the RRI should be 100. However, in our system if we divide the output number of inclusions through one particular strand with that added to the shroud, the RRI value would be much less than 100, since the inclusions are distributed and pass out through the 4 strands. Thus, the prefactor of 4, just acts to normalize the RRI values. Now as mentioned, while one RRI can be associated with one particular strand, it will not be a constant value as RRI also depends on the particle size being measured. Integrated RRI values are calculated

considering the total number of particles detected irrespective of their size, while RRI can also be calculated considering a particular size range.

While APS probes connected at the exit strands measured the number and size distribution of inclusions exiting, the number of inclusions being added could not be obtained directly. Common practice would involve putting an APS probe at the shroud; however this poses a set of problems:

- The high fluid flow velocities within the shroud would damage the fragile APS probes
- The internal diameter of the shroud pipe being in the range of 4 to 5 cm, putting a 1.2 cm bore tube within it would change the hydrodynamic performance of the shroud
- High turbulence within the shroud results in the entrainment of small gas bubbles which would result in added noise and erroneous APS signals.
- The high concentration of particles within the shroud would mean that the detector be operated very close to the coincidence limit of the instrument.

For the above reasons, the amount of inclusions being added was calculated indirectly. An off-line particle assay study was made to ascertain the particle size distribution and concentration in the slurry being added to the shroud. For this test, however, the slurry had to be diluted with measured quantities of water several hundred times for the test solution to be within the co-incidence limit of the device. The slurry was made with a known weight of borosilicate glass microspheres in a known volume of water. Tests gave particle distribution and total particle density per volume. This was used to calculate the number of particles per gram of the dry powder.

$$= \frac{\textit{number of particles detected per ml of the slurry}}{\textit{amount of particles in grams added per ml of water}}$$

Let $f(s)$ = particle size fraction as a function of 's', the particle size range.
(Appendix 2)

This is referred to as “particle assay” in Appendix 3

Let the concentration of particles in the suspension = x g/ml

Rate of addition of particle slurry = 300 ml/min

Shroud flow rate = 170 l/min

Also from our results, we know that 1g of particles contains 2.2×10^6 particles.

So from the above data, the number of particles of size ‘s’ going into the shroud

$$x \cdot 2.2 \times 10^6 \cdot 300 \cdot f(s) = A(s) \quad [3.7]$$

At the outlet, the two APS probes were connected with known aspiration rates, which was used to measure the total number of particles detected as a function of time, as well as their size fraction. Now during tests, the APS samples a small fraction of the water exiting an outlet, since the total flow rate is much higher than the sampling rate through the detector, Hence

$$\frac{\text{Rate of inclusion count at the detector}}{\text{Total number of inclusions exiting a strand per time}} = \frac{\text{Flowrate through the detector}}{\text{Total flow rate at the strand}}$$

Flow rate through each strand = 42.5 l/min

Aspiration rate through the APS probe = y ml/min

Let N = number of particles detected by a probe per min at steady state.

This is referred as “rate per minute (sampled) in Appendix 3

So total number of particles exiting the strand = $(N \cdot 42.5 \cdot 1000) / y$

So from the above data, the number of particles of size ‘s’ going out of a tundish strand (assuming no float-out)

$$N \cdot 42.5 / y \cdot 1000 \cdot f(s) = B(s) \quad [3.8]$$

$$\text{Therefore RRI} = [4 * B(s) / A(s)] \quad [3.9]$$

3.4.0 Experimental results

RRI studies were done with the new MMPC On-line aqueous particle detection system. Tests were conducted first with the bare tundish and subsequently with a standard set of flow modifiers commonly being used by the industry. This was done with the view to obtain a better understanding of the improved performance offered by the flow modifier as compared to the bare tundish.

Since the new system had online capabilities, data was recorded from the very start of the experiment. Each experiment was continued for 45 minutes, a way to make sure that we reach steady state. The following Figure 3.9 shows a plot of the total number of inclusions detected as a function of time, at the inner strand of the bare tundish. As is apparent, the slope slowly reaches a constant value, which means that we reach a constant number of inclusions going into the strand in unit time, which is the condition of steady state.

While calculating RRIs, data from only the last 15 minutes were used, to make sure that we have steady state conditions. The nature of the curve for the other strand, both with, and without, the flow modifier, was essentially similar, except the final slope. It should be made clear; a higher slope means a poorer inclusion float out, as we have more inclusions going into a particular strand per unit time. In-essence the new APS system can thus judge the performance of flow modifiers, by calculating the steady state slope of the type of plot shown Figure 3.9. It is also interesting to note that under steady state conditions, the slopes of the two curves are different. The inner strand shows a much higher slope than the outer strand. This can be explained by the fact that the residence time in the tundish for the liquid exiting the inner strand is much lower than at the outer strand simply because of its greater distance from the shroud. The increased

residence time provides more time for the inclusions to reach the surface, and hence we have a larger number of inclusions reaching the surface. Figure 3.9 was obtained with a bare tundish under steady state operating conditions. At this point, the curve shown does not consider particle characterization with respect to size; as only the total number of particles, irrespective of size, being detected at the strands, is plotted along the y axis.

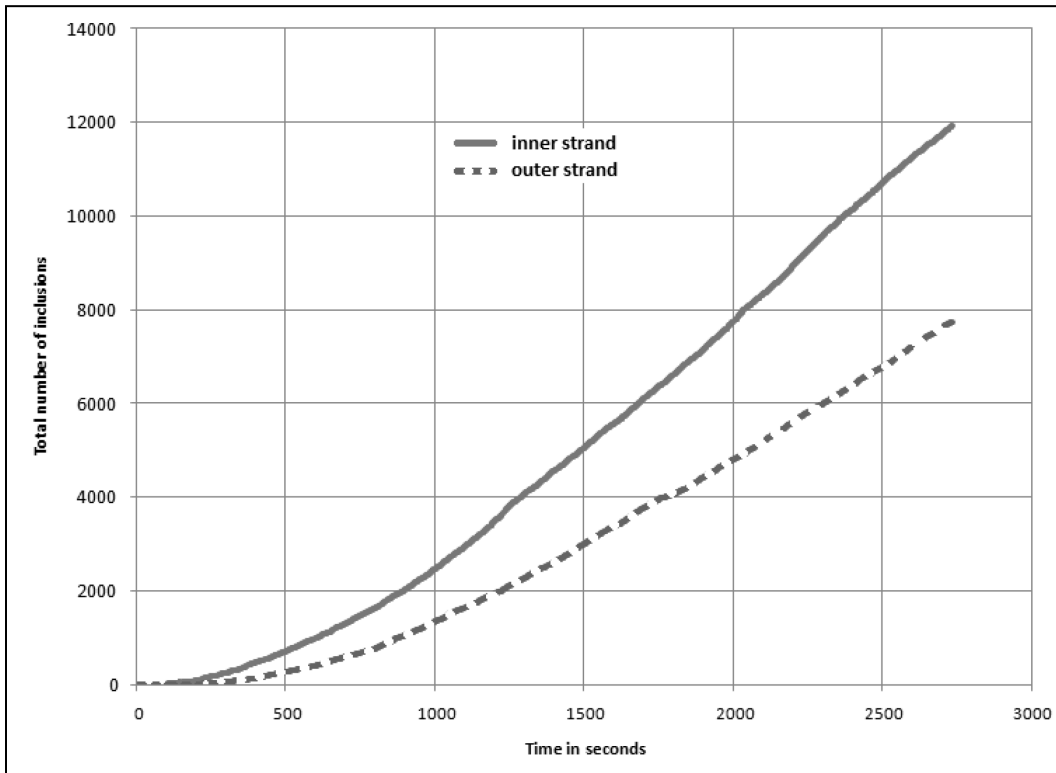


Figure 3.9 – Total particle count at exit strands in a bare tundish

With the new online APS system operational, it was decided to use the experimental setup to be used with a number of flow modifiers to judge their performance. Since the slope of the APS curve gave an indication of the inclusion count in each strand, it was defined as a measured quantity of interest associated to each strand under a particular tundish configuration. The quantity defined as

Steady-state Inclusion Entrainment Rate (SIER) = total number of inclusions of all sizes exiting a strand per second = slope of the linear region of the APS curve.

Needless to mention, a higher value of SIER would point to an inferior tundish configuration. The quantity can be thus used as a convenient performance characteristic for comparison of two different tundish configurations.

3.4.1 Experiments with different flow modifiers (Rio Tinto QIT, Fer. et Titan. 4 strand , delta shaped tundish)

Four different flow modifiers were installed inside the tundish, and tested for a performance comparison. Figure 3.10 shows the different flow modifiers that were tested.

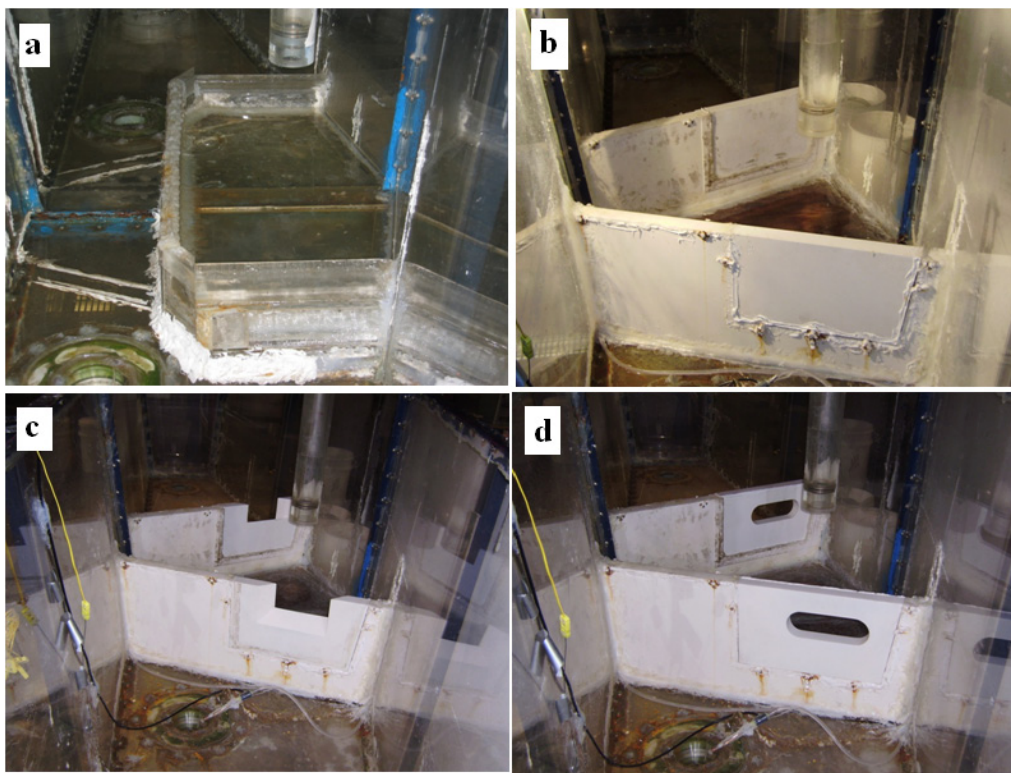


Figure 3.10 – Image showing the flow modifiers tested. a) standard QIT impact pad b) angled dam c) slotted dam and d) holed dam.

From Figure 3.11, it is interesting to note that an improvement in SIER for one of the strands, either inner or outer, does not necessarily translate to improved SIER values for the other strand. For example, comparing data between the impact pad and angled dam, there is an improvement in the inner strand while reduced performance for the outer strand. The new online APS system can thus be used as

a convenient research tool for testing and comparison of tundish performance under differing configurations.

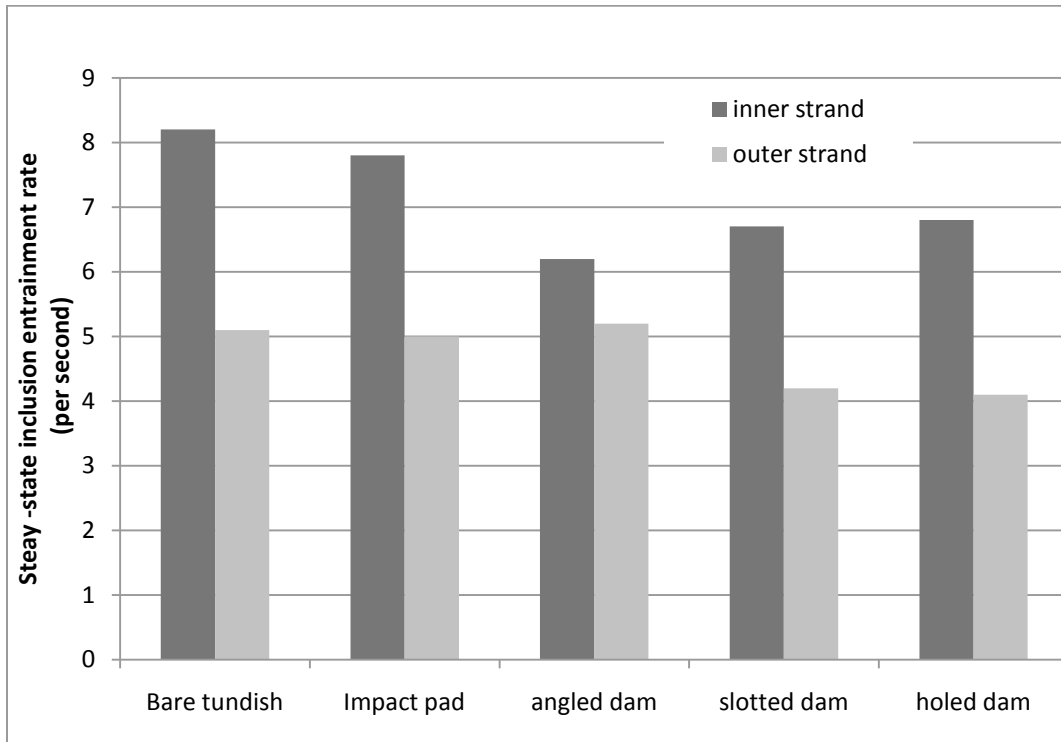


Figure 3.11 – Comparison of flow modifier performance using SIER

3.4.2 Calculation of RRI for the standard impact pad

The results of the calculation are shown in Figure 3.12 (ref 93). The higher Stokes value of the larger inclusions facilitates their easy float-out and very few of them are entrained into the strands. Meantime, the smaller particles rise more slowly and the residence time of the water in the tundish is inadequate for their removal. These two facts are well corroborated by the RRI curves. RRI values are very high at the smaller end of the particle size range, while it reduces to essentially zero at sizes above 120 microns.

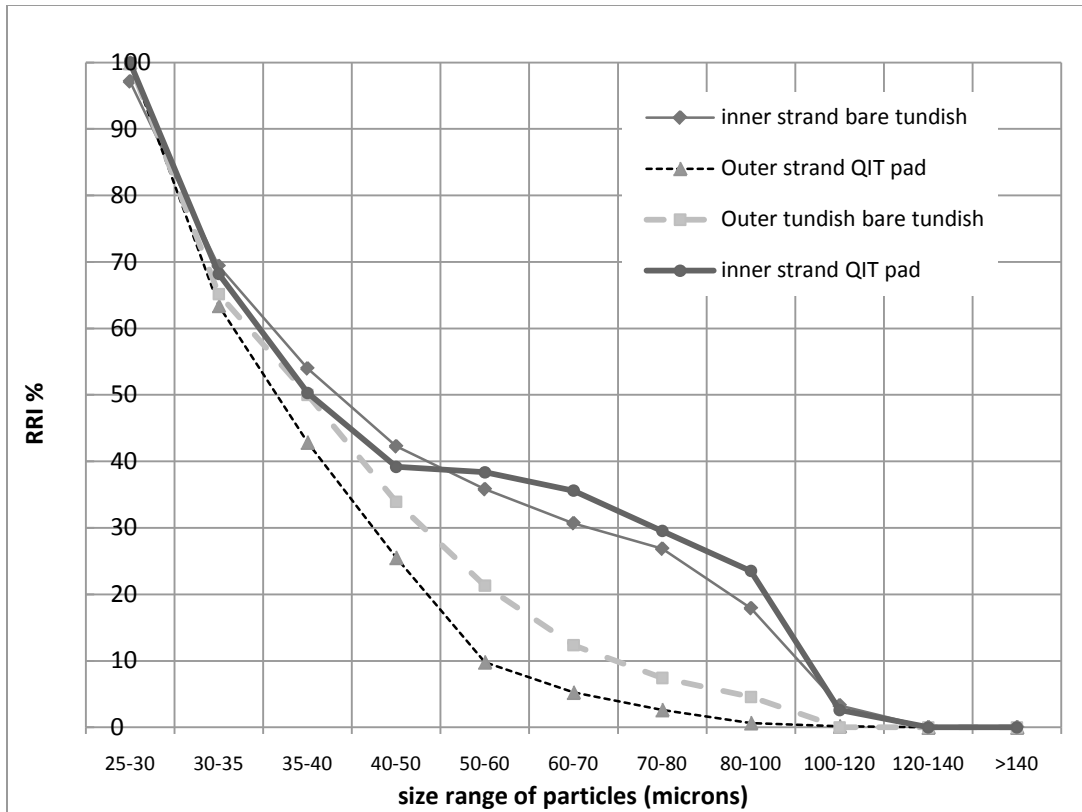


Figure 3.12 – Comparison of RRI values at differing size ranges between bare tundish and standard impact pad.

A careful study of the above graph reveals a minor improvement in inclusion removal with the standard impact pad, but almost no improvement for the inner strands. The above data was gathered as a part of an experiment requisitioned by Rio Tinto Quebec Iron and Titanium (QIT), since the use of this particular impact pad is the standard operational practice in their manufacturing unit. RRI calculations for the other flow modifiers were decided to be outside the scope of the present preliminary study because of their rare industrial use, and previous research pointing towards their very limited performance improvements.

Conclusions

- A new and improved Aqueous Particle Sensor (APS III) has been developed from first principles. It can outperform its commercial counterpart, both in terms of its accuracy, reliability and versatility
- The new system can be used as an invaluable research tool in carrying out inclusion behavior studies in a variety of physical modeling experiments involving liquid metal processing operations
- The setup designed gathers real-time inclusion count and inclusion size distribution, and is the only known research facility of its type. Analysis of the total inclusion count data plotted as a function of time can be used to obtain a new derived quantity, the Steady-state Inclusion Entrainment Rate (number of inclusions detected per second). This can be used as an indicator for comparing inclusion float-out potential of a particular tundish configuration
- The data obtained from the results can also be used to obtain Residual Ratio of Inclusions (RRI) over the entire size range of inclusion measurement.
- Contrary to the marked improvement in tundish performance obtained by using flow modifiers, as shown by slag entrainment tests and flow field visualization techniques, this RRI study of a few such industrially used fittings, showed only a marginal improvement, and that too, only at selected strand positions. At times, the use of flow modifiers even resulted in higher values of RRI, especially at the inner strand positions.

Future work

- In the preliminary experiments carried out, symmetry conditions were assumed, where APS detectors were only installed on one side of the symmetry axis, assuming that corresponding positions on the other side of the axis would show similar inclusion distributions. However, in the industry, symmetry conditions may not always hold good as the shroud positioning may not be exactly neutral with respect to the tundish. Research suggests a marked asymmetry in steel quality obtained from the strands as a result. A 4 channel version of APS III is being installed at MMPC laboratories to study the effects of biased shroud positioning on RRI.
- The sensing probes developed were of appreciable size, about 13 cm long and 1.2 cm in diameter. Concerns could be raised that the presence of these elements within the flow fields may modify it to some extent. Currently, a miniaturized version of the detector element is being designed which will have a much lower effect on the local flow fields within the liquid.
- The algorithm being implemented in the setup only measures the height of each peak, and no other aspects of its shape. Previous research suggests that the exact skewness and kurtosis of each signal peak can provide added information about the particle apart from its equivalent cross sectional area, like density, bulk modulus etc.
- Modern commercial LiMCA devices are currently being marketed both for the Aluminum and Steel industry. Though the exact algorithm and particle discrimination techniques may be proprietary materials to its manufacturers, a preliminary study may be made to implement the APS III particle discrimination algorithm to LiMCA equipment for application in the metallurgical industry.

References

- 1) Y. Sahai and T. Emi: “Tundish Technology for Clean Steel Production”, ISBN-13 978-981-270-621-8, pp 17
- 2) G.E. Dieter: Mechanical Metallurgy, ISBN 0-07-084187-X, pp 212
- 3) Copper & Copper Alloys: ASTM Designation B577-87 02.01 Philadelphia PA, 1987
- 4) L. Riopelle: J. Met., 1996 vol. 48(10), pp 44-46
- 5) J.D. Hannawalt, C.E. Nelson and J.A. Peloubet: Trans AIME 1942 vol. 147 pp 173-99
- 6) Y. Lakhtin, N. Weinstein: Engineering Physical Metallurgy, ISBN: 0898750857
- 7) M.Li, C. Carozza and R.I.L. Guthrie: “Particle Discrimination in Water Based LIMCA (Liquid Metal Cleanliness Analyzer) System” Can Met Q, vol 39 No 3 pp 325-338, 2000
- 8) R. Conti and R.I.L. Guthrie: Pittsburg USA The Direct Measurement of Inclusions in Liquid Steel
- 9) R.I.L. Guthrie and M. Li: “In Situ Detection of Inclusions in Liquid Metals: Part I. Mathematical Modeling of the Behavior of Particles Traversing the Electric Sensing Zone” Met. & Mat. Trans., Vol. 32B, Dec 2001-1067
- 10) M. Li and R.I.L. Guthrie: “Numerical Studies of the Motion of Particles in Current-Carrying Liquid Metals Flowing in a Circular Pipe” Met. & Mat. Trans., Vol. 31B, Apr 2000-357
- 11) R.I.L. Guthrie and M. Li: “In Situ Detection of Inclusions in Liquid Metals: Part II. Metallurgical Applications of LIMCA Systems” Met. & Mat. Trans., Vol. 32B, Apr 2001-1081
- 12) J.C. Maxwell: A Treatise on Electricity and Magnetism, 3rd ed., Clarendon, Oxford, UK 1954 vol. 1 pp 429
- 13) H. Nakajima: “On the Detection and Behavior of Second Phase Particles in Steel Melts” PhD Thesis, McGill University, 1986 Montreal
- 14) S. Tanaka: “Modeling Inclusion Behavior and Slag Entrainment in Liquid Steel Processing Vessels” PhD thesis, McGill University, 1986 Montreal

- 15) T. Iida and R.I.L. Guthrie: "The Physical Properties of Liquid Metals" ISBN – 0-19-856331-0, pp - 232
- 16) T. Draganovici: "A User-Friendly Software Interface for the Liquid Metal Cleanliness Analyzer (LiMCA)" Master`s Thesis, 1994, Montreal
- 17) X. Shi: "Upgrading Liquid Metal Cleanliness Analyzer (LiMCA) with Digital Signal Processing (DSP) Technology" Master`s Thesis, McGill University, 1994 Montreal,
- 18) U.D. Larsen: "Particle Characterization Apparatus" US Patent, 6959618 B1
- 19) C. Carozza: "Montreal Water Modeling of Particle Discrimination Using LiMCA Technology" Master`s Thesis, McGill University, 1999
- 20) X. Wang: "In-Situ Detection of Inclusions in Liquid Steel" Comsol Conference, Boston 2008
- 21) R.W. Beblois and C.P. Bean: "Counting and Sizing of Submicron Particles by the Resistive Pulse Technique" Rev. Scientific Instrum., 1970, vol. 41 pp 909-15
- 22) W.R. Smythe: Phys. Fluids, 1961, vol 4 pp 756-59
- 23) X. Wang, R.I.L. Guthrie and M. Isac: Proceedings, Comsol Conf. Boston 2008
- 24) T.R. Auton, J.C.R. Hunt, and M. Prud`home: J. Fluid Mech., 1987, vol. 183, pp. 199-218
- 25) A.M. Fayon and J. Happel: AICHE J., 1960, vol. 6, pp. 55-58
- 26) R. Clift, J.R. Grace, and M.E. Weber: Bubbles Drops and Particles, Academic Press, Inc., New York, NY, 1978, pp. 112 and 225
- 27) M.D. Graham et al: "Potential-Sensing Method and Apparatus for Sensing and Characterizing Particles by the Coulter Principle" US Patent, 6175227 B1
- 28) M.Li and R.I.L. Guthrie: "On the Detection and Selective Separation of Inclusions in Liquid Metal Cleanliness Analyzer (LiMCA) Systems" Met. & mat. Trans., Vol. 31B, Aug 2000-767
- 29) W. H. Coulter: "Means for Counting Particles Suspended in a Fluid" US Patent, 2656508

- 30) W. H. Coulter: "Method of Making a Scanner Element for Particle Analyzers" US Patent, 3122431
- 31) M.I. Henderson: "Particle Studying Device Control Circuit" US Patent, 3271672
- 32) J.R. Coulter Jr.: "Flow-through Sample Apparatus for Use With Electrical Particle Study Device" US Patent, 3340470
- 33) W.R. Hogg: "Particle Analyzing Apparatus" US Patent, 3689833
- 34) W.H. Coulter and W.R. Hogg: "Electronic Particle Analyzing Apparatus with Improved Aperture Tube" US Patent, 3714565
- 35) W.H. Coulter and J.R. Coulter Jr.: "Electronic Particle Study Apparatus With Improved Aperture Tube" US Patent 3361965
- 36) W.R. Hogg: "Method for making Glass Aperture Tube and Product Produced Thereby" US Patent, 3539919
- 37) W.R. Hogg: "Apparatus for Preservation and Identification of Particles Analyzed by Flow-Through Apparatus" US Patent, 4009435
- 38) J.A. Pontigny: "Particle Counting Apparatus Including Isolated Manometer" US Patent, 3921006
- 39) R. Karuhn, R. Davis and M.J. Clinch: "Studies on the Coulter Counter Part I - Investigations into the Effect of Orifice Geometry and Flow Direction on the Measurement of Particle Volume." Powder Tech. 11(1975) 157-171
- 40) R. Davies, R. Karuhn and J. Graph: Powder Tech. 12(1975) 157
- 41) R. Davies, R. Karuhn, J. Graph and J. Stockham: "Studies on the Coulter Counter Part III - Applications of the IITRI Sensing System" Powder Tech. 13(1976) 193-201
- 42) W.H. Coulter: "Method and System for Cleaning an Aperture in a Particle Study Device" US Patent, 3963984
- 43) T.J. Gaudin: "Particle Analyzing System" US Patent, 3979669
- 44) M.R. Groves: "Particle Shape Determination" US Patent, 4298836
- 45) W.R. Hogg: "Tandem Sensing Zones for Improved Signal-to-Noise Ratio in Particle Analyzer" US Patent, 4438390

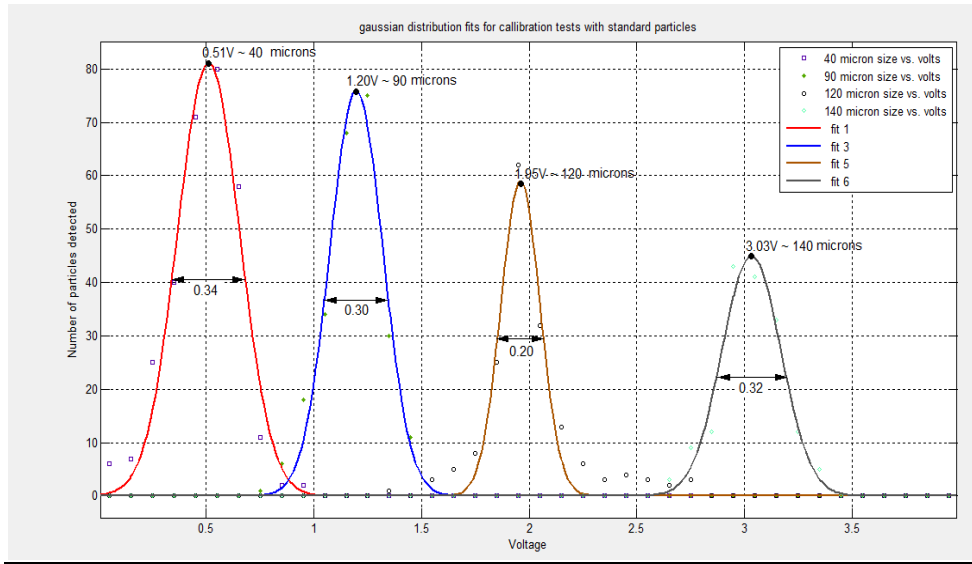
- 46) W.H. Coulter and W.R. Hogg: "Method and Apparatus for Studying Particles Having Widely Different Sizes" US Patent, 3882385
- 47) R.O. Simpson et al: "Aperture Module for use in Particle Testing Apparatus" US Patent, 4090128
- 48) T.J. Gaudin: "Transducers for Measuring Particles Suspended in a Fluid" US Patent, 4491786
- 49) W.H. Coulter: "Particle Analyzing Device" US Patent, 3271671
- 50) W.H. Coulter: "Particle Analyzing Device" US Patent, 3259842
- 51) W.A. Claps: "Noise Discrimination Circuitry and Method for Electronic Particle Study Apparatus" US Patent, 3781674
- 52) R.I. Klein and W.R. Hogg: "Particle Analyzing System for Coulter Particle Device and Method" US Patent, 3783247
- 53) W.H. Coulter and W.R. Hogg: "Particle Analyzing Apparatus and Method Utilizing Multiple Apertures" US Patent, 3444463
- 54) W.H. Coulter et al: "Method and Apparatus for Providing Primary Coincidence Correction During Particle Analysis Utilizing Time Generation Techniques" US Patent, 3936741
- 55) W.H. Coulter and W.R. Hogg: "Particle Analyzer of the Coulter Counter Type Including Coincidence Error Correction Circuitry" US Patent, 3968429
- 56) W.H. Coulter and W.R. Hogg: "Method and Apparatus for Determining the Correct Percentiles of the Size Distribution of a Particulate System" US Patent, 3944797
- 57) W.R. Hogg and W.H. Coulter: "Method and Apparatus for Automatically Sampling Pulses a Predetermined Average Number of Times for Storage and Subsequent Reproduction" US Patent, 3936740
- 58) W.R. Hogg: "Method and Apparatus for Correcting Total Particle Volume Error Due to Particle Coincidence" US Patent, 3987391
- 59) S.K. Campbell: "Method and Apparatus for Providing Primary Coincidence Correction During Particle Analysis" US Patent, 3938038
- 60) W.H. Coulter and W.R. Hogg: "Method and Apparatus for Particle Length Measurement" US Patent, 3890568

- 61) D.A. Doutre: "The Development and Application of a rapid Method of Evaluating Molten Metal Cleanliness" PhD Thesis, McGill University 1986, Montreal
- 62) M. Li and R.I.L. Guthrie: "Liquid Metal Cleanliness Analyzer (LiMCA) in Molten Aluminum" *ISIJ Int.*, Vol 41 (2001), No. 2, pp. 101-110
- 63) R.I.L. Guthrie: "Molten Metal Inclusion Sensor" US Patent, 5789910
- 64) D.A. Doutre and R.I.L. Guthrie: "Apparatus for the Detection and Measurement of Particulates in Molten Metal" US patent, 4600880
- 65) D.A. Doutre and R.I.L. Guthrie: "Method and Apparatus for the detection and Measurement of Particulates in Molten Metal" US patent, 4555662
- 66) D.A. Doutre: "Method and Apparatus for the Detection and Measurement of Solid particles in Molten Metal" US Patent, 5834928
- 67) R. Hachey: "Apparatus for Particle Determination in Liquid Metals" US Patent, 5130639
- 68) R.I.L. Guthrie and H. Nakajima: "Single-Use Disposable Molten Metal Inclusion Sensor" US Patent, 5198749
- 69) R.I.L. Guthrie and H. Nakajima: "Continuous-Use Molten Metal Inclusion Sensor" US Patent, 5241262
- 70) J. Wannasin, D. Schwam and J.F. Wallace: "Evaluation of Methods for Metal Cleanliness Assessment in Die Casting" *JMPT*, 19 (2007) 242-246
- 71) S. Kuyucak: "Montreal Direct Detection of Non Metallic Inclusions in Molten Iron" Master's Thesis, McGill University 1985,
- 72) S. Kuyucak: "On the Direct Measurement of Inclusions in Molten Metals" PhD Thesis, McGill University 1989, Montreal
- 73) J.W. Fergus: "Sensors in Monitoring the Quality of Molten Aluminum During Casting" *ASM International, JMEPEG* (2005) 14:267-275
- 74) X. Cao: "A New Indirect Method of Measuring the Contents of Solid Inclusions in Liquid Aluminum" *J. Mater. Sci.*, 41 (2006) 4285-4292
- 75) T.L. Mansfield: *Proceedings of the 3rd Int. Aluminum Extrusion Tech. Seminar*, pp-273-278, The Aluminum Assoc., Atlanta 1984

- 76) N.D.G. Mountford and A. McLean: Steel Industry / Researcher, Sensor Research Workshop, 1984, pp 97-98
- 77) N.D.G. Mountford et al: Steelmaking Proceedings, ISS, 5th Int. Iron and Steel Cong., pp 699-704, Washington DC, 6-9 April 1986
- 78) Y Ono et al: “An On-Line Ultrasonic Cleanliness Analyzer for Molten Metals” Light Metals JOM 4004 Feb,
- 79) LiMCA Literature published by ABB®, “Liquid metal cleanliness analyzer for continuous monitoring”
- 80) R. I. L. Guthrie : Engineering in Process Metallurgy ISBN13: 9780198563679, ISBN10: 0198563671
- 81) S.K. Ray: “Studies to predict steel quality to predict steel quality in a 4 strand delta shaped tundish” Master’s Thesis, McGill University, 2006, Montreal.
- 82) www.analog.com, Analog Devices, Inc., 1999, Norwood, USA: Precision Instrumentation Amplifier, AD 624
- 83) S. Hajj, Recommendations and Suggestions for the “Water LiMCA” sensor project, Report, 2009, Aug 12
- 84) DASYTEC ® Daten System Technik GmbH, Germany: DASYLab Book 2:Module Reference Guide
- 85) <http://www.mathworks.com/access/helpdesk/help/toolbox/curvefit/cftool.html> :Documentation →Curve Fitting Tool Box, The MathWorks ®
- 86) NIST Traceable certificate (Certification 5524), Duke Standards TM, Fermont CA, USA: Material Data Sheet, Dry Borosilicate Glass Microspheres
- 87) H. Kim: “Modeling of Transport Phenomenon in a Delta-shaped 4 strand Tundish” PhD Thesis, McGill University, 2009, Montreal
- 88) S.K. Ray: “On the application of physical and mathematical modeling to predict tundish performance” PhD thesis, McGill University, 2009, Montreal
- 89) R.M. Daelen, German Patent No. 51217, July 1889
- 90) S. Junghans, U.S. Patent No. 2135, November 1938

- 91) R.I.L. Guthrie and J.J. Jonas: Volume 1, 10th Edition: Properties and Selection, ASM International, Metals Handbook
- 92) <http://www.metsoc.org/VirtualTour/processes/images/Continuous+Caster+Schematic.jpg> :Met Soc, Continuous casting
- 93) A.Chakraborty, M.Isac and R.I.L. Guthrie “Results of RRI tests on standard QIT impact pad with 2 inch using the new McGill online aqueous particle detection system”, Technical report for QIT, Jan 27, 2009

Appendix 1, Gaussian curve fits using CFTOOL in MATLAB ®



FIT 1

General model Gauss1:

$$f(x) = a1 * \exp(-((x-b1)/c1)^2)$$

Coefficients (with 95% confidence bounds):

a1 = 81.17 (76.73, 85.61)
 b1 = 0.5107 (0.5015, 0.5198)
 c1 = 0.2052 (0.1922, 0.2181)

Goodness of fit:

SSE: 304.2
 R-square: 0.9797
 Adjusted R-square: 0.9786
 RMSE: 2.867

Nominal particle size= 40.6 microns
 Error = +/- 2.8 microns

FIT 2

General model Gauss1:

$$f(x) = a1 * \exp(-((x-b1)/c1)^2)$$

Coefficients (with 95% confidence bounds):

a1 = 75.9 (72.37, 79.44)
 b1 = 1.197 (1.191, 1.204)
 c1 = 0.1748 (0.1654, 0.1842)

Goodness of fit:

SSE: 164.5
 R-square: 0.9855
 Adjusted R-square: 0.9847
 RMSE: 2.108

Nominal particle size= 90 microns
 Error = +/- 4.5 microns

FIT 3

General model Gauss1:

$$f(x) = a1 * \exp(-((x-b1)/c1)^2)$$

Coefficients (with 95% confidence bounds):

a1 = 58.96 (54.39, 63.53)
 b1 = 1.96 (1.952, 1.968)
 c1 = 0.1293 (0.1179, 0.1408)

Goodness of fit:

SSE: 207.4
 R-square: 0.9595
 Adjusted R-square: 0.9573
 RMSE: 2.367

Nominal particle size= 120 microns
 Error = +/- 3 microns

FIT 4

General model Gauss1:

$$f(x) = a1 * \exp(-((x-b1)/c1)^2)$$

Coefficients (with 95% confidence bounds):

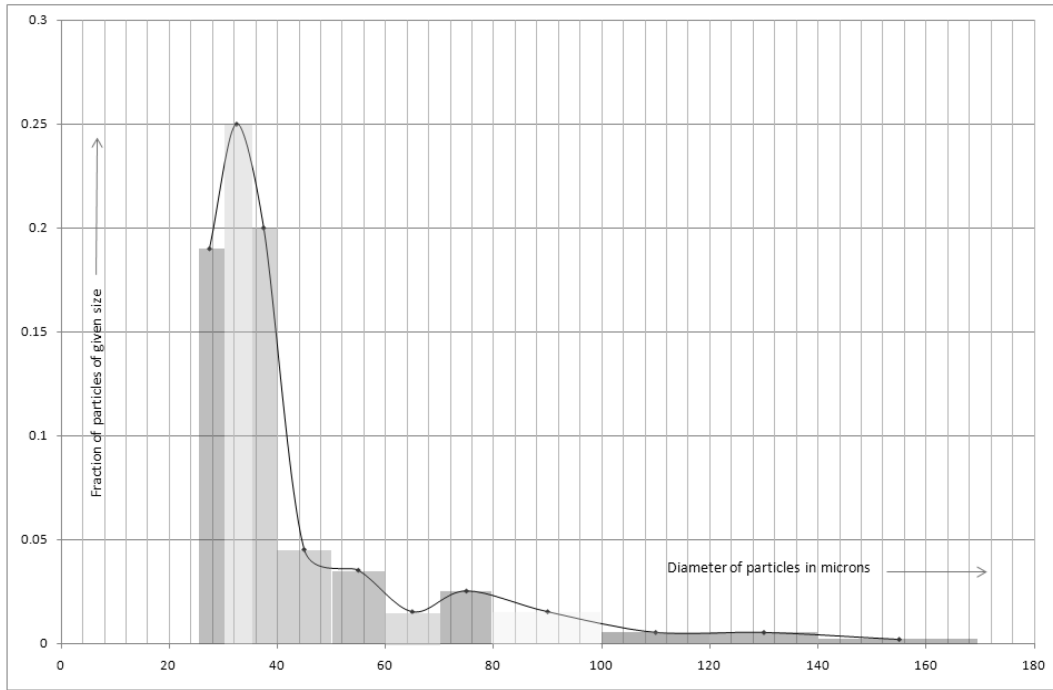
a1 = 44.93 (42.17, 47.68)
 b1 = 3.034 (3.024, 3.043)
 c1 = 0.1941 (0.1804, 0.2079)

Goodness of fit:

SSE: 111
 R-square: 0.9748
 Adjusted R-square: 0.9734
 RMSE: 1.732

Nominal particle size= 139 microns
 Error = +/- 7 microns

Appendix 2 – Results showing size distribution and properties of borosilicate microspheres



Particle size distribution density

Sl. No.	voltage range	Particle size range (microns)	Mean size	fraction of particles of size	Class range	Height of histogram
1	0.15 to 0.20	25 to 30	27.5	0.18	1	0.19
2	0.20 to 0.30	30 to 35	32.5	0.24	1	0.25
3	0.30. to 0.40	35 to 40	37.5	0.19	1	0.2
4	0.40. to 0.50	40 to 50	45	0.12	2	0.045
5	0.50 to 0.60	50 to 60	55	0.06	2	0.035
6	0.60 to 0.80	60 to 70	65	0.07	2	0.015
7	0.80. to 1.00	70 to 80	75	0.04	2	0.025
8	1.00 to 1.50	80 to 100	90	0.06	4	0.015
9	1.50 to 2.00	100 to 120	110	0.02	4	0.005
10	2.00 to 3.00	120 to 140	130	0.01	4	0.005
11	3.00 to 5.00	140 to 170	155	0.01	6	0.001666667



Density of borosilicate glass, $\rho=2.01\text{ g/cc}$
 Let a =outer diameter of the glass microsphere in cm
 b =inner diameter of the microsphere in cm

$$\text{therefore total mass of particle} = \left[\frac{4}{3} \pi \left(\frac{a}{2} \right)^3 - \frac{4}{3} \pi \left(\frac{b}{2} \right)^3 \right] \rho = \frac{\pi \rho}{6} (a^3 - b^3)$$

$$\text{Volume of the particle} = \frac{4}{3} \pi \left(\frac{a}{2} \right)^3$$

$$\text{Therefore } \rho_{\text{effective}} = \rho \left(1 - \frac{b^3}{a^3} \right) \text{ gm/cc}$$

Particle ID		microns	cm	density (gm/cc)
1	a (outer dia)	46	4.60E-05	0.69
	b (inner dia)	40	4.00E-05	
2	a (outer dia)	28	2.80E-05	0.66
	b (inner dia)	24.5	2.45E-05	
3	a (outer dia)	18	1.80E-05	0.70
	b (inner dia)	15.6	1.56E-05	
4	a (outer dia)	10	1.00E-05	0.69
	b (inner dia)	8.7	8.70E-06	

Appendix 3 – Calculation of RRI

	>140	120-140	100-120	80-100	70-80	60-70	50-60	40-50	35-40	30-35	25-30	inner strand bare tundish
t=1800 secs	0	0	0	140.82	140.82	281.64	281.64	492.87	1056.15	2182.71	2464.35	
t=2733 secs	0	0	6	238.56	238.56	477.12	477.12	954.24	1989.2	3697.68	4055.52	
rate per sec (sampled)	0	0	0.006431	0.104759	0.104759	0.209518	0.209518	0.494502	1.000054	1.623762	1.705434	
rate per sec (bulk)	0	0	19.78135	322.2382	322.2382	644.4764	644.4764	1521.087	3076.165	4994.692	5245.915	
particle assay (f)	0.01	0.01	0.02	0.06	0.04	0.07	0.06	0.12	0.19	0.24	0.18	
inlet rate (bulk)	300	300	600	1800	1200	2100	1800	3600	5700	7200	5400	
RRI	0	0	3.296892	17.90212	26.85318	30.68935	35.80424	42.25242	53.9678	69.37072	97.14658	
	>140	120-140	100-120	80-100	70-80	60-70	50-60	40-50	35-40	30-35	25-30	outer strand bare tundish
t=1800 secs	0	0	0	58	72.3	145.23	190.78	249.89	536	842.82	1325.19	
t=2733 secs	0	0	0	83	99.32	223.9	307.12	620.23	1400.54	2265.92	2959.68	
rate per sec (sampled)	0	0	0	0.026795	0.02896	0.084319	0.124695	0.396935	0.926624	1.525295	1.751865	
rate per sec (bulk)	0	0	0	82.42229	89.08202	259.3665	383.5604	1220.971	2850.295	4691.807	5388.737	
particle assay (f)	0.01	0.01	0.02	0.06	0.04	0.07	0.06	0.12	0.19	0.24	0.18	
inlet rate (bulk)	300	300	600	1800	1200	2100	1800	3600	5700	7200	5400	
RRI	0	0	0	4.579016	7.423501	12.35078	21.30891	33.91586	50.00517	65.16398	99.79142	
	>140	120-140	100-120	80-100	70-80	60-70	50-60	40-50	35-40	30-35	25-30	outer strand QIT pad
t=1800 secs	0	0	2	35	53.73	98.56	110.49	180.32	410.22	842.82	1219.85	
t=2733 secs	0	0	2.3	38.36	62.67	129.75	160.46	440.47	1101.99	2135.92	3869.65	
rate per sec (sampled)	0	0	0.000322	0.003601	0.009582	0.03343	0.053558	0.278832	0.741447	1.385959	2.8403	
rate per sec (bulk)	0	0	0.989068	11.07756	29.47421	102.8301	164.7457	857.6864	2280.691	4263.211	8736.763	
particle assay (f)	0.01	0.01	0.02	0.06	0.04	0.07	0.06	0.12	0.19	0.24	0.18	
inlet rate (bulk)	280	280	560	1680	1120	1960	1680	3360	5320	6720	5040	
RRI	0	0	0.176619	0.659378	2.631626	5.246431	9.806291	25.52638	42.87013	63.44064	100	
	>140	120-140	100-120	80-100	70-80	60-70	50-60	40-50	35-40	30-35	25-30	inner strand QIT pad
t=1800 secs	0	0	3.6	168.73	162.59	325.64	281.64	482.59	937.65	2099.58	2560.5	
t=2733 secs	0	0	8	288.56	262.9	537.25	477.12	881.77	1809.11	3490.1	4100.5	
rate per sec (sampled)	0	0	0.004716	0.128435	0.107513	0.226806	0.209518	0.427846	0.869732	1.490375	1.650589	
rate per sec (bulk)	0	0	14.50632	395.0665	330.7112	697.6553	644.4764	1316.053	2675.296	4584.394	5077.213	
particle assay (f)	0.01	0.01	0.02	0.06	0.04	0.07	0.06	0.12	0.19	0.24	0.18	
inlet rate (bulk)	280	280	560	1680	1120	1960	1680	3360	5320	6720	5040	
RRI	0	0	2.590415	23.51587	29.52779	35.59466	38.36169	39.16825	50.28751	68.22015	100	